2009

Fracture toughness, crack-growth-rate and creep studies of alloy 276

Joydepp Pal
University of Nevada Las Vegas

FRACTURE TOUGHNESS, CRACK-GROWTH-RATE AND CREEP STUDIES OF ALLOY 276

by

Joydeep Pal

Bachelor of Science in Engineering
Jadavpur University, Kolkata, India
July 2000

Master of Science in Mechanical Engineering
University of Nevada, Las Vegas
December 2006

A dissertation submitted in partial fulfillment
of the requirements for the

Doctor of Philosophy Degree in Mechanical Engineering
Department of Mechanical Engineering
Howard R. Hughes College of Engineering

Graduate College
University of Nevada, Las Vegas
December 2009

UNLV
UNIVERSITY OF NEVADA LAS VEGAS

THE GRADUATE COLLEGE

We recommend that the dissertation prepared under our supervision by

Joydeep Pal

entitled

Fracture Toughness, Crack-growth-rate and Creep Studies of Alloy 276

be accepted in partial fulfillment of the requirements for the degree of

Doctor of Philosophy
Mechanical Engineering

Brendan O'Toole, Committee Chair

Ajit K. Roy, Committee Co-Chair

Woosoon Yim, Committee Member

Anthony E. Hechanova, Committee Member

Daniel Cook, Committee Member

Edward S. Neumann, Graduate Faculty Representative

Ronald Smith, Ph. D., Vice President for Research and Graduate Studies
and Dean of the Graduate College

December 2009

ABSTRACT

Fracture Toughness, Crack-growth-rate and Creep Studies of Alloy 276

by

Joydeep Pal

Dr. Brendan O'Toole, Examination Committee Chair
Associate Professor of Mechanical Engineering
University of Nevada, Las Vegas

Dr. Ajit K. Roy, Examination Committee Co-Chair
Professor of Mechanical Engineering
University of Nevada, Las Vegas

Austenitic nickel-base Alloy 276 had been proposed to be a candidate structural material within the purview of the nuclear hydrogen initiative program. A mechanistic understanding of high temperature tensile deformation of this alloy has already been presented in an earlier investigation. The current investigation has been focused on the evaluation of crack-growth behavior, fracture toughness, stress-corrosion-cracking and creep deformation of this alloy as functions of different metallurgical and mechanical variables. The results of crack-growth study under cyclic loading indicate that this alloy exhibited greater cracking tendency with increasing temperature at a constant load ratio (R). However, the effect of temperature on crack-growth-rate was more pronounced within a temperature range of 100-150 °C when the R value was kept at 0.1. The fracture toughness of this alloy in terms of J_{IC} was significantly reduced at 100 °C compared to those at higher temperatures. As to the cracking susceptibility of this alloy in an acidic solution, the average crack-growth-rate was gradually reduced with increasing exposure time probably reaching a near threshold value following eight months of testing. Limited data on creep testing suggest that Alloy 276 may be capable of withstanding time-

dependent deformation at 750, 850 and 950 °C under sustained loading equivalent to its 10 percent yield strength values at these temperatures. Finally, the extent of deformation under different modes of loading was analyzed by numerous state of the art characterization tools.

TABLE OF CONTENTS

LIST OF TABLES

LIST OF FIGURES

ACKNOWLEDGMENTS

I am extremely happy to take this opportunity to acknowledge my debts of gratitude to them who are associated in the preparation of this dissertation.

Words fail to express my profound regards from the inmost recess of my heart to my advisors Dr. Ajit K. Roy and Dr. Brendan O'Toole for their invaluable help, constant guidance and wide counseling extended by them toward successful completion of my research work.

I would like to thank my committee members, Dr. Anthony Hechanova, Dr. Woosoon Yim, Dr. Daniel Cook and Dr. Edward Neumann, for their direct and indirect contribution throughout this investigation. Special thanks should be given to Dr. Longzhou Ma for his expert guidance and my project mates Hasan and Sudin, who helped me in many ways.

Keeping separate space in my heart, I would like to thank my wife, **Ratnabali** for her great support and encouragement throughout my research. I would also like to thank our baby daughter **Rajeeka**, who has been a tremendous source of inspiration.

The zeal and enthusiasm provided by my parents Mr. D.C. Pal and Mrs. S. Pal are thankfully acknowledged. I would also like to thank my brother Sudip for his support.

Finally I would like to acknowledge the financial support of the United States Department of Energy (USDOE), grant number DE-FC07-04ID14566.

CHAPTER 1

INTRODUCTION

The continued increase in the cost of fossil fuels has provided an impetus to develop alternate forms of energy, such as hydrogen (H_2). However, the cost of hydrogen generation using a conventional electrolysis technique is generally high. Therefore, the United States Department of Energy (USDOE) has been considering the development of hydrogen using nuclear heat within the purview of the Nuclear Hydrogen Initiative (NHI) program using a thermochemical process, known as the sulfur-iodine (S-I) cycle. The energy required for the chemical reactions to occur in the S-I process is proposed to be provided by the heat generated from the nation's nuclear power plants. The concept of hydrogen generation using the S-I cycle is described below.

1.1 S-I Cycle

The S-I process consists of three chemical reactions to form and decompose sulfuric acid (H_2SO_4) and hydrogen iodide (HI), respectively at different temperatures, as illustrated in Figure 1-1. The formation of H_2SO_4 and HI will be achieved by activating chemical reactions among sulfur dioxide (SO_2), iodine (I_2) and water at 120 °C. H_2SO_4 and HI will subsequently be separated and transferred to two different reaction chambers. The decomposition of H_2SO_4 has previously been recommended to occur at a temperature of 950 °C for enhanced efficiency in H_2 generation, leading to the formation of oxygen (O_2), SO_2 and water (H_2O). Simultaneously, HI will be allowed to undergo decomposition at a temperature of 400 °C, producing H_2 and I_2. The generated O_2 and H_2 will then be transferred to two separate containers. Both SO_2 and I_2 will be recycled to

react with water producing H_2SO_4 and HI, as shown in Figure 1-1. Thus, SO_2 and I_2 can act as catalysts to generate H_2SO_4 and HI, and the overall process will be repeated.

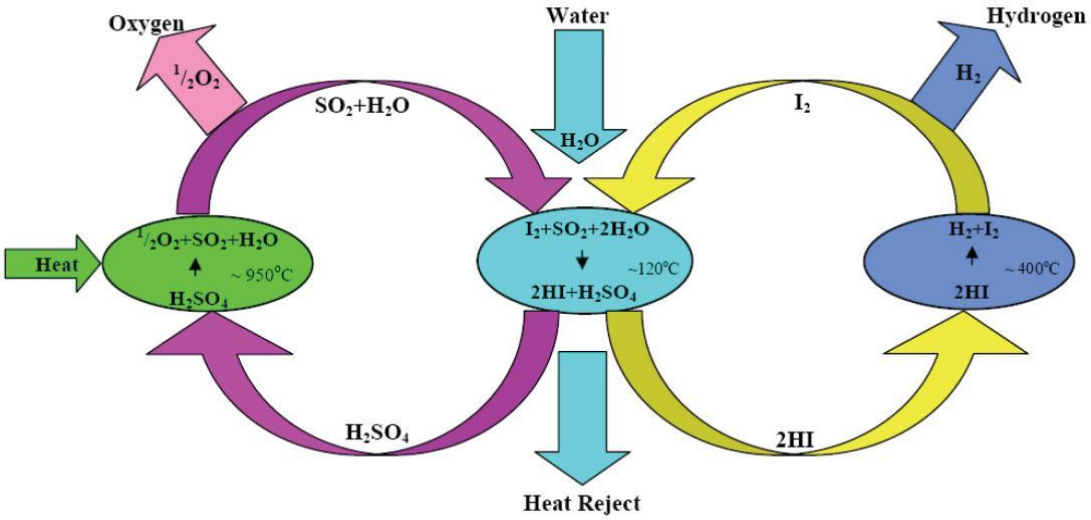

Figure 1-1 S-I Water Splitting Cycle for Hydrogen Generation

The overall chemical reactions associated with the S-I process are given by reactions 1-1, 1-2, and 1-3. As indicated earlier, the formation of HI and H_2SO_4 takes place at a much lower temperature compared to those of the HI and H_2SO_4 decomposition reactions. The application of an unusually high temperature (950 °C) for H_2SO_4 decomposition was thought to have achieved an enhanced efficiency in hydrogen generation through utilization of this thermochemical process. However, more recently, a maximum operating temperature of 800 °C has been recommended [1] in view of the severity in operating conditions associated with such an elevated temperature that may be impractical from a realistic point of view.

$$I_2 + SO_2 + 2H_2O \rightarrow 2HI + H_2SO_4 \text{ (Temperature ~ 120 °C)} \qquad \text{Reaction 1-1}$$

$H_2SO_4 \rightarrow H_2O + SO_2 + ½ O_2$ (Temperature ~ 950 °C) Reaction 1-2

$2HI \rightarrow H_2 + I_2$ (Temperature ~ 400 °C) Reaction 1-3

1.2 Research Objective

The generation of H_2 from thermochemical reactions at different temperatures is a major challenge to scientists and engineers. This challenge stems from the identification and selection of suitable structural materials possessing the desired metallurgical properties and corrosion resistance under conditions relevant to the proposed S-I process. A major requirement for the structural materials is their adequate mechanical strength at temperatures up to 1000 °C. Simultaneously, these materials have to withstand many hostile chemical environments during the formation and decomposition of H_2SO_4 and HI at different temperatures. Thus, the structural materials to be used in nuclear hydrogen generation must possess superior tensile properties including strength and ductility at elevated temperatures, and exhibit excellent corrosion resistance in acidic environments of very low pH values.

The structural materials used in many industrial applications can undergo mechanical degradations under different types of loading. These degradations include tensile, creep, and fatigue deformation at elevated temperatures. Plastic instability of these materials under tensile loading can lead to reduced tensile strength and ductility. Similarly, time-dependent plastic deformation under sustained loading (creep), and deformation under cyclic loading (fatigue) may also be experienced by these engineering materials. Thus, the identification of suitable materials with superior tensile properties, and optimum resistance to creep and fatigue failures will play a major role in nuclear hydrogen generation using the S-I process. Further, they should possess adequate fracture

toughness. These materials could also suffer from environment-induced degradations such as stress-corrosion-cracking (SCC) while exposed to hostile aqueous environments containing H_2SO_4 and HI. Therefore, the identification of suitable structural materials to circumvent the detrimental effects of elevated temperatures and aggressive chemical species is the first step to develop a strategic plan to generate hydrogen using the S-I process. In view of this judgment, a nickel-base austenitic superalloy, namely Alloy 276 has been identified to be a suitable candidate structural material for heat-exchanger applications during the H_2SO_4 decomposition process. Alloy 276 has superior overall properties as noted by its manufacturer [2], and results obtained from preliminary tests conducted by the UNLV Materials Performance laboratory (MPL) group. This investigation has been focused on the evaluation of this alloy for such application.

Alloy 276 was originally developed by the Haynes International Inc. for prospective use in modern day industrial applications due to its exceptional capability to withstand severe operating conditions including hostile corrosive environments, elevated temperatures, high stresses of different types, and a combination of all these environmental and mechanical variables [2-5]. Alloy 276 (UNS N10276) is a nickel-chromium-molybdenum (Ni-Cr-Mo) superalloy possessing high strength, ductility, and corrosion resistance in many hostile environments. This alloy has a continuous matrix of face centered cubic (FCC) Ni-base solid solution of Cr, Mo, iron (Fe), cobalt (Co) and tungsten (W). Alloy 276 is routinely used in flue gas desulfurization systems because of its excellent resistance to degradation in the presence of sulfur compounds. This alloy is also extensively used in chemical processing, pollution control, pulp and paper production, industrial and municipal waste treatment, and the recovery of sour natural

gas. Its applications in air pollution control include stack liners, ducts, dampers, scrubbers, stack-gas re-heaters, fans and fan housings. This alloy has also been used in components for chemical processing, such as heat-exchangers, reaction vessels, evaporators and transfer piping [2-5].

Alloy 276 is known to exhibit enhanced resistance to corrosion in seawater, especially under a crevice condition. The presence of high Mo content in this alloy can provide an enhanced resistance to localized corrosion such as pitting. Further, the presence of low carbon content in this alloy can minimize or prevent carbide precipitation during welding, providing excellent resistance to intergranular attack in the heat-affected zone of many welded joints and structures [2-5].

A mechanistic understanding on tensile deformation of Alloy 276 at temperatures ranging from ambient to 1000 °C had been presented in an earlier investigation performed by Pal [6, 7]. The structural integrity of engineering components is known to be influenced by the presence of surface irregularities such as cracks and flaws in metals and alloys. The engineering materials may also be subjected to different types of loading due to a fluctuation in the operating temperatures as expected in the proposed S-I process for nuclear hydrogen generation. Therefore, efforts have been made in this investigation to evaluate the crack-propagation-rate (CGR) of Alloy 276 under cyclic loading at ambient and elevated temperatures using fracture-mechanics-based testing specimens. The fracture toughness of this alloy has also been evaluated at ambient and elevated temperatures using elastic-plastic-fracture-mechanics (EPFM) principle [8, 9]. As to the corrosion behavior of Alloy 276, its susceptibility to stress-corrosion-cracking (SCC) has

been evaluated by using wedge-loaded and precracked fracture mechanics-based specimens as a function of exposure time in an acidic solution.

Further, a limited study on creep deformation of Alloy 276 has been performed at three elevated temperatures for 1000 hours. The creep study was conducted to develop a deformation mechanism of this alloy under a sustained loading condition at different temperatures relevant to the S-I process. Finally, the extent and morphology of failure of the tested specimens were determined by using scanning electron microcopy (SEM). It is anticipated that the overall data presented in this dissertation will provide a realistic assessment on the performance capability of Alloy 276 for prospective application as a heat exchanger material as functions of different metallurgical, mechanical, and environmental variables.

1.3 Test Matrix

Since the maximum operating temperature was stipulated by the USDOE NHI program to be 950 °C, it was considered essential to evaluate the tensile properties of the proposed candidate heat exchanger material, Alloy 276 at temperatures approaching 1000 °C. An increment in temperature by 50 °C from the maximum recommended temperature of 950 °C was considered to satisfy the convention prescribed by the ASME pressure vessel code. Simultaneously, a consideration was also made to apply very high temperatures to evaluate the crack growth behavior (da/dN), fracture toughness (J_{IC}) and creep deformation of Alloy 276. However, at the time of the evaluation of da/dN and J_{IC}, the Instron testing equipment could not be utilized using the furnace due to its malfunctioning. Therefore, both da/dN and J_{IC} studies were performed only up to temperatures of 300 and 500 °C, respectively (the point before equipment malfunction).

Further, even though the autoclave was thought to be used up to a maximum temperature of 600 °C, stress-corrosion-cracking (SCC) testing using DCB specimens could not be accommodated beyond 100 °C due to unexpected leakage. In view of all these rationales, the following test matrix (Table 1-1) was pursued. It is to be noted that the results of tensile testing ranging from ambient to 1000 °C were included in an earlier M.S. Thesis [6].

Table 1-1 Test Matrix for Alloy 276

Type of Testing	Temperature (°C)	Test Conditions
Tensile	Ambient – 1000 (100 °C increments)	Nitrogen; Strain rate = 5×10^{-4} sec^{-1}
Crack-growth-rate	Ambient, 150, 300, 500, 750, 850 and 950*	Air, Frequency =1 Hz; Load ratios = 0.1, 0.2 and 0.3
Fracture Toughness	Ambient, 100, 200, 500, 750, 850 and 950†	Air; Single specimen technique
Creep	750, 850 and 950	Air; Initial stresses = 0.10 and 0.25YS
Stress-corrosion-cracking	100, 200 and 300‡ (boiling point of H_2SO_4 is 327-340 °C at 100 kPa)	H_2SO_4; pH = 1; Test durations = 1, 2, 4 and 8 months

* Due to equipment failure and funding constraints, testing could not be performed beyond 300 °C for CGR studies.
† The Instron furnace failed after 500 °C and due to funding constraints testing was stopped at that point.
‡ The autoclave could only be operated up to a temperature of 100 °C.

CHAPTER 2

TEST MATERIAL, SPECIMENS AND ENVIRONMENT

2.1 Test Material

As indicated in the previous chapter, Alloy 276 has been identified to be one of the candidate structural materials for heat exchanger application in hydrogen generation using nuclear heat through chemical reactions associated with the S-I process. The identification of this Ni-base superalloy was based on its superior tensile properties, and excellent corrosion resistance in many hostile environments encountered by numerous chemical processing plants, as cited in the open literature [2-5]. However, very little or no data exist as to its mechanical properties at temperatures up to 1000 °C, and corrosion behavior in the presence of chemical species relevant to the S-I process. Therefore, different types of testing has been performed in this investigation using state-of-the-art techniques to evaluate the metallurgical, mechanical, and corrosion properties of Alloy 276. This chapter contains a detailed discussion on the metallurgical aspects of this Alloy, the types of testing specimens used, and the aqueous environment used in the corrosion testing.

Alloy 276 was originally developed by the Haynes International Inc. for many industrial applications due to its exceptional capability to withstand severe operating conditions including hostile corrosive environments, elevated temperatures, high stresses and a combination of all of them. The excellent ductility and toughness of this alloy can be attributed to its stable FCC crystal structure maintained even up to its melting temperature. The presence of Ni in this alloy enables significant plastic deformation in multiple slip planes, thus leading to enhanced ductility until failure under tensile loading.

Further, the presence of high Cr content provides significantly high resistance to environment-induced degradations in normal atmosphere, seawater, and acidic environments [10, 11]. This alloy is known to be resistant to different forms of corrosive degradations in many strong acidic solutions such as H_2SO_4 and hydrochloric acid (HCl) even in the presence of chlorides at ambient temperature. In addition, significant resistance to localized corrosion can be achieved with this alloy due to the presence of Mo. The presence of high levels of Ni, Cr and Mo in Alloy 276 can make this alloy sufficiently resistant to H_2S-containing environments even at elevated temperatures, as encountered in deep oil and gas wells.

Alloy 276 is readily weldable and can outperform many commercially available stainless steels. This material can be used in the as-welded conditions, eliminating the need for post-weld thermal treatments. The presence of significantly low carbon and silicon contents in Alloy 276 is beneficial to prevent grain boundary precipitation/segregation during heating cycles associated with the welding operations. The typical physical properties of Alloy 276 are given in Table 2-1 [2, 12].

Table 2-1 Physical Properties of Alloy 276

Physical Property	Temperature (°C)	Metric Units
Density	22	8.89 g/cm^3
Melting Range	1323-1371	--
Electrical Resistivity	24	1.30 microhm-m
Mean Coefficient of Thermal Expansion	24-93	11.2 x 10^{-6}m/m.K
Thermal Conductivity	38	10.2 W/m.K
Specific Heat	Room	427 J/Kg.K

Alloy 276, tested in this investigation, was procured from two vendors in properly heat-treated conditions. This heat treatment consisted of solution-annealing at 1163 °C (2125 °F) followed by rapid cooling, thus providing a fully austenitic microstructure. Both round and flat bars were procured to fabricate different types of test specimens. The chemical compositions and the ambient-temperature tensile properties of two heats of Alloy 276, in the as-received conditions, are given in Tables 2-2 and 2-3 [13, 14], respectively. No additional thermal treatments were given to these materials prior to the fabrication of the test specimens.

Table 2-2 Chemical Composition of Alloy 276 (wt %)

Heat No.	C	Mn	P	S	Si	Fe	Ni	Cr	Mo	Co	V	W
Z7437CG	0.006	0.42	0.002	0.001	0.008	5.94	58.33	15.84	15.93	0.10	<0.01	3.42
2760 6 3671	0.002	0.47	0.009	0.001	0.04	5.47	57.48	15.73	15.28	1.82	0.03	3.67

Table 2-3 Ambient-Temperature Tensile Properties of Alloy 276

Heat No.	Yield Strength, ksi (MPa)	Ultimate Tensile Strength, ksi (MPa)	%El	Hardness, R_B
Z7437CG	51 (354)	117 (807)	84	84
2760 6 3671	52 (359)	113 (779)	90	79

2.2 Test Specimens

The crack-growth behavior of Alloy 276 under cyclic loading, and its fracture toughness were evaluated by using compact-tension (CT) specimens based on

conventional fracture-mechanics concepts. Fracture-mechanics-based double-cantilever-beam (DCB) specimens were also machined from the plate materials to evaluate the susceptibility of this alloy to stress-corrosion-cracking (SCC), and estimate the average crack-growth-rate (CGR) as a function of stress intensity factor (K) in an acidic solution for a variable exposure period. Further, smooth cylindrical specimens were machined from the round bars of this alloy to evaluate its creep properties at different temperatures.

2.2.1 Compact-Tension Specimen

2.2.1.1 Crack-Growth-Rate Evaluation

Pre-cracked CT specimens having 1.25-inches (31.75 mm) length, 1.2-inches (30.48 mm) width and 0.25-inch (6.35 mm) thickness (Figure 2-1) were used to determine the crack-growth-rate (CGR) of Alloy 276. The machining of these specimens was done in compliance with the size requirements prescribed by the ASTM designation E 647-2000 [15]. The intersection of the crack starter notch tips with the two specimen surfaces were made equidistant from the top and bottom edges of the specimen within 0.005W, where W is the width of the specimen. A root radius of 0.003-inch (0.25 mm) was provided for the straight-through slot terminating in the V-notch of the specimen to facilitate fatigue pre-cracking at low stress intensity levels. A W/B ratio of 4 was maintained while machining the CT specimens [15], where B is the thickness of the specimen.

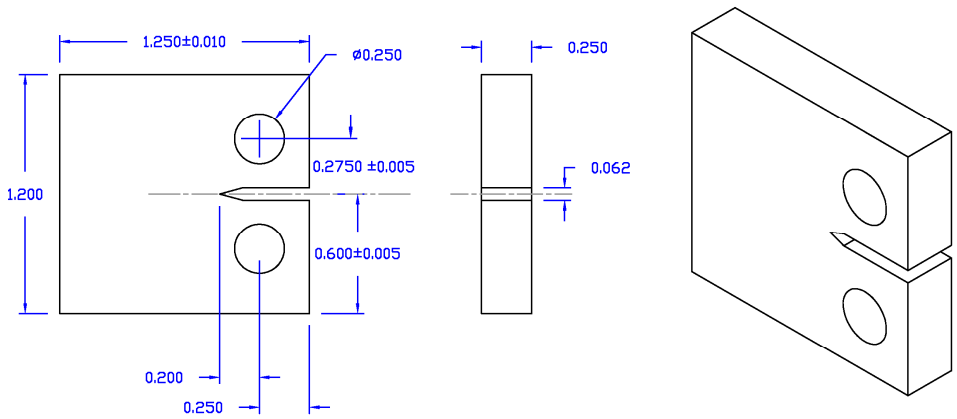

(a) Specimen Dimensions in Inches

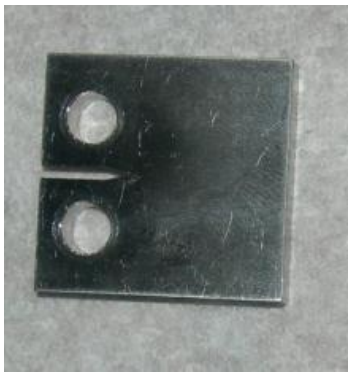

(b) Pictorial View

Figure 2-1 CT Specimen used in CGR Testing

2.2.1.2 Fracture Toughness Evaluation

For fracture toughness (J_{IC}) evaluation, pre-cracked CT specimens having 2.5-inches (63.5 mm) length, 2.4-inches (60.96 mm) width and 1-inch (25.4 mm) thickness, shown in Figure 2-2, were used. These specimens were machined in compliance with the size requirements prescribed by the ASTM designation E 813-1989 [16]. A root radius of 0.003-inch (0.25 mm) was provided for the straight-through slot terminating in the V-

notch of the specimen to facilitate fatigue pre-cracking at low stress intensity levels. A W/B ratio of 2 was maintained in machining these CT specimens [16], where B is the thickness of the specimen.

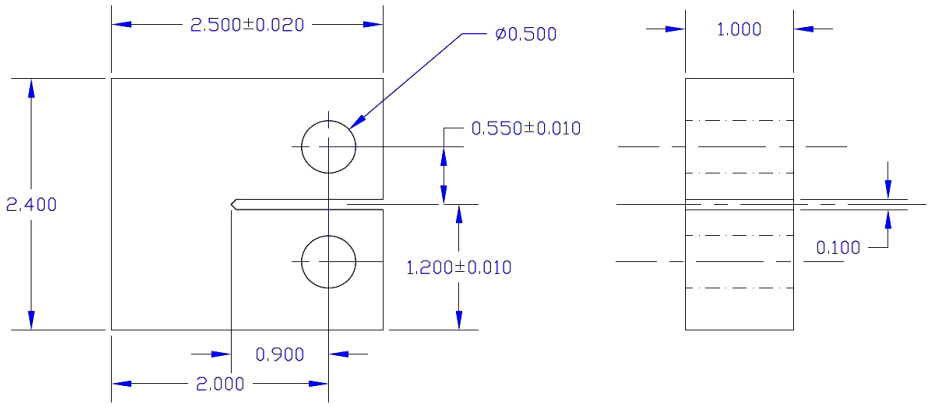

(a) Specimen Dimensions in Inches

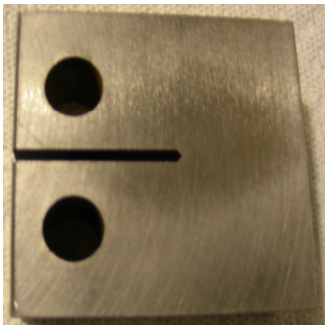

(b) Pictorial View

Figure 2-2 CT Specimen used in J_{IC} Testing

2.2.2 Double-Cantilever-Beam Specimen

Rectangular double-cantilever-beam (DCB) specimens, 4-inches (101.6 mm) long, 1-inch (25.4 mm) wide and 0.375-inch (9.525 mm) thick with one end slotted for wedge-loading and V-shaped side grooves extended from the slot to the opposite end, were used

for the SCC study. These specimens were machined according to the NACE Standard TM0177-1990 [17]. The side grooves were machined as 20% of the wall thickness, thus maintaining a web thickness (B_n) equal to 60% of the wall thickness (i.e. 0.225-inch or 5.715 mm in this case). The fabrication of the DCB specimens was done in such a way that the crack plane was perpendicular to the short transverse direction, thus ensuring that crack propagation would occur in the longitudinal rolling direction. Machining of the side grooves was done carefully to avoid overheating and cold working. The final two passes in machine operations removed a total of 0.002-inches (0.05 mm) of the metal.

The pre-cracked DCB specimens were loaded by inserting double taper wedges, made of Alloy 276, into the specimen slots. Wedges of different thickness were inserted into the DCB slot to apply the desired load. Thus, the arm-displacement due to the insertion of the wedge resulted in different initial stress intensity factor values. The thickness of the wedge was varied from 0.11-inch (2.8 mm) to 0.124-inch (3.14 mm), as shown in Table 2-4. The dimensions of the DCB specimen, and a pictorial view of the wedge-loaded DCB specimen are illustrated in Figure 2-3 (a and b). A pictorial view of the wedge is shown in Figure 2-4.

Table 2-4 DCB Wedge Thickness

Specimen Number	Test Duration [Month(s)]	Wedge Thickness (mm)
1 (High initial load)	1	3.11
2 (High initial load)	2	3.12
3 (High initial load)	4	3.14
4 (High initial load)	8	3.13
5 (Low initial load)	1	2.93
6 (Low initial load)	2	2.88
7 (Low initial load)	4	2.85
8 (Low initial load)	8	2.80

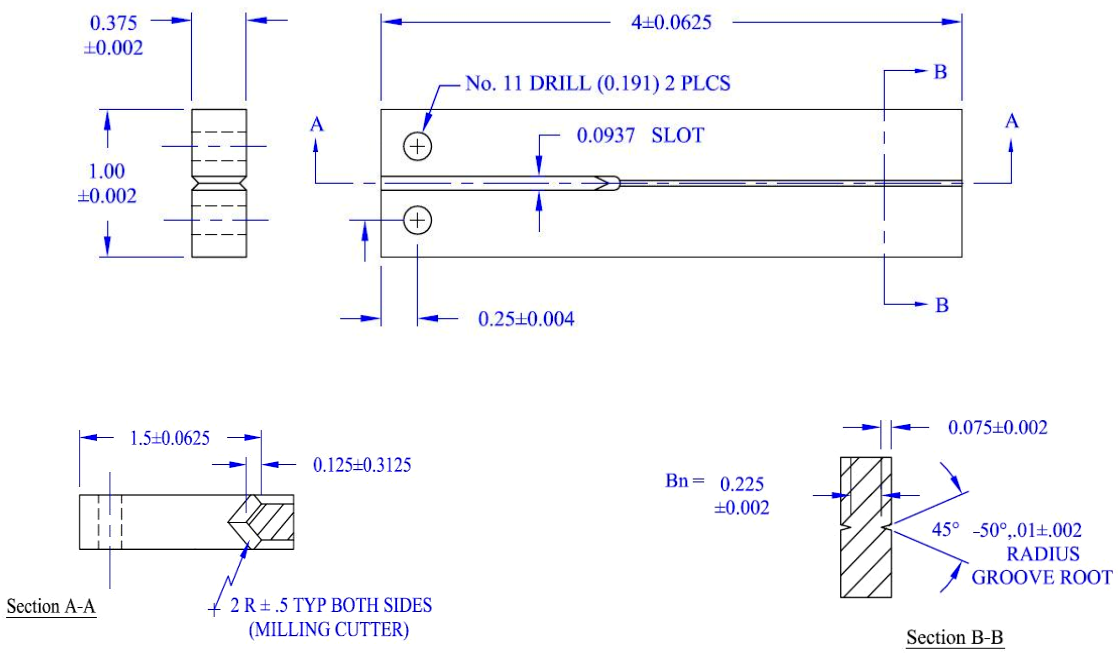

(a) Specimen Dimensions in Inches

(b) Pictorial View

Figure 2-3 Wedge-Loaded DCB Specimen

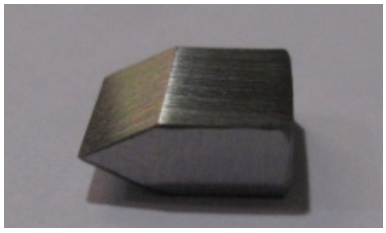

Figure 2-4 Double Taper Wedge

2.2.3 Creep Test Specimen

A schematic view of the smooth cylindrical specimen used in tensile testing is shown in Figure 2-5. The data from tensile testing were used in determining the stress values for creep testing. For creep testing, smooth cylindrical specimens having an overall length of 4-inches (101.6 mm) and a gage length of 1.48-inches (37.59 mm) were used. A ratio of 6:1 was maintained between the gage length and diameter. The test specimens were fabricated in such a way that the gage section was parallel to the longitudinal rolling direction. Specimens were machined according to the size requirements prescribed by the ASTM Designation E 139-2000 [18]. Circular grooves were machined at both ends beyond the shoulder region of the specimens to attach dual extensometers for monitoring elongation during creep testing. The dimensions and a pictorial view of the creep specimen is illustrated in Figure 2-6 (a and b).

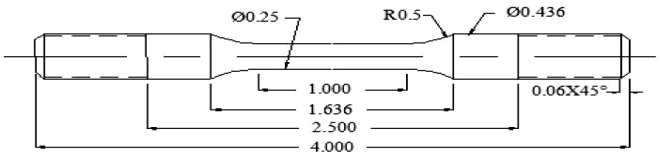

Figure 2-5 Tensile Specimen Dimensions in Inches

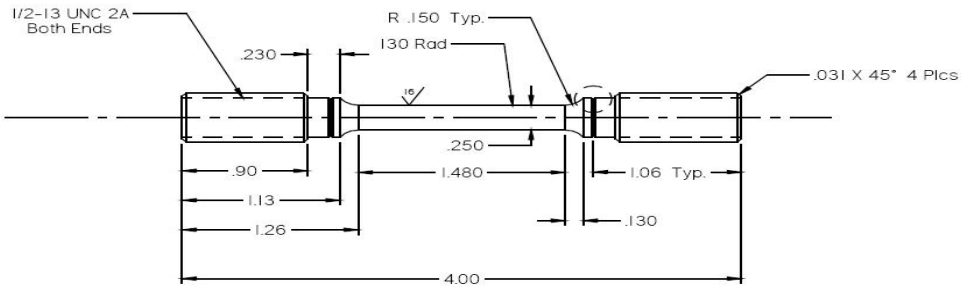

(a) Specimen Dimensions in Inches

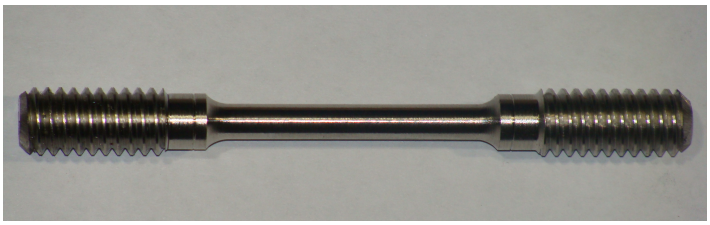

(b) Pictorial View

Figure 2-6 Creep Specimen

2.3. Test Environment

Environment can have a profound effect on the performance of structural materials to be used in heat-exchangers associated with the nuclear hydrogen generation process. Even though the S-I process involves the formation and decomposition of H_2SO_4 and HI at different temperatures, a prototypic environmental condition could not be accommodated in the corrosion testing due to a lack of proper infrastructure. Therefore, an effort was made to evaluate the corrosion behavior of Alloy 276 in an aqueous solution containing H_2SO_4 at the highest possible temperature (100 °C) at the Materials Performance Laboratory without having any leakage of the testing equipment (autoclave). The composition of the testing solution is given in Table 2-5.

Table 2-5 Chemical Composition of Test Solution

Solution (pH)	Deionized Water (ml)	H_2SO_4
Acidic (1.0)	4000	Added to adjust the desired pH

CHAPTER 3

EXPERIMENTAL PROCEDURES

Crack propagation behavior of Alloy 276 was studied at temperatures ranging from ambient to 300 °C using a mechanical testing equipment manufactured by the Instron Corporation (model 8862). This equipment was also used to determine the fracture toughness (J_{IC}) values of this alloy at temperatures up to 500 °C, after which point the furnace cooling system failed. Additionally, pre-cracking of the double-cantilever-beam (DCB) specimens, used in the determination of stress intensity factor (K) values for stress-corrosion-cracking (SCC) under a wedge-loaded condition, was performed in this machine. Efforts were also made to evaluate time-dependent deformation (creep) of Alloy 276 under sustained loading in load frames (model 8330) manufactured by the Applied Test Systems Corporation (ATS). The metallographic and fractographic evaluations of all tested specimens were performed using optical microscopy and scanning electron microscopy (SEM), respectively. The characterization of linear lattice defects (dislocations), and precipitates resulting from plastic deformation and metallurgical changes at different testing temperatures was performed by transmission electron microscopy (TEM). The detailed procedures used in these tests are described in the following subsections.

3.1 Crack-Growth-Rate Testing

Crack-growth-rate (CGR) testing involving compact-tension (CT) specimens of Alloy 276 was performed in accordance with the ASTM Designation E 647-2000 [15]. Testing was performed at temperatures ranging from ambient to 300 °C under three different load ratios (R = Minimum load/Maximum load) of 0.1, 0.2 and 0.3, keeping the frequency of

loading at 1 Hz. Prior to CGR testing, the CT specimens were pre-cracked up to a length of 2 mm under cyclic loading. Testing was performed using a constant maximum load P_{max} of 5 kN, and the magnitude of minimum load P_{min} was varied to maintain R values of 0.1, 0.2, and 0.3, respectively. The magnitudes of maximum and minimum stresses σ_{max} and σ_{min} were determined from P_{max} and P_{min}, which were used to calculate the maximum and minimum stress intensity factor values K_{max} and K_{min}.

3.1.1 Instron Testing Machine

The Instron testing machine, shown in Figure 3-1, had an axial load transducer capacity of 22.5 kip (100 kN). It had a single screw electromechanical top actuator that was developed for static and quasi-dynamic cyclic testing at slow speed. This equipment consisted of a large heavy-duty load frame with an adjustable crosshead attached to the top grip, and a movable actuator with another grip at the bottom to enable loading and unloading of the test specimen. The axial motion was controlled by force, displacement, or an external signal from the strain gage. The specimen was mounted between the two grips and pulled by the movable actuator. The load cell measured the applied force on the CT specimen. The movement of the upper crosshead relative to the lower one measured the strain within the specimen and consequently, the applied load. The key specifications of the Instron equipment are given in Table 3-1 [19].

Table 3-1 Specifications of Instron Model 8862 System

Load Capacity	Total Actuator Stroke	Maximum Ramp Rate	Actuator Attachment Threads	Load Cell Attachment Threads
100 kN	100 mm	350 mm/min	M30 × 2	M30 × 2

A split furnace (model MDS1735A) was attached to the testing system for elevated temperature testing. This furnace was capable of sustaining a maximum temperature of 1500 °C, and consisted of two water-cooled stainless steel jackets that provided a safe ergonomic outer surface for operation. This furnace had two layers of micro-pores and ceramic fibers over them. Six U-shaped molybdenum disilicide heating elements were used for attaining the desired testing temperature. The specimen temperature during testing was monitored by three B-type thermocouples contained inside the test chamber. A separate control panel (model CU666F) was used to perform the overall monitoring of temperature during testing. By design, a maximum heating rate of 10 °C per minute could be achieved by this control panel. However, a slow heating rate of 4 °C per minute was used during CGR and fracture toughness testing to prevent any thermal shock of the pull rods and the fixtures inside the furnace. Since the grip material could undergo phase transformation and plastic deformation at elevated temperatures during straining of the specimen, a pair of custom-made grips of high strength and temperature resistant MarM 246 alloy was used to hold the specimen in an aligned position.

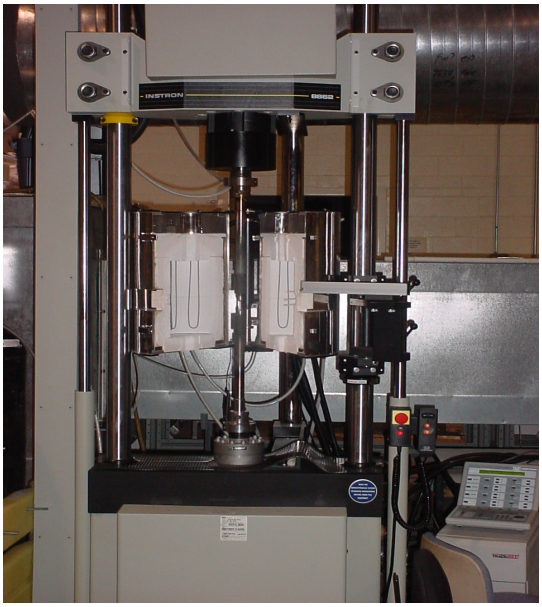

Figure 3-1 Instron Testing Machine

3.1.2 DCPD Crack Monitoring Device

The CGR was measured using an in-situ crack monitoring technique, known as direct-current-potential-drop (DCPD). In this process, the changes in crack length were measured from the potential or voltage drop between the two arms of the specimen as crack propagates [20-23]. Two wires (current probes) were attached (spot-welded) to the top and bottom faces of the specimen, as shown in Figure 3-2, which allowed the flow of constant current (3 amps) into the specimen. Two additional wires (voltage/potential probes) were welded to the arms of the specimen that measured the resultant potential drop due to an increase in resistance resulting from the extension of the crack length under the influence of cyclic loading. The applied current was provided by a PD-501 Amplifier (Figure 3-3), and the resultant voltage drop was recorded and analyzed by an ADwin-GOLD controller, shown in Figure 3-4. As the crack length increases, the gap between the two loaded arms of the specimen increases, thus, the electrical resistance

increases. This increase in electrical resistance gives rise to an increase in potential difference or voltage drop between the two arms of the specimen spanning the crack length, which was recorded by use of a software program [24] provided by the 'Fracture Technology Associates (FTA)'. The potential drop was converted to crack extension using Johnson's Formula [25-28], given by Equation 3-1.

$$a = \frac{W}{\pi}\cos^{-1}\left[\frac{\cosh\left(\frac{\pi}{W}\times Y_o\right)}{\cosh\left[\frac{V}{V_r}\times\cosh^{-1}\left[\frac{\cosh\left(\frac{\pi}{W}\times Y_o\right)}{\cos\left(\frac{\pi}{W}\times a_r\right)}\right]\right]}\right] \qquad \text{Equation 3-1}$$

where

a = Crack size, mm

a_r = Reference crack size, mm

W = Specimen width, mm

V = Measured potential drop, volt

V_r = Measured voltage corresponding to a_r

Y_o = Voltage measurement lead spacing from the crack plane

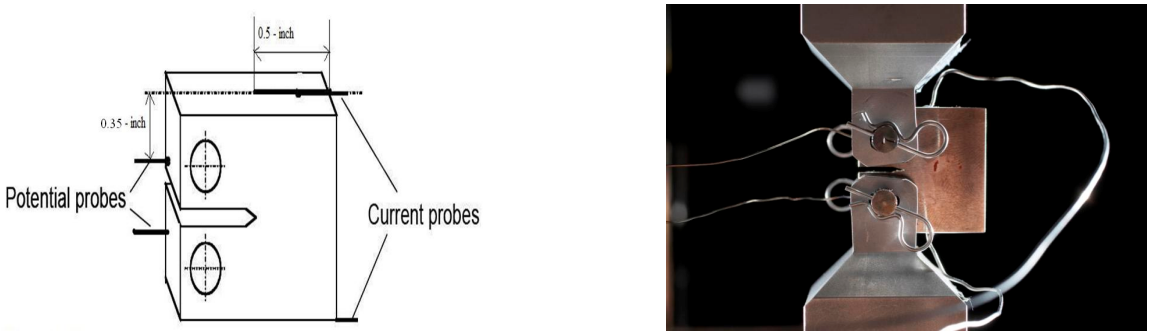

Figure 3-2 DCPD Test Setup

Figure 3-3 PD-501 Amplifier

Figure 3-4 ADwin-GOLD Controller

At the end of each test, the FTA software program enabled the analyses of the recorded data, and subsequently generated plots of da/dN versus ΔK, showing a three-stage curve including a threshold crack-growth, steady-state crack-growth, and an unstable crack-growth regions. The steady-state crack-growth region is generally governed by the Paris Law [29-31], given by Equation 3-2, also known as the Paris regime. A classical da/dN versus ΔK plot, showing these three regions is illustrated in Figure 3-5 [32].

$$da/dN = A\,(\Delta K)^m \qquad \text{Equation 3-2}$$

where

da/dN = Crack-growth-rate, mm/cycle

ΔK = Stress intensity factor range ($K_{max} - K_{min}$), MPa√m

K_{max} = Maximum stress intensity factor (MPa√m)

K_{min} = Minimum stress intensity factor (MPa√m)

A = Crack-growth coefficient, MPa√m

m = Slope of the linear portion of log da/dN versus log ΔK plot

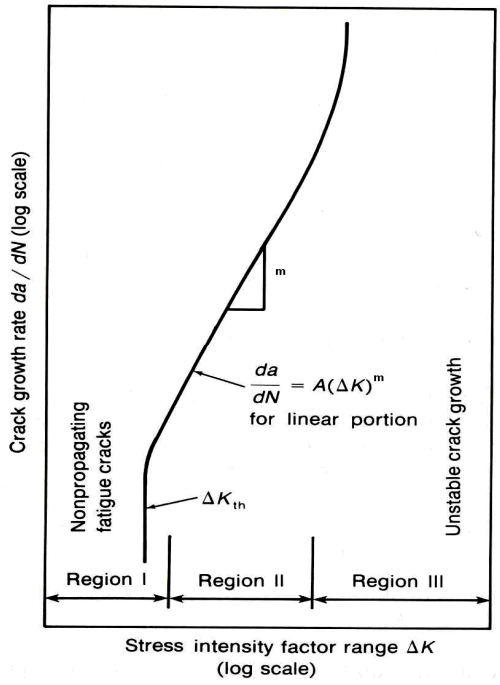

Figure 3-5 da/dN vs. ΔK Plot

The overall data generated from CGR testing, and the resultant plots include the magnitudes of m and A, and the number of cycles to failure N_f. Further, the magnitude of threshold stress intensity factor range (ΔK_{th}) can also be determined that represent a ΔK value below which no crack-growth of the tested material occurs even under cyclic loading [15]. However, for all tested conditions, the magnitude of ΔK_{th} was taken to be equivalent to a ΔK value that corresponds to a da/dN value of 10^{-7} mm/cycle [15]. The magnitude of N_f was calculated by using Equation 3-3, given below [8].

$$N_f = \left[\frac{a_f^{\left(1-\frac{m}{2}\right)} - a_i^{\left(1-\frac{m}{2}\right)}}{A\left(\sigma_r\right)^m \alpha^m \pi^{\frac{m}{2}}}\right]\left[\frac{1}{1-\frac{m}{2}}\right] \qquad \text{Equation 3-3}$$

where

a_f = Final crack-length, mm

a_i = Initial crack-length, mm

σ_r = Stress range ($\sigma_{max} - \sigma_{min}$), MPa

σ_{max} = Maximum stress, MPa

σ_{min} = Minimum stress, MPa

α = Geometric factor of the specimen (5.317), determined by using Equation 3-4 for a 0.25-inch thick CT specimen

$$\alpha = \frac{\left[2+\frac{a_i}{W}\right]\left[0.886+4.64\left(\frac{a_i}{W}\right)-13.32\left(\frac{a_i}{W}\right)^2+14.72\left(\frac{a_i}{W}\right)^3-5.6\left(\frac{a_i}{W}\right)^4\right]}{\left(1-\frac{a_i}{W}\right)^{\frac{3}{2}}} \quad \text{Equation 3-4}$$

where

W = Width of the CT specimen, mm

3.1.3 Activation Energy Evaluation

It is well known [33] that crack tip stresses developed under cyclic loading are sufficiently high to cause plastic deformation, leading to instantaneous generation and multiplication of lattice defects such as dislocations, eventually causing dislocation pile-ups near grain boundaries. Thus, no thermal activation is needed. However, the movement of dislocations is a thermally- activated process. Dislocation motion can cause plastic crack-extension, which is also expected to be thermally activated with activation energy (Q) being the same as that for dislocation movement. If m is considered to be independent of the testing temperature, Equation 3-2 can be modified to Equation 3-5, taking Q into consideration for crack-growth [33-36].

$$da/dN = A_o\,[\exp(-Q/RT)]\,(\Delta K)^m \quad \text{Equation 3-5}$$

where

R = Universal gas constant, 8.314 J/mol.K

A_o = A material constant, which is independent of temperature, and can be related to A, as shown in Equation 3-6 [33-36]

$$A = A_0 [\exp (-Q/RT)] \quad \text{Equation 3-6}$$

Taking natural logarithm on both sides of Equation 3-6 and re-arranging, one can get

$$\ln (A) = [-Q/R]1/T + \ln (A_0) \quad \text{Equation 3-7}$$

Equation 3-7 represents a straight line with a slope and an intercept of –Q/R and ln (A_0), respectively, when ln (A) is plotted against 1/T. Using the value of R, one can determine the magnitude of Q.

3.1.4 CGR Testing at Constant K_{max}, K_{min} and ΔK

Efforts were also made to determine CGR of Alloy 276 under constant K_{max}, K_{min} and ΔK values at ambient temperature, while maintaining an R value of 0.1. It should be noted that, as crack propagated under constant K values, the maximum and minimum loads P_{max} and P_{min} values were automatically adjusted by the software used to maintain constant values of K_{max} and K_{min} , and thus, a constant ΔK value, too. The magnitudes of K_{max}, K_{min} and ΔK used in constant-K CGR testing are given in Table 3-2.

Table 3-2 K_{max}, K_{min} and ΔK Values used in Constant-K Testing

Specimen No.	K_{max} (MPa√m)	K_{min} (MPa√m)	ΔK (MPa√m)
1	26.25	2.625	23.62
2	27.63	2.763	24.87
3	29.07	2.907	26.17

3.2 Fracture Toughness Evaluation

Initially, attempts were made to evaluate the fracture toughness of Alloy 276 in terms of plane strain fracture toughness (K_{IC}), based on the linear-elastic-fracture-mechanics (LEFM) concept [8]. However, the determination of K_{IC} was not feasible from a practical standpoint since significantly thicker CT specimens were needed to comply with the LEFM criterion. Therefore, elastic-plastic-fracture-mechanics (EPFM) concept was used to evaluate the fracture toughness of this alloy in terms of J_{IC} involving 1-inch thick CT specimens. The determination of J_{IC} was based on a procedure prescribed by the ASTM Designation E 813-1989 [16].

In essence, two types of J_{IC} testing method exist [16], namely single-specimen technique and multiple-specimen technique. The multiple-specimen technique [16] requires at least five specimens to be tested at a particular temperature to determine the J_{IC} value. Hence, to reduce both cost and time, and because the single-specimen technique is equally reliable as the multiple-specimen technique, the former technique was used to determine the J_{IC} value of Alloy 276 in this study using the Instron testing machine. Testing was conducted at temperatures ranging from ambient to 500 °C. A 'J_{IC} Fracture Toughness Software' [37], provided by the Instron Corporation, was used to calculate and validate the J_{IC} value. The detailed procedure associated with such evaluation is described next.

The CT specimen was pre-cracked to an approximate length of 3 mm using an R value of 0.1 and a frequency of 1 Hz. The maximum load used in pre-cracking was based on Equation 3-8 [16], which was maintained at 20 kN. Following pre-cracking, the specimen was subjected to thirty loading and unloading cycles. Due to these

loading/unloading cycles, the load-line-displacement (LLD) or, the crack-opening-displacement (COD) i.e. the gap between the two arms of the CT specimen was enhanced. The LLD was measured by a high-temperature knife-edge extensometer, which was attached to the specimen arms at the onset of testing. The maximum travel distance of the extensometer was kept at +/- 2 mm. The J_{IC} test setup used in this investigation is shown in Figure 3-6. A typical load versus LLD plot is shown in Figure 3-7 (a).

$$P_L = \frac{Bb_0^2\sigma_Y}{(2W+a_0)} \qquad \text{Equation 3-8}$$

where

P_L = Maximum load during pre-cracking, N

B = Thickness of the specimen, mm

b_0 = Uncracked ligament, mm

σ_Y = Effective yield strength of the material, MPa

W = Width of the specimen, mm

a_0 = Pre-crack length, mm

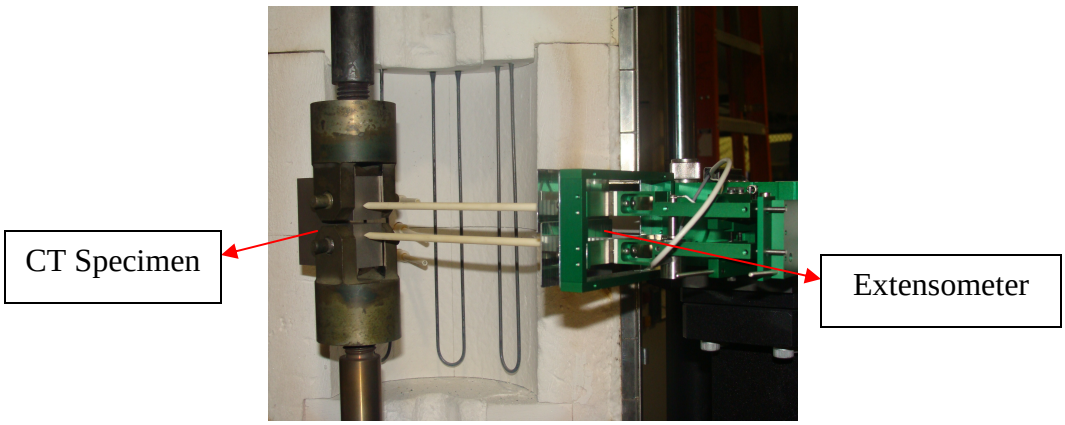

Figure 3-6 J_{IC} Test Setup

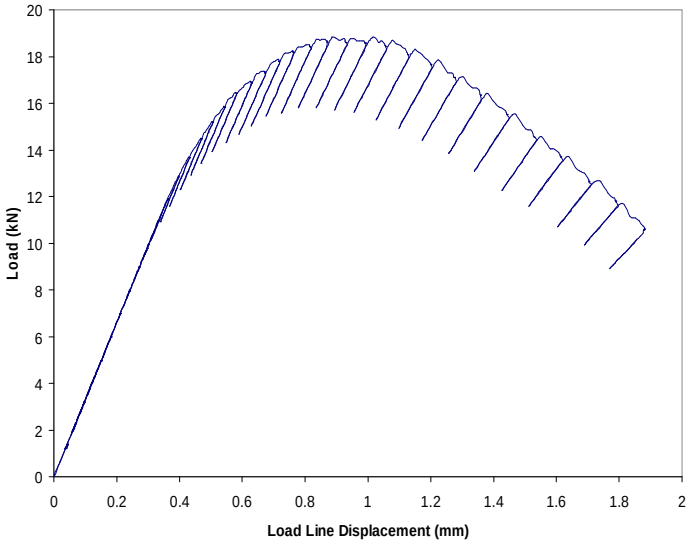

Figure 3-7 (a) Load versus LLD Plot

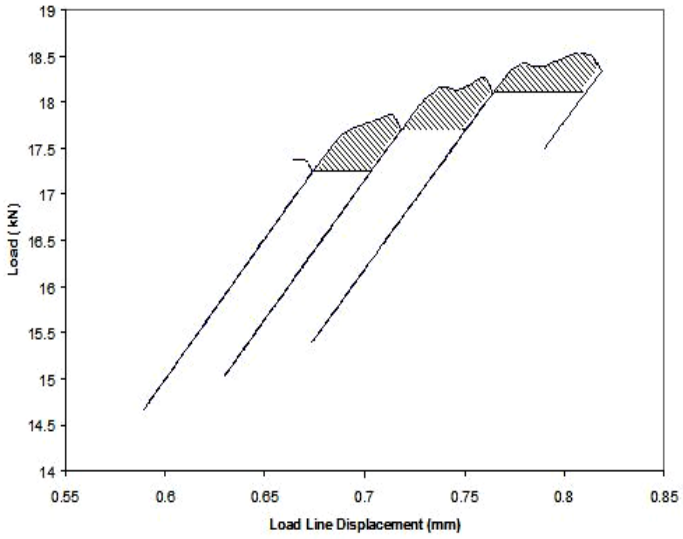

Figure 3-7 (b) Areas Representing J-Integral

The shaded area corresponding to each loading/unloading cycle, shown in Figure 3-7 (b), represents the energy (J-Integral) needed to cause an increment in crack length. The

crack increases by a certain amount during each loading/unloading sequence. The J-Integral value for each area was calculated using Equation 3-9 [16, 38].

$$J = J_{elastic} + J_{plastic} \quad \text{Equation 3-9}$$

where

$$J_{elastic} = \frac{K^2}{E}\left[1 - \nu^2\right], \text{ and} \quad \text{Equation 3-10}$$

$$J_{plastic} = \frac{\eta_{pl}}{Bb}\int_0^{v_{pl}} Pdv_{pl} = \frac{\eta_{pl}}{Bb} \times A_{pl} \quad \text{Equation 3-11}$$

$$K = \text{Stress intensity factor} \left[\frac{P}{\left(BB_N W\right)^{0.5}}\right] \times \alpha, \text{ MPa}\sqrt{\text{m}}$$

P = Load, N

B = Specimen thickness, mm

B_N = Net specimen thickness = B (in present study), mm

W = Width of the specimen, mm

α = Geometric factor of the specimen

E = Elastic modulus of the material

ν = Poisson's ratio of the material (0.3)

b = Uncracked ligament, mm

$\eta_{pl} = 2 + 0.522b/W$

ν_{pl} = LLD / COD

A_{pl} = Area corresponding to each loading / unloading sequence, mm^2

The calculated J value was then plotted against the corresponding crack extension, as shown in Figure 3-8. The crack extension (a_i) for each sequence was measured by the unloading compliance principle, given by Equation 3-12 [16].

$$a_i/W = 1.000196 - 4.06319u_{LL} + 11.242u_{LL}^2 - 106.043u_{LL}^3 + 464.335u_{LL}^4 - 650.677u_{LL}^5$$

Equation 3-12

where

$$u_{LL} = \frac{1}{\left[B_e E C_i\right]^{0.5} + 1}$$

B_e = Effective thickness of the CT specimen = $[B - (B - B_N)^2/B] = B$ (since $B = B_N$ in the current study), mm

C_i = Specimen load line elastic compliance on an unloading/reloading sequence ($\Delta v/\Delta P$), mm/N

Δv = Increment in LLD/COD, mm

ΔP = Change in load, N

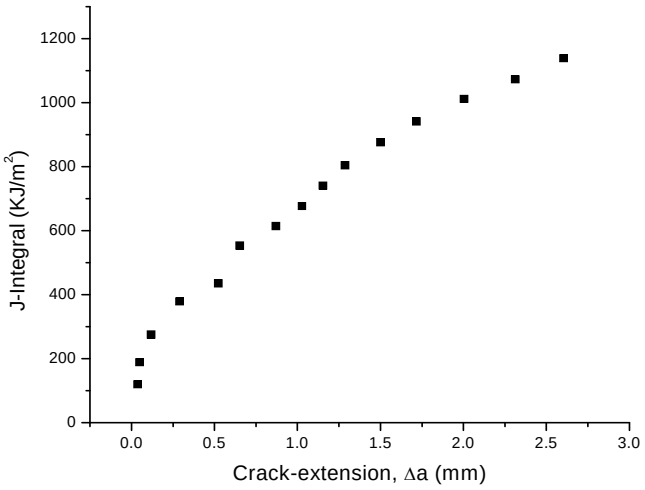

Figure 3-8 J-Integral vs. Crack-Extension

The data shown in Figure 3-8 were fitted to a power law regression curve, and four parallel lines were then drawn, as shown in Figure 3-9. These lines are referred to as the

blunting line, 0.15-mm exclusion line, 0.2-mm exclusion line, and 1.5-mm exclusion line. The blunting line was drawn using Equation 3-13, and all other lines were drawn parallel to it. The J - Δa data are considered to be valid if at least one J - Δa point lies between the 0.15-mm exclusion line and a line parallel to the blunting line at an offset of 0.5-mm from the blunting line.

$$J = 2\sigma_Y \Delta a \qquad \text{Equation 3-13}$$

The point of intersection of the regression curve and the 0.2-mm exclusion line (as shown in Figure 3-9) is usually taken as J_Q, or the conditional J_{IC} value. J_Q is considered to be the J_{IC} value if the following two criteria are met.

i. Thickness (B) of the specimen > [25 J_Q / σ_Y], where σ_Y = effective yield strength of the material = average of the yield and ultimate tensile strength (σ_{YS} and σ_{UTS}, respectively) of the material = [σ_{YS} + σ_{UTS}] / 2, and

ii. Initial uncracked ligament (b_0) > [25 J_Q / σ_Y]

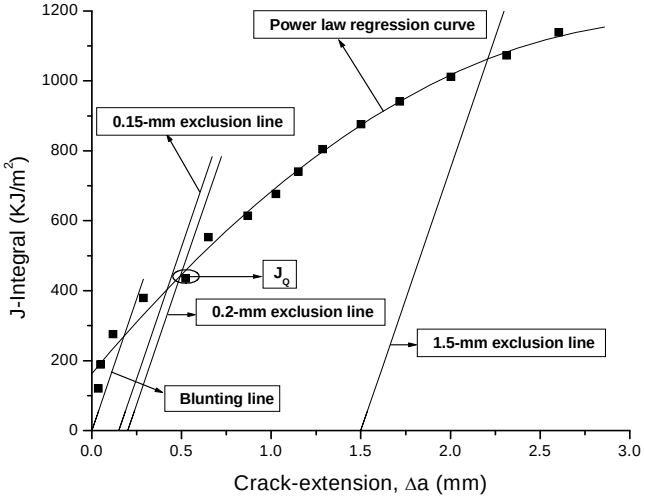

Figure 3-9 Determination of J_Q from J-Integral vs. Δa Plot

Efforts were also made to correlate J_{IC} to K_{IC}. Literature [8, 39, 40] suggests that K_{IC} can be calculated from the J_{IC} value according to Equation 3-14, as given below.

$$K_{IC} = \sqrt{J_{IC} \times E / \left(1 - \nu^2\right)} \qquad \text{Equation 3-14}$$

Fracture toughness can also be measured using the crack-tip-opening-displacement (CTOD) method, which is based on Equation 3-15, given below [8, 41].

$$\delta = \frac{K_I^2}{mE\sigma_{YS}} \qquad \text{Equation 3-15}$$

where

δ = CTOD, mm

$K_I = K_{IC}$ value of the material, MPa$\sqrt{m}$

m = Constant = 2 for plane-strain condition

3.2.1 Determination of Tearing Modulus

During fracture toughness testing, or loading in tension, an instability arises that can cause continuous crack extension by a so-called ‘tearing’ mechanism. The tearing modulus (T) of a material is defined as the material’s resistance to such instability, and can be given by Equation 3-16 [42-44].

$$T = \frac{E}{\sigma_Y^2} \frac{dJ}{da} \qquad \text{Equation 3-16}$$

where

dJ/da = Slope of the J-Δa curve

3.3 SCC Testing

Stress-corrosion-cracking (SCC) testing using DCB specimens of Alloy 276 was performed in a 100 °C acidic solution for exposure periods of 1, 2, 4 and 8 months. The

DCB specimens were loaded by inserting double-taper wedges of similar material with different thickness into their slots [17, 45, 46]. Prior to their loading, they were pre-cracked in the Instron equipment according to ASTM Designation E 399–1990 [47]. A cyclic loading with an R value of 0.1 and a frequency of 1 Hz was used in pre-cracking the DCB specimens. The wedge thickness was determined based on the linear portion (within the elastic region) of the load versus displacement curve of this alloy. A typical load versus displacement plot for a DCB specimen of Alloy 276 is shown in Figure 3-10. Two sets of load and displacement were selected to load the DCB specimens by inserting wedges of different thickness. The wedge thickness was calculated using Equation 3-17.

$$W = (t + \delta) \qquad \text{Equation 3-17}$$

where

W = Wedge thickness

t = Initial gap between the two arms of the DCB specimen

δ = Displacement corresponding to a desired load (from the load-displacement plot)

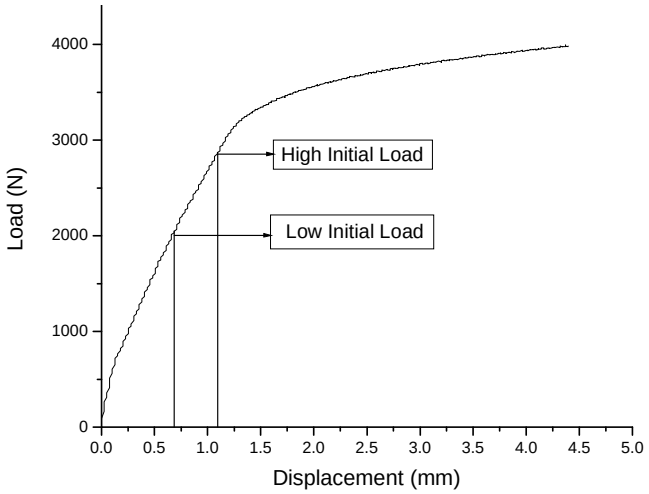

Figure 3-10 Load vs. Displacement Plot

The initial and the final stress intensity factor (K_I and K_f) values were computed using Equation 3-18, prescribed by the Nace Standard TM0177-1990 [17]. The pre-cracked and wedge-loaded DCB specimens were then immersed into an acidic solution contained in an autoclave (Figure 3-11).

$$K=\frac{Pa\left(2\sqrt{3}+2.38h/a\right)\left(B/B_n\right)^{1/\sqrt{3}}}{Bh^{3/2}} \qquad \text{Equation 3-18}$$

where

P = Wedge load (before or after exposure to the environment), measured in the loading plane

a = Initial or final crack length, measured from the load line

h = Height of each arm

B = Specimen thickness

B_n = Web thickness

Figure 3-11 DCB Test Setup

Upon completion of testing, the specimens were broken apart in the Instron machine, and the final crack length was measured on the broken faces [45, 46]. The final load and the crack length were used to calculate the final stress intensity factor (K_f) value due to SCC. Fractographic studies were subsequently conducted on the broken specimens to determine the extent and mode of cracking.

3.4 Creep Testing

Creep is a time-dependent deformation of a material at a constant load / stress [48, 49]. To generate a creep curve, a constant load is applied to a cylindrical specimen at a constant temperature, and the resultant strain is recorded as a function of time. Creep testing of Alloy 276 was performed at temperatures of 750, 850 and 950 °C according to ASTM Designation E 139-2000 [18]. The selection of the testing temperatures was based on an understanding that meaningful creep data could be generated at a homologous temperature (ratio of test temperature, T to melting temperature, T_m) of greater than or equal to 0.5 [18, 48]. Testing was performed in an ATS Series 2320 loading frame, having a lever arm ratio of 20:1. These loading frames had a ‘master’ and a ‘slave’ component in each unit. A split-furnace (model 3210) having three heating zones was attached to each load frame to achieve the desired testing temperature. A maximum temperature of 1100 °C could be accommodated using these furnaces. Kanthal A1 was used as a heating element in these furnaces. A pictorial view of the creep testing setup including the attached furnace is illustrated in Figure 3-12.

Figure 3-12 Creep Testing Setup

Four K-type thermocouples were used to monitor the testing temperature inside the furnace. Three thermocouples were firmly attached to the test specimen at the top, middle and bottom portion, respectively. A 'Windows Computer Creep System' (WINCCS) software was used to simultaneously monitor and record the instantaneous temperature at the top, middle and bottom location of the test specimen. The elongation at the gage section of the test specimen was measured by using two extensometers, as shown in Figure 3-13. The average elongation measured by the left and right extensometer was used to analyze the creep data. Creep testing was performed for a maximum period of 1000 hours at constant applied loads equivalent to 10 and 25% of the yield strength (YS) values of Alloy 276 at the testing temperature. The magnitudes of load and the corresponding initial stress values used in creep testing are given in Table 3-3.

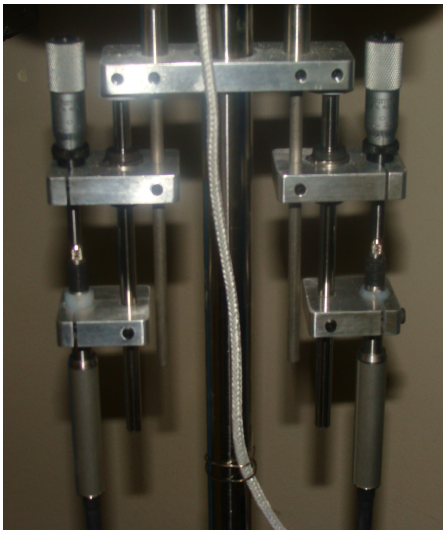

Figure 3-13 Extensometers used in Creep Testing

Table 3-3 Initial Stress and Load Values used in Creep Testing

Temperature, °C	Applied Stress = 0.10YS		Applied Stress = 0.25YS	
	Initial Stress, ksi (MPa)	Load, lbf	Initial Stress, ksi (MPa)	Load, lbf
750	2.95 (20.34)	50.74	7.38 (50.85)	126.85
850	2.84 (19.58)	48.85	7.10 (48.95)	122.12
950	2.29 (15.76)	39.30	5.71 (39.39)	98.26

At the end of each test, a three-stage creep curve was generated. The three regions of this curve are known as, primary, secondary and tertiary creep, respectively. A classical creep curve, showing three regions [50], is illustrated in Figure 3-14. At the onset of each creep test, there is an instantaneous elastic plus plastic strain (ε_0) resulting from the initial applied stress. The creep rate then decreases with time in the primary creep region, followed by a steady-state creep region. The slope of the secondary or steady-state creep curve ($d\varepsilon/dt$, or $\dot{\varepsilon}$) is known as creep rate of the tested material. Finally the creep rate increases rapidly, showing a steeper tertiary curve until failure.

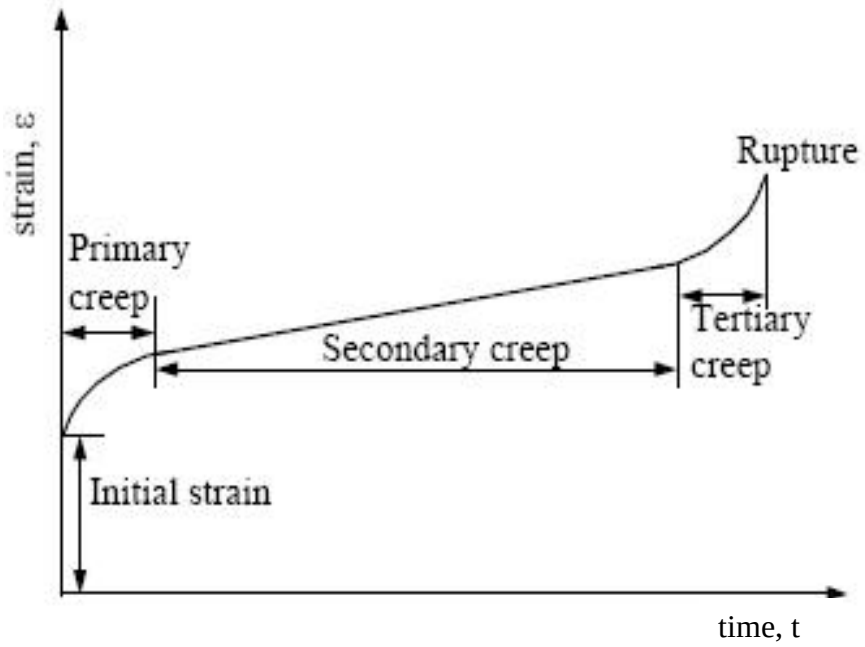

Figure 3-14 Three-Stage Creep Curve

3.4.1 Determination of Activation Energy

The steady-state creep rate of metals and alloys is a function of temperature. The driving force for deformation in the secondary stage is expressed in terms of an activation energy (Q). The magnitude of Q can be determined by three different techniques. One method of determination of Q is to consider Equation 3-19 [48], showing a temperature dependency of $\dot{\varepsilon}_s$.

$$\dot{\varepsilon}_s = A \exp(-Q/RT) \qquad \text{Equation 3-19}$$

where

$\dot{\varepsilon}_s$ = Steady-state creep rate, sec^{-1}

A = A pre-exponential complex constant containing the frequency of vibration of the flow unit, the entropy change, and a factor that depends on the structure of the material

T = Absolute temperature, K

Taking natural logarithms on both sides of Equation 3-19,

$$\ln (\dot{\varepsilon}_s) = [-Q/R] (1/T) + \ln (A) \qquad \text{Equation 3-20}$$

Equation 3-20 represents a straight line with an equation in the form of y = mx + c, when $\ln (\dot{\varepsilon}_s)$ is plotted against (1/T). The magnitude of Q can be calculated from the negative slope (-Q/R) by substituting the known value of R (gas constant).

The second method for determining the Q value is based on the consideration of Equation 3-21, which can be rearranged as Equation 3-22 for two testing temperatures of T_1 and T_2.

$$A = \dot{\varepsilon}_1 \exp (Q/RT_1) = \dot{\varepsilon}_2 \exp (Q/RT_2) \qquad \text{Equation 3-21}$$

$$Q = \frac{R \ln (\dot{\varepsilon}_1 / \dot{\varepsilon}_2)}{(1/T_2 - 1/T_1)} \qquad \text{Equation 3-22}$$

where

$\dot{\varepsilon}_1$ and $\dot{\varepsilon}_2$ = Steady-state creep rates at temperatures T_1 and T_2, respectively

The third method of Q calculation takes both temperature and stress dependency of steady-state creep rate into consideration, as given by Equation 3-23 [51]. The Q value can be computed from this equation by using three sets of $\dot{\varepsilon}$, σ and T values, and a related process of elimination.

$$\dot{\varepsilon} = A\sigma^{n}\exp\left(-Q/RT\right) \qquad \text{Equation 3-23}$$

where

$\dot{\varepsilon}$ = Minimum or steady-state creep rate, sec^{-1}

σ = Applied stress, MPa

n = Stress exponent

Q = Apparent activation energy for creep deformation, kJ/mole

A = A constant

3.5 Metallographic Evaluations

The metallographic technique, using an optical microscope, enables the characterization of phases present, their distributions within grains and their sizes that depend on both the chemical composition and the thermal treatment of the test material. The principle of an optical microscope is based on the impingement of a light source perpendicular to the test specimen. The light rays pass through the system of condensing lenses and the shutters up to the half-penetrating mirror. This brings the light rays through the objective to the surface of the specimen. Light rays are reflected off the surface of the sample, which then return to the objective, where they are gathered and focused to form the primary image. This image is then projected to the magnifying system of the eyepiece. The contrast observed under the microscope results from either an inherent difference in intensity or wavelength of the light absorption characteristics of the phases present. It may also be induced by preferential staining or attack of the surface by etching with a chemical reagent.

The test specimens were sectioned, and mounted using the standard metallographic technique, followed by polishing and etching to reveal their metallurgical

microstructures. The etchant used was composed of a mixture of 80 ml of concentrated hydrochloric acid (HCl), 4 ml of concentrated nitric acid (HNO_3) and 1 gm of cupric chloride ($CuCl_2$) [52]. The polished and etched specimens were then evaluated for determination of their microstructures in a Leica optical microscope, shown in Figure 3-15. This microscope was capable of resolution of up to 1000X. A digital camera with a resolution of 1 Mega pixel enabled the image capture on a computer screen, utilizing the Leica software.

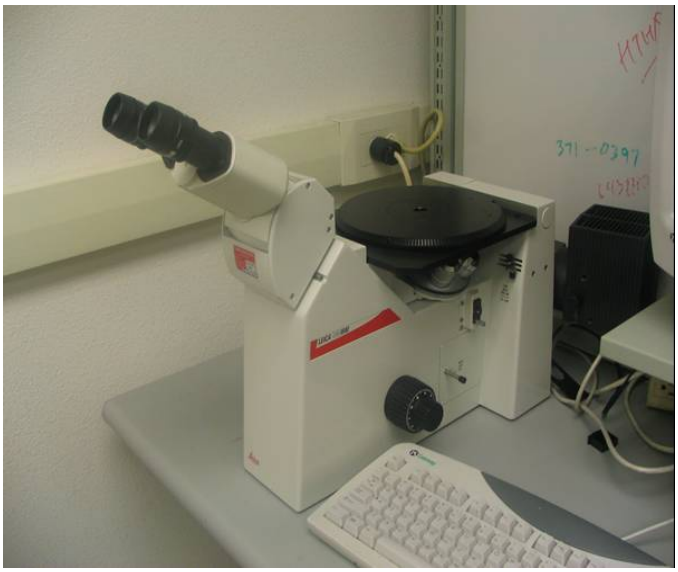

Figure 3-15 Leica Optical Microscope

3.5.1 Grain Size Evaluation

Efforts were made to determine the grain size of the tested materials from their optical micrographs. The ASTM grain number (G) as well as the grain size (diameter D) were determined using the 'mean lineal intercept method,' prescribed by the ASTM

Designation E 112-1996 [53]. The following steps were used to determine the G and D values.

- First, a template (Figure 3-16) consisting of three concentric circles with a total length of 500 mm was placed over the resultant optical micrograph, and the total number of grain boundary intersections with these test lines was determined.

- Then, the mean lineal intercept length ($\bar{L}_L$) was determined by using Equation 3-24.

$$\bar{L}_L = \frac{L_T}{PM} \qquad \text{Equation 3-24}$$

where

L_T = Total length of test lines

P = Total number of grain boundary intersections

M = Magnification of the micrograph

- Next, the value of G was calculated using Equation 3-25.

$$G = -3.2877 - 6.438 \log \bar{L}_L \qquad \text{Equation 3-25}$$

- Finally, the grain diameter (D) was determined using Equations 3-26 and 3-27, shown below.

$$N = 2^{G-1} \qquad \text{Equation 3-26}$$

$$D = \frac{1}{\sqrt{N}} \qquad \text{Equation 3-27}$$

where

N = Number of grains/sq. mm at a magnification of 1X

D = Grain diameter, mm

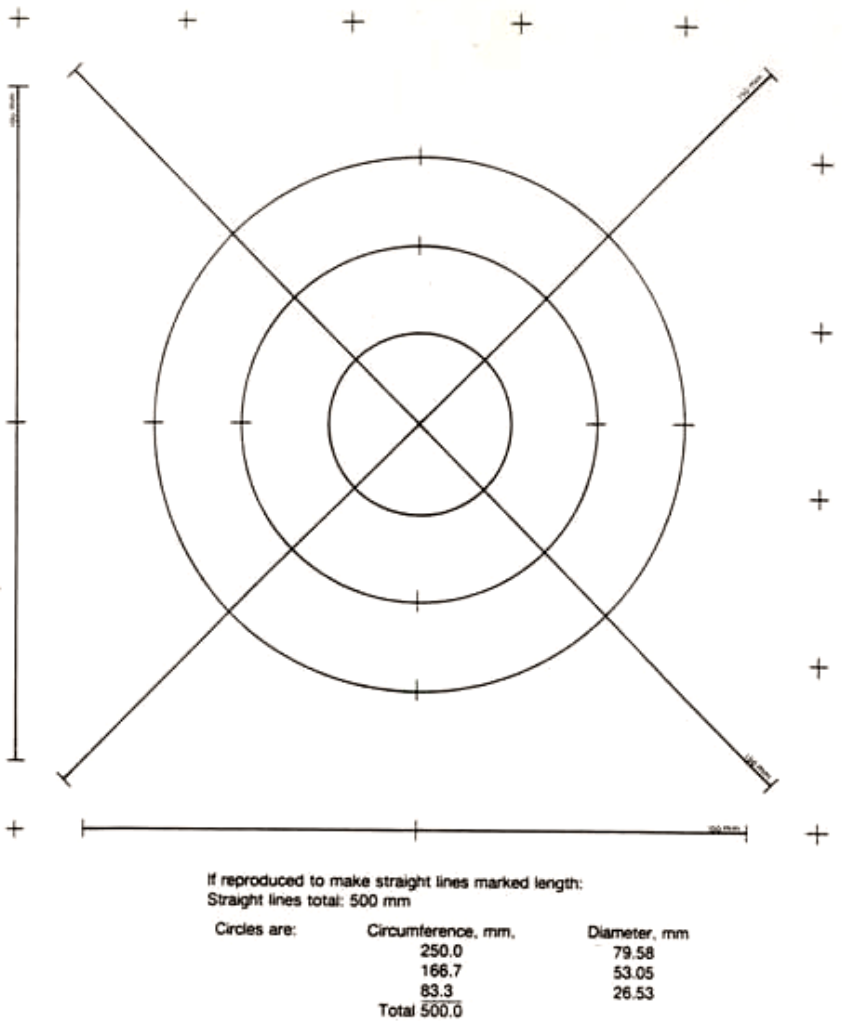

Figure 3-16 Template used in Grain Size Determination

3.6 Fractographic Evaluations

The extent and morphology of failure of the tested specimens were determined by a scanning electron microscope (SEM). Analysis of failure in metals and alloys involves identification of the type of failure. The test specimens were sectioned into 1/2 to 3/4 of an inch in length to accommodate them in the vacuum chamber of the SEM. Failures can usually be classified into two common types including ductile and brittle. Dimpled

microstructure is a characteristic of ductile failure. Brittle failure can be of two types; intergranular and transgranular. An intergranular brittle failure is characterized by crack propagation along the grain boundaries while a transgranular failure is characterized by crack propagation across the grains.

In SEM evaluations, electrons from a metal filament are collected and focused, just like light waves, into a narrow beam. The beam scans across the subject, synchronized with a spot on a computer screen. Electrons scattered from the subject are detected and can create a current, the strength of which makes the spot on the computer brighter or darker. This current can create a photograph-like image with an exceptional depth of field. Magnifications of several thousands are possible to achieve. A JEOL-5610 scanning electron microscope, shown in Figure 3-17, capable of resolution of up to 50 nm at magnifications of up to 100,000 times, was used in this study. The manual stage of this SEM unit can accommodate four 1 cm diameter samples or one sample with up to 3.2 cm diameter.

Figure 3-17 Scanning Electron Microscope

3.7 Transmission Electron Microscopy

TEM studies were conducted to characterize dislocations and precipitates of the tested creep specimens using a Tecnai G² F30 S-TWIN transmission electron microscope (Figure 3-18). This equipment operates at 300kV acceleration voltage that allows a point-to-point resolution of 0.2 nanometer. Magnifications up to 1,000,000 times can be achieved with this TEM. This system is fully loaded including HAADF (high angle annular dark field) detector, EDX (energy dispersive x-ray analysis), and GIF (Gatan Image Filter). Multiple samples were prepared from the tested specimen to obtain valid TEM micrographs. The sample preparation technique is described in details in the next subsection.

Figure 3-18 Transmission Electron Microscope

3.7.1 TEM Sample Preparation

Sample preparation for the TEM study involves a state-of-art technique. To ensure electron transparency of the sample by the TEM method, the specimen thickness was maintained between 50-100 nanometers. This was achieved through a series of operations, as described below [54, 55].

- Initially, multiple circular disc-shaped samples were cut from the gage length of the tested creep specimens up to a thickness of 500–700µm, using a precision cutter in the Materials Performance Laboratory (MPL).
- Samples were then mechanically ground (Figure 3-19) to about 100–150 µm using a grinder in the TEM Sample Preparation Laboratory. This process involved two steps; rough-grinding and fine-polishing. Specimen thickness was monitored periodically during this process.
- The samples were then punched into 3mm diameter discs, using a disc puncher (Figure 3-20).
- Finally, electro-polishing was done to achieve the desired specimen thickness. A twin-jet TenuPol-5 electro polisher (Figure 3-21) was used for this purpose. This process involved removal of material from the sample surface as well as surface finish prior to TEM observation. The thinnest area was obtained around the perforation area. The composition of the electrolyte used for the process was 5% perchloric acid ($HClO_4$) in methanol (CH_3OH) with an applied potential of 50V, a pump flow rate of 12 and a temperature of -3°C [56]. Care was taken to control the flow of electrolyte to prevent the formation of anodic film that could cause etching of the specimen rather than polishing [55, 57].

Figure 3-19 Grinding Accessories

Figure 3-20 Disc Puncher

Figure 3-21 TenuPol-5 Electro-polisher

CHAPTER 4

RESULTS

This chapter presents the overall data generated from different types of experimental work performed on Alloy 276. These data include the results of microstructural evaluation, crack-growth studies under both variable and constant load ratios (R), fracture toughness (J_{IC}) evaluation, stress-corrosion-cracking (SCC) evaluation in terms of stress-intensity-factor (K_{SCC}) under wedge-loaded conditions for variable exposure periods, characterization of time-dependent plastic deformation under sustained loading (creep) at different temperatures, characterization of defects (dislocations and voids) and precipitates by TEM, and finally, analyses of fracture morphology by SEM. These results are presented next in different sub-sections in a systematic manner.

4.1 Metallographic Evaluation

An optical micrograph of an as-received Alloy 276 specimen, polished and etched in a mixture of HCl, HNO_3 and $CuCl_2$, is illustrated in Figure 4-1. Large austenitic grains and annealing twins, characteristics of solution-annealed Ni-base alloys, are clearly present in this micrograph. The average grain diameter of this alloy, determined by the mean lineal intercept method [53, 58], was found to be 0.101 mm that corresponds to an ASTM grain size of 4 [59].

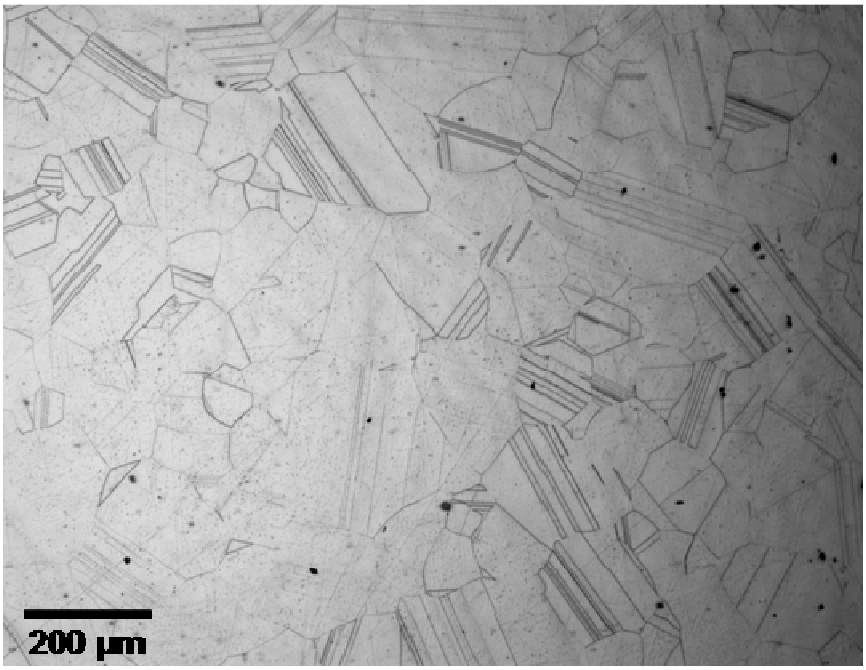

Figure 4-1 Optical Micrograph of Alloy 276 ($HCl + HNO_3 + CuCl_2$)

4.2 Crack-Growth-Rate Evaluation

4.2.1 Crack-Growth-Rate versus Stress Intensity Range

Prior to the evaluation of crack-growth-rate (CGR) of Alloy 276 in terms of da/dN, the tensile properties of this alloy including the yield strength (YS), ultimate tensile strength (UTS), percent elongation (%El), percent reduction in area (%RA), and modulus of elasticity (E) were determined at ambient temperature, 100, 150, 200, 300 and 500 °C using smooth cylindrical specimens according to the ASTM Designation E 8-2004 [60]. The magnitudes of these properties are given in Table 4-1. The tensile data indicate that the magnitudes of YS, UTS and E were gradually reduced with increasing temperature due to ease of deformation at elevated temperatures.

Table 4-1 Results of Tensile Testing

Temperature (°C)	YS, MPa	UTS, MPa	%El	%RA	E, GPa
Ambient	354	794	87	78	260
100	308	724	85	77	245
150	290	709	84	76	230
200	272	694	84	76	229
300	261	682	85	73	220
500	223	638	84	70	203

The superimposed da/dN versus ΔK plots for this alloy, generated under R values of 0.1, 0.2, and 0.3 within a temperature range of ambient to 300 °C, are shown in Figures 4-2, 4-3, and 4-4. It is obvious from these figures that irrespective of the R value, the CGR in terms of da/dN was appreciably higher at 150 °C, compared to that at ambient temperature. At 300 °C, the magnitude of da/dN was also slightly enhanced, suggesting that the CGR was further increased at a higher temperature.

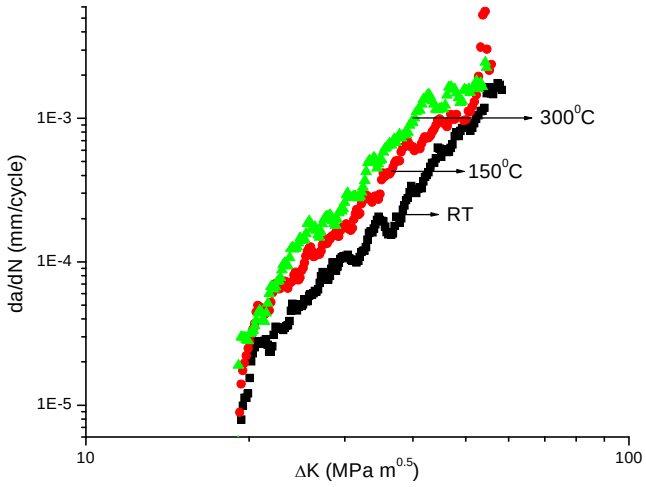

Figure 4-2 da/dN vs. ΔK at R = 0.1

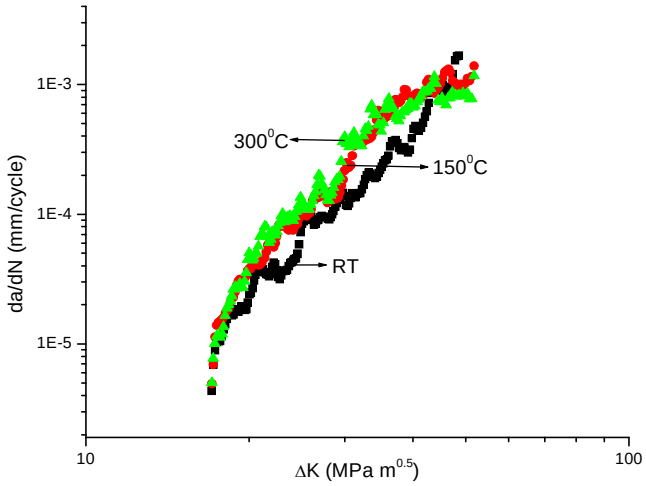

Figure 4-3 da/dN vs. ΔK at R = 0.2

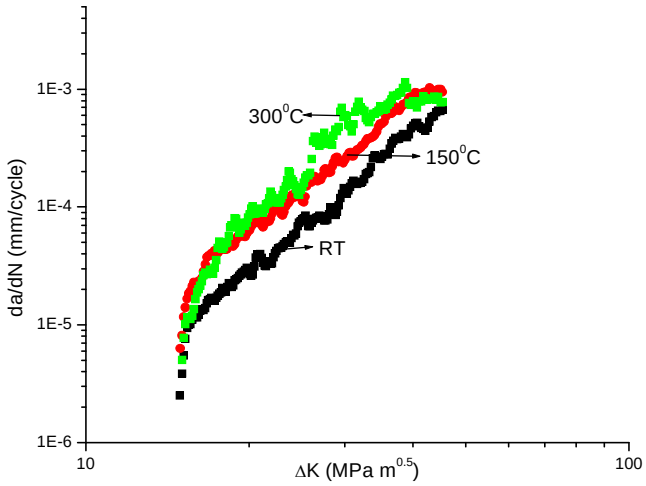

Figure 4-4 da/dN vs. ΔK at R = 0.3

4.2.2 Crack Length versus Number of Cycles

The superimposed plots of crack length (a) versus number of cycles (N), generated under an R value of 0.1 in the temperature range of ambient to 300 °C, are shown in Figure 4-5. These data indicate that the number of cycles (N) needed for comparable

crack extension was significantly reduced with increasing temperature. Thus, the magnitude of da/dN was higher at elevated temperatures when the R value was maintained at 0.1. It should, however, be noted that the difference in N value at temperatures between 150 and 300 ^{o}C was not that significant. A similar trend in 'a' versus 'N' plot was observed with this alloy at R values of 0.2 and 0.3, as illustrated in Figures 4-6 and 4-7, respectively. Variations of 'a' with 'N' at room temperature, 150 and 300 °C, at three R values, are shown in Figures 4-8, 4-9 and 4-10, respectively. These data indicate that the magnitude of N needed to develop a comparable crack length reached a minimum value at an R value of 0.1, irrespective of the testing temperature. However, even at this R value (0.1), the lowest value of N to cause a similar level of cracking resulted at 300 °C, suggesting a combined detrimental effect of both higher temperature and lower load ratio on the cracking tendency of Alloy 276. A lowest value of N at an R value of 0.1 could be attributed to a maximum loading constraint resulting from the highest load range (ΔP) of 4.5 kN.

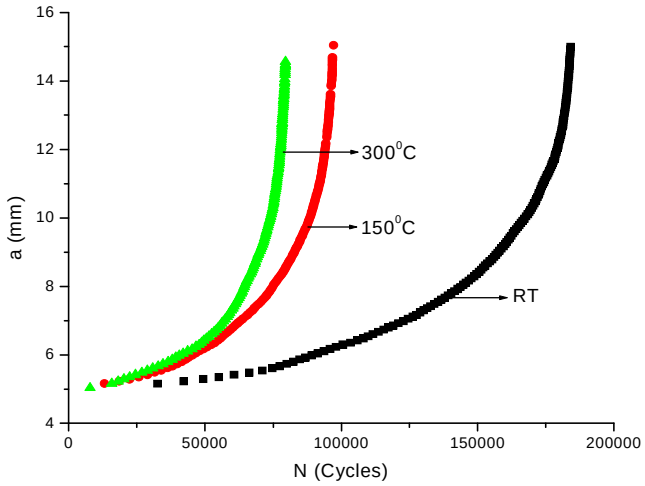

Figure 4-5 Crack Length (a) vs. N at R = 0.1

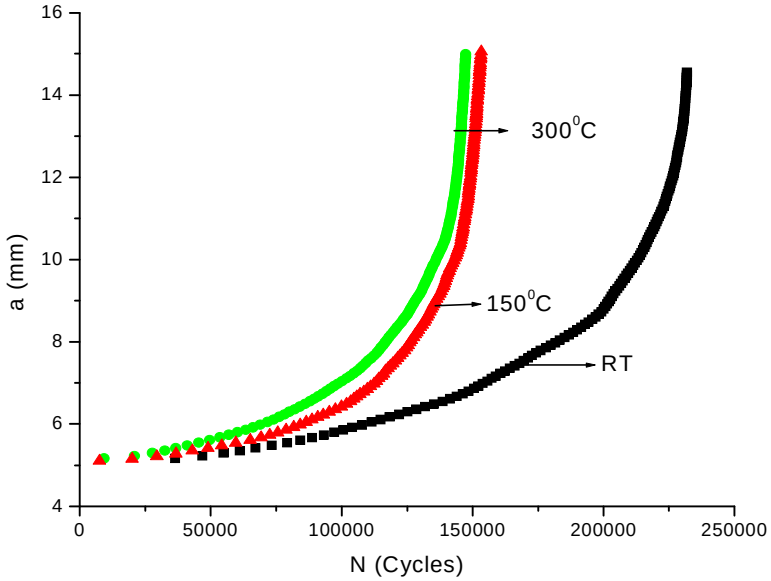

Figure 4-6 Crack Length (a) vs. N at R = 0.2

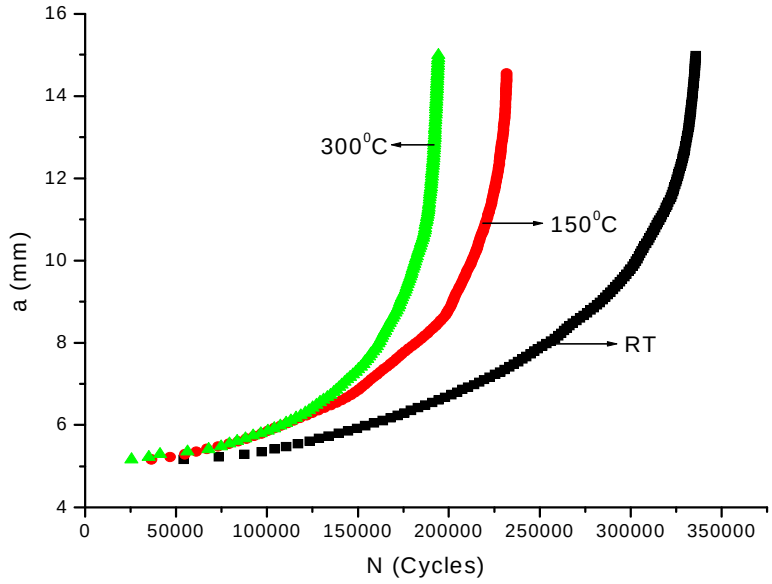

Figure 4-7 Crack Length (a) vs. N at R = 0.3

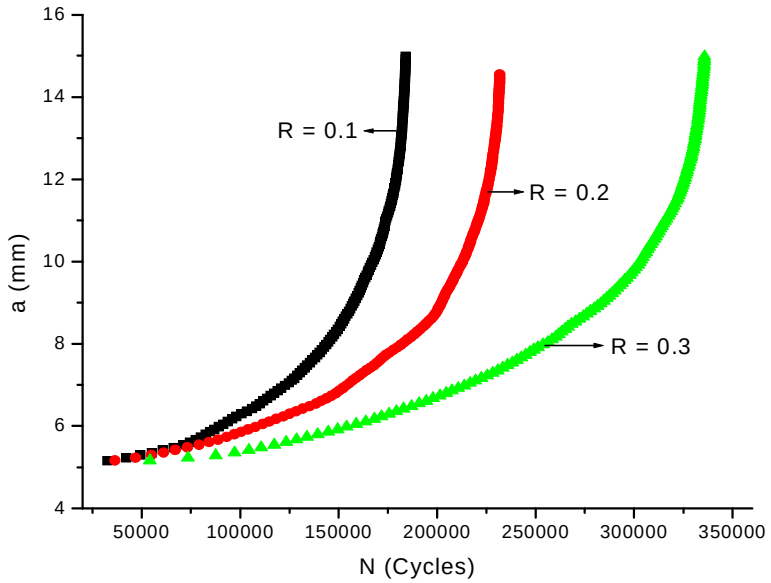

Figure 4-8 Crack Length (a) vs. N at Room Temperature

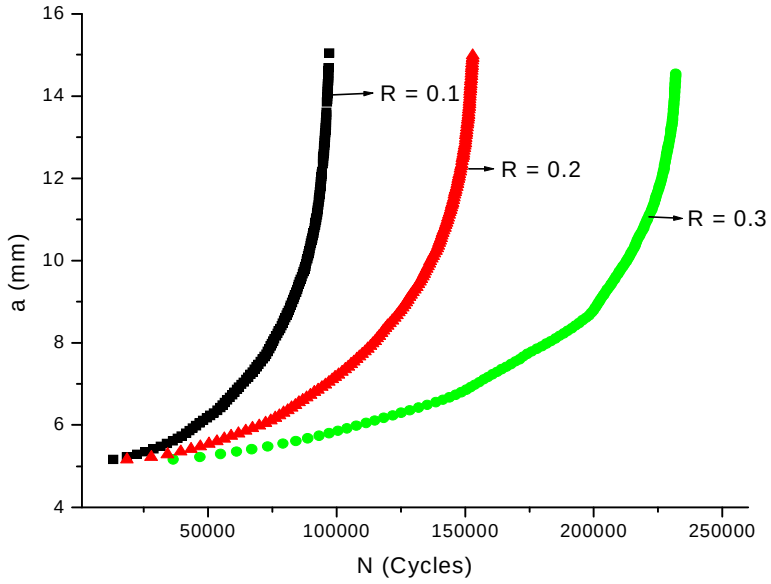

Figure 4-9 Crack Length (a) vs. N at 150 °C

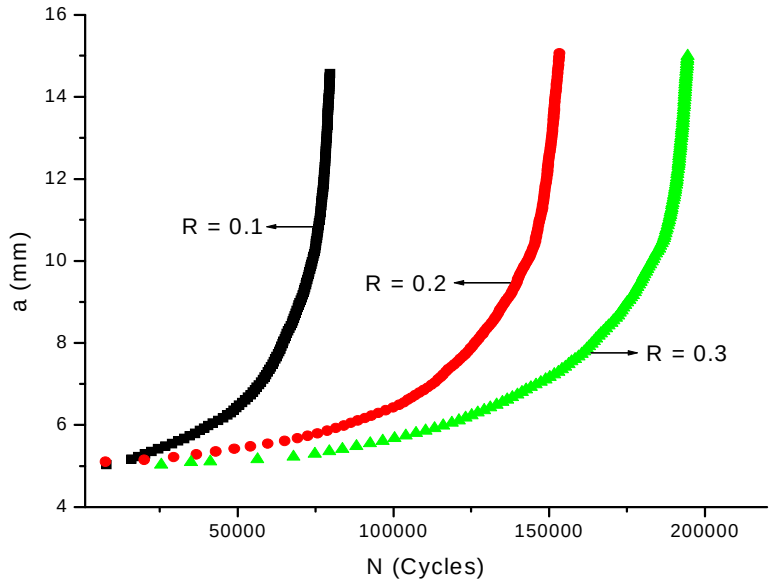

Figure 4-10 Crack Length (a) vs. N at 300 °C

4.2.3 N versus Temperature and R

The variation of N with temperature as a function of R (0.1, 0.2 and 0.3) is illustrated in Figure 4-11. Once again, these data indicate that the number of cycles needed for comparable crack extension was significantly reduced at 150 °C compared to that at room temperature, irrespective of the R value. Interestingly, the magnitude of N was not significantly reduced at a higher temperature (300 °C), suggesting that the crack might have reached a critical length within a temperature range of 150-300 ^{o}C. The variation of N with R at different temperatures is illustrated in Figure 4-12, once again confirming the detrimental effect of the lowest R value and higher temperature in enhancing the cracking susceptibility of Alloy 276 in terms of reduced number of cycles.

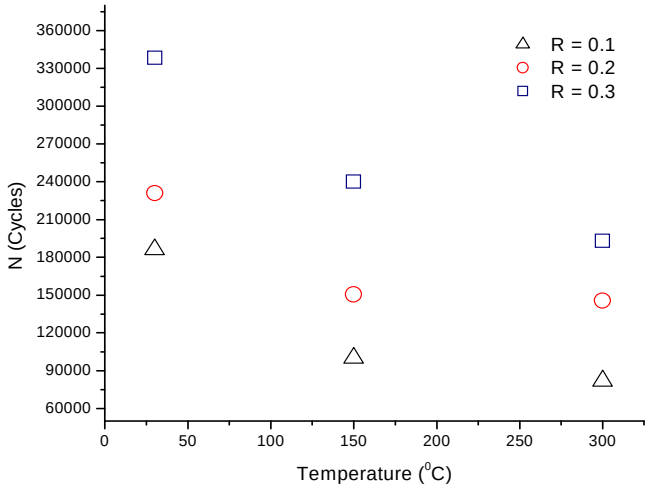

Figure 4-11 N vs. Temperature

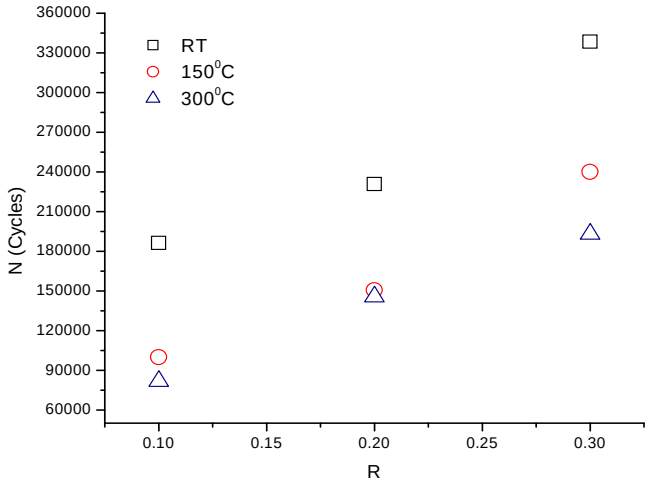

Figure 4-12 N vs. R

4.2.4 Number of Cycles to Failure versus Temperature and R

Efforts were made to calculate the number of cycles to failure (N_f) at different temperatures at all three tested R values. The magnitude of N_f was calculated using Equation 3-3, derived from the Paris equation. The variations of N_f with temperature and

R are illustrated in Figures 4-13 and 4-14, respectively. These data, once again, confirm the detrimental effects of higher temperature and lower R value on crack extension of Alloy 276 by showing reduced N_f values.

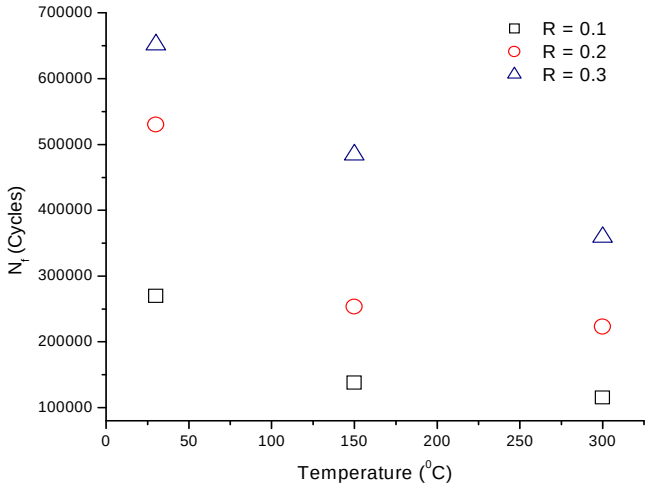

Figure 4-13 N_f vs. Temperature

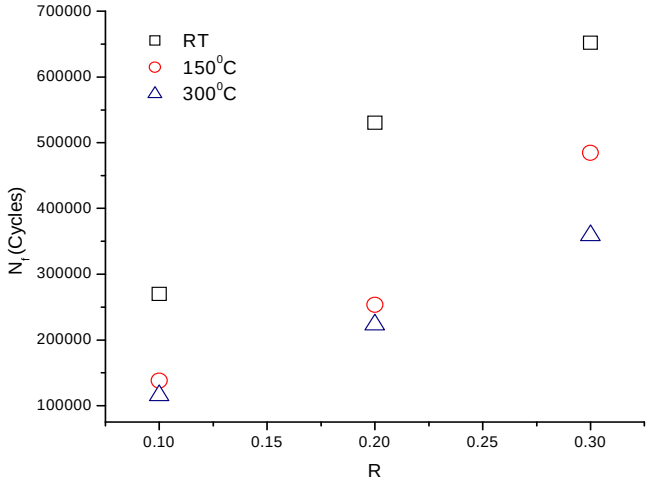

Figure 4-14 N_f vs. R

4.2.5 Determination of Slope and Crack-Growth Coefficient

The magnitudes of the slope (m) and crack-growth coefficient or intercept (A) of the linear portion of the da/dN versus ΔK plot (using Paris Equation) at different temperatures and R values are given in Tables 4-2 and 4-3, respectively. These data suggest that, irrespective of the testing temperature and R value, there were no significant variations in m value (i.e., 3.72-4.0), suggesting that the steady-state regions at all temperatures and R values maintained the same slope, even though the CGR was different. However, the magnitude of 'A' was gradually increased with an increase in temperature from ambient to 300 °C at all three R values. Also, the magnitude of A was gradually reduced at higher R values when the temperature was kept constant.

Table 4-2 Calculated m Values from da/dN vs. ΔK Plots

Temperature (°C)	m		
	R = 0.1	R = 0.2	R = 0.3
Room Temperature	4	3.82	3.88
150	3.97	3.83	3.72
300	3.92	3.80	3.82

Table 4-3 Calculated A Values from da/dN vs. ΔK Plots

Temperature (°C)	A ($\times 10^{-13}$ MPa$\sqrt{m}$)		
	R = 0.1	R = 0.2	R = 0.3
Room Temperature	1.22	1.15	1.05
150	2.99	2.89	2.75
300	3.70	3.60	3.50

4.2.6 Determination of Threshold Stress Intensity Ranges

The variations of threshold stress intensity range (ΔK_{th}) with temperature at three different R values are given in Table 4-4. As expected, these data indicate insignificant variation of ΔK_{th} value with temperature when the R value was kept constant. However, the magnitude of ΔK_{th} was gradually reduced with increasing R value irrespective of the testing temperature, as anticipated. Such results can be justified in terms of relatively higher loading constraint due to a greater load range (ΔP) at lower R values, thus causing higher cracking tendency. Thus, the role of R on da/dN becomes very significant.

Table 4-4 Average ΔK_{th} Values

Temperature (°C)	ΔK_{th} (MPa$\sqrt{m}$)		
	R = 0.1	R = 0.2	R = 0.3
Room Temperature	18.90	16.77	14.51
150	18.76	16.89	14.58
300	19.00	16.90	14.78

4.2.7 Determination of Activation Energy

The calculated values of activation energy (Q) for crack propagation of Alloy 276 within a temperature range of ambient to 300 °C at all three tested R values are given in Table 4-5. The average Q value was found to be approximately 308 J/mole. While no literature data exist as to the Q value of this alloy, the average Q value estimated in this study seems to be close to that of a similar type of alloy, DS-GTD-111 [33]. It is interesting to note that the Q value was somewhat enhanced with an increase in the load

ratio (R), suggesting that greater driving forces were necessary for crack extension at higher R values due to lesser loading constraint. Plots of ln (A) versus 1/T are shown in Figures 4-15 through 4-17 at R values of 0.1, 0.2, and 0.3, respectively, from which the Q values were calculated using their slopes.

Table 4-5 Calculated Q Values vs. R

R	Average Q (J/mole) at a particular R Value	Average Q (J/mole)
0.1	296.8	307.7
0.2	305.2	
0.3	321.0	

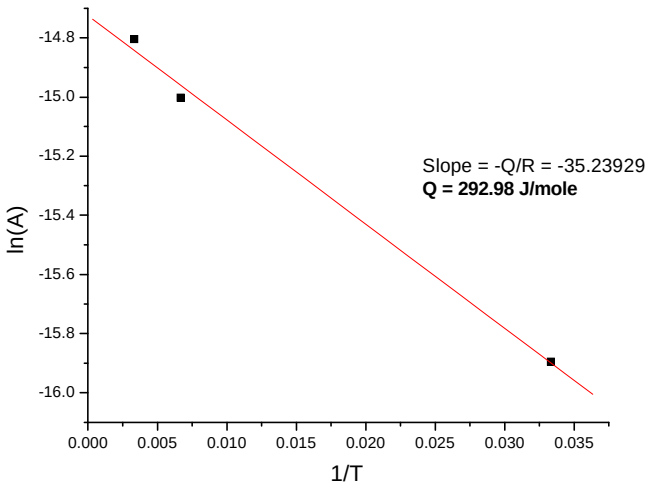

Figure 4-15 ln (A) vs. 1/T at R = 0.1

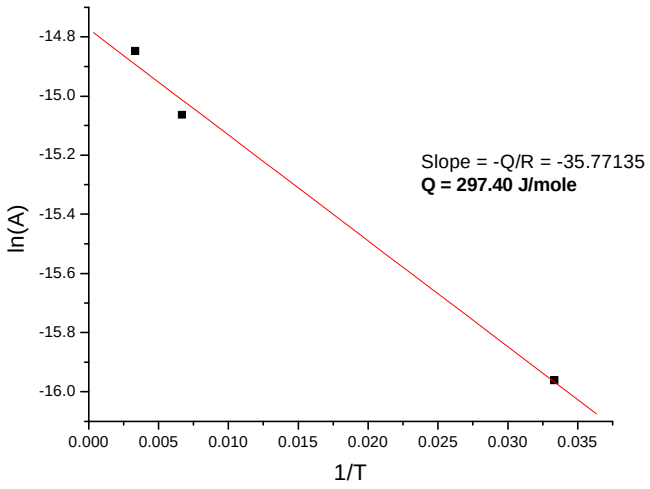

Figure 4-16 ln (A) vs. 1/T at R = 0.2

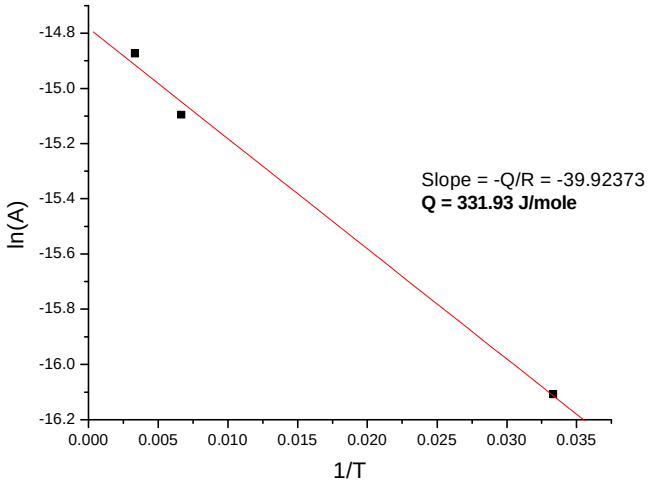

Figure 4-17 ln (A) vs. 1/T at R = 0.3

4.2.8 Results of Constant-K Testing

The results of CGR testing performed at different ΔK values under an R value of 0.1 at ambient temperature are illustrated in Figure 4-18 in the form of crack-length (a) vs. number of cycles (N) plots. These data reveal a linear relationship for all three ΔK values,

consistent with the literature [61, 62]. The slopes of these linear plots (da/dN) were calculated and are shown in Table 4-6 against the corresponding ΔK values. The variation of the number of cycles (N) with the ΔK values for comparable crack growth (15 mm) is also shown in Table 4-6. These data indicate that even though there was a reduction in the N values with increasing ΔK, there was insignificant variation in the da/dN values for all three ΔK values. This observation suggests that the CGR of Alloy 276 was independent of the K values. The plots of 'a' vs. load (P) are also shown in Figure 4-19. The P value was gradually decreased with increasing 'a' for all three sets of K values. This is due to the fact that in a constant-K test, the only variables are 'a' and P. So if 'a' increases, P decreases [$K = \sigma\sqrt{(\pi a)}\times\alpha$, where σ = stress = P/area, and α = geometric factor (constant)].

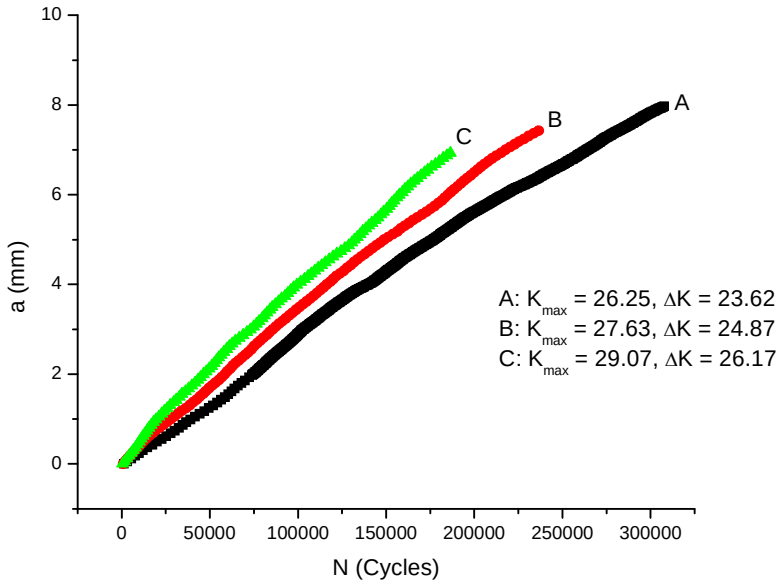

Figure 4-18 Crack Length (a) vs. N

Table 4-6 da/dN and N Values vs. ΔK

ΔK (MPa√m)	Average da/dN (mm/cycle) ×10^{-5}	N (Cycles)
23.62	2.85	445809
24.87	2.77	440651
26.17	3.90	330365

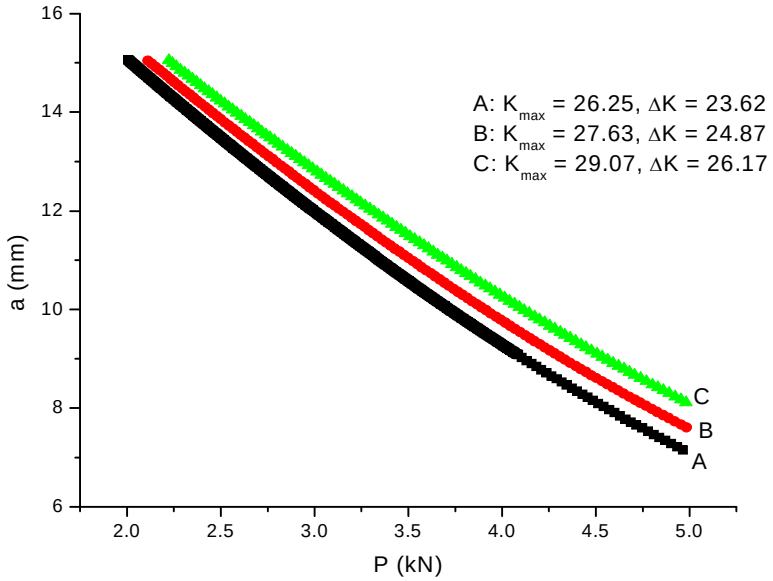

Figure 4-19 a vs. P

4.3 Results of Fracture Toughness Testing

4.3.1 Determination of J_{IC}

The measured conditional fracture toughness (J_Q) values determined from J_{IC} testing satisfied the validity criteria set by the ASTM Designation E 813-1989. The average J_{IC} values of Alloy 276 tested at room temperature, 100, 200 and 500 °C are given in Table 4-7. Also, the variation of J_{IC} with temperature is illustrated in Figure 4-20. These data indicate that the J_{IC} value was gradually reduced with increasing temperature, the

reduction being more pronounced as the temperature was increased from ambient to 100 °C. The reduction in the J_{IC} value is due to the fact that at higher temperatures, plastic deformation is enhanced thereby increasing the cracking susceptibility of the material. As a result, the resistance to fracture decreases resulting in a lower J_{IC} value, as obtained at 100 °C. Between 200 and 500 °C, an insignificant change in J_{IC} value was observed. A load versus load-line-displacement (LLD) plot and a J-Integral versus Δa plot used in J_{IC} calculation are illustrated in Figures 4-21 and 4-22, respectively.

Table 4-7 J_{IC} vs. Temperature

Temperature (°C)	Average J_{IC} (KJ/m^2)
Room Temperature	155.7
100	102.9
200	88.1
500	86.2

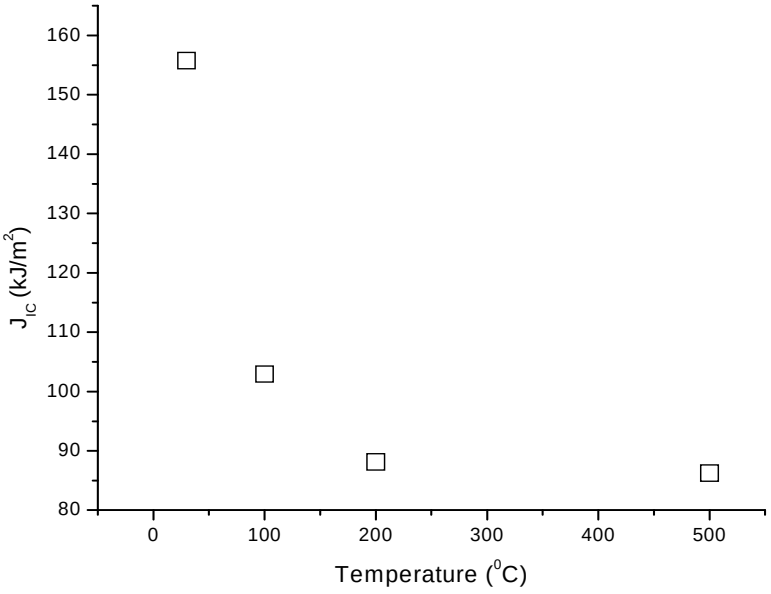

Figure 4-20 J_{IC} vs. Temperature

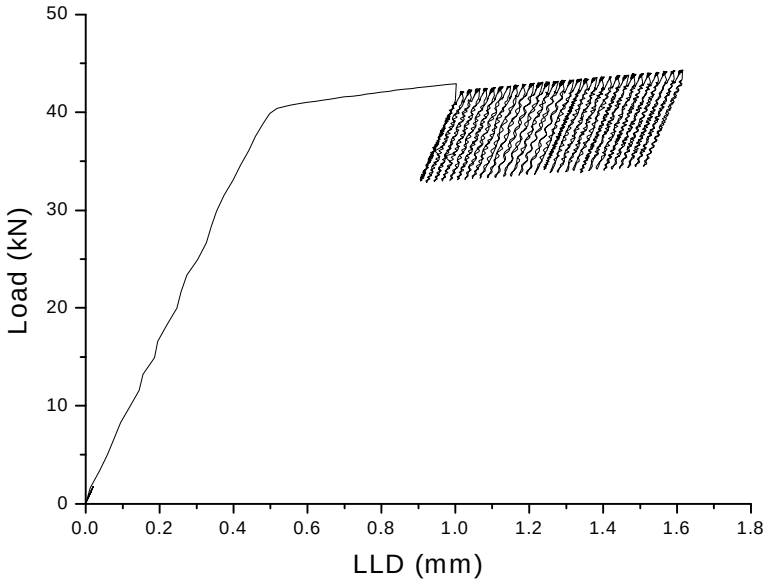

Figure 4-21 Load vs. LLD at Ambient Temperature

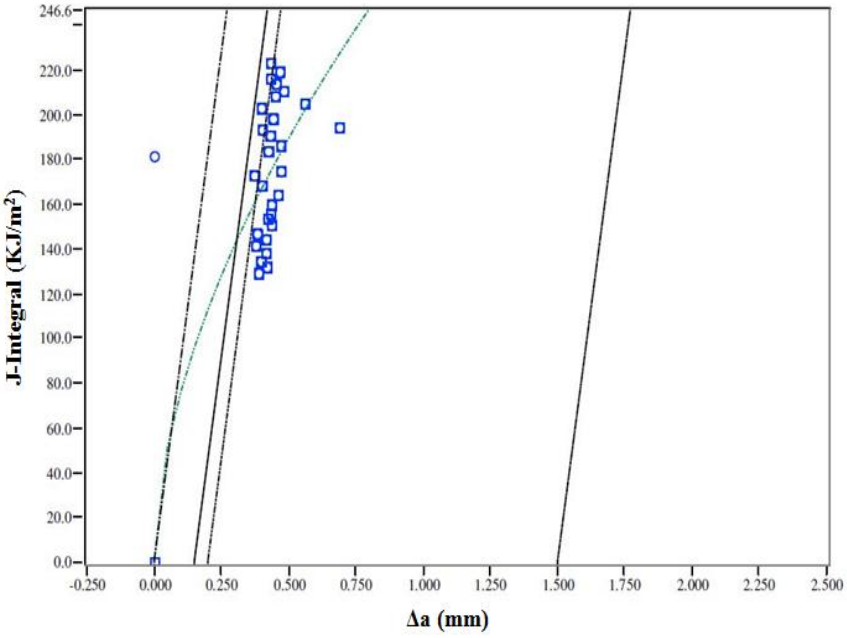

Figure 4-22 J-Integral vs. Δa at Ambient Temperature

4.3.2 Equivalent K_{IC} and CTOD Values

The average values of equivalent K_{IC} (determined by using Equation 3-14) and CTOD (determined by using Equation 3-15) are given in Table 4-8. Since no fracture toughness data exist in the open literature for Alloy 276, neither the J_{IC} nor the K_{IC} values determined from this investigation could be compared for verification purpose. However, it should be noted that the measured fracture toughness values of Alloy 276, in terms of J_{IC}/K_{IC}, were substantially higher compared to those of other engineering materials, as shown in Table 4-9 [8]. Further, the calculated δ values were very close to a range of CTOD values (0.1 to 0.2) for an adequately tough material [63].

Table 4-8 K_{IC} and δ Values vs. Temperature

Temperature (°C)	Average K_{IC} (MPa√m)	Average δ (mm)
Room Temperature	192.1	0.24
100	155.9	0.18
200	143.3	0.18
500	138.6	0.21

Table 4-9 Fracture Toughness Values of Different Engineering Materials

Material	Fracture Toughness (K_{IC}), MPa√m (Ambient Temperature)
Alloy 276	**192**
Alloy 617	163
Alloy 230	137
Titanium-6Al-4V	115
4340 Steel	99
304 Stainless Steel	88
Maraging Steel 350	55
Aluminum 7075	24

4.3.3 Tearing Modulus Values

The average tearing modulus (T) values for Alloy 276 are given in Table 4-10 as a function of temperature. These results indicate that the T value of this alloy was gradually enhanced with increasing temperature. Greater T values with Alloy 276 indicate its greater resistance to tearing due to increased plasticity at elevated temperatures, thus less susceptibility to brittle cracking [42]. The magnitudes of dJ/da, used in the calculation of T, were determined from the plot of J versus crack extension (Δa), as shown in Figure 4-23.

Table 4-10 Tearing Modulus (T) vs. Temperature

Temperature (°C)	Average T (Dimensionless)
Room Temperature	377.8
100	478.6
200	544.3
500	557.3

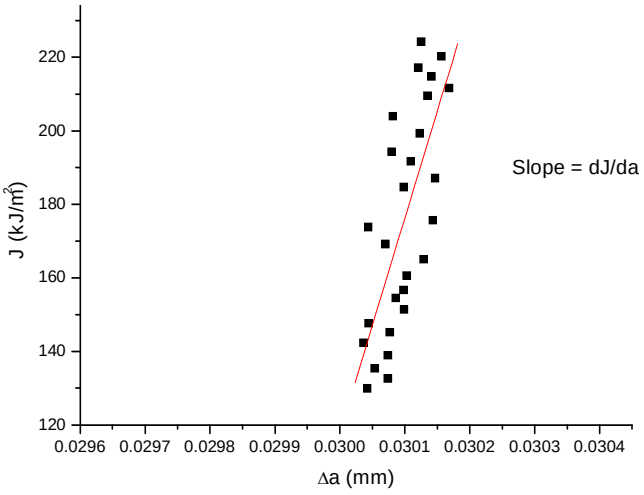

Figure 4-23 J vs. Crack Extension (Δa) at Room Temperature

4.4 Results of SCC Testing

The results of SCC testing using DCB specimens of Alloy 276, immersed in an acidic solution (pH ~ 1) at 100 °C for 1, 2, 4 and 8 months, are given in Table 4-11. The final crack lengths due to SCC were determined from the SEM micrographs of the broken surfaces of the tested specimens, loaded under different initial stress intensity factor (K_I) values. SEM micrographs of three different regions of a broken surface of a tested DCB specimen, loaded for four months at a K_I value of 45.34 MPa$\sqrt{m}$, are illustrated in Figure 4-24. These micrographs revealed striations due to cyclic loading during pre-cracking, brittle (cleavage) failure resulting from SCC, and dimpled microstructure indicating ductile failure resulting from fast fracture under tensile loading. The final wedge-loads sustained by the specimens upon completion of testing were found to be substantially reduced from the initial applied loads, the reduction being more pronounced for specimens loaded at higher K_I values. The difference in stress intensity (ΔK) value and the crack-growth-rate were also enhanced for specimens loaded at higher K_I levels.

The variation of crack extension with test duration is illustrated in Figure 4-25, showing greater crack extension under higher K_I values. The average crack-growth-rate (CGR) was also plotted against the test duration, as shown in Figure 4-26. These data indicate that the average CGR was gradually reduced with increasing exposure time, possibly reaching a near-threshold value at the eighth month. The DCB testing is based on a constant-displacement method, whereby the load imparted by the wedge gradually drops as crack extends, thus resulting in reduced stress intensity factor (K_f) values due to exposure in a corrosive environment for selected times. The wedge-load becomes so insignificant following exposure for a critical time-period that the stress corrosion crack

can not extend any further, thus achieving a threshold K value, known as $K_{ISCC.}$ Thus, the resultant data suggest that a K_{ISCC} value for Alloy 276 can be reached if SCC testing could be performed for a little longer duration (more than eight months) in a similar environment involving wedge-loaded DCB specimens.

Table 4-11 Results of DCB Testing

Test Duration (Months)	P_i	P_f	ΔP	a_i	a_f	Δa	K_I	K_f	ΔK	CGR
1	2748	2401	347	33.4	34.4	0.9412	39.53	35.31	4.22	1.31E-03
1	2351	2134	217	33.1	33.7	0.569	33.56	30.88	2.68	7.9E-04
2	2821	2290	531	32.7	33.8	1.095	39.89	33.23	6.80	7.6E-04
2	2226	1723	503	33.2	33.8	0.671	31.82	25.02	6.65	4.66E-04
4	3140	2450	690	33.6	34.8	1.162	45.34	36.35	8.99	4.03E-04
4	2402	1872	530	32.7	33.7	0.951	33.97	27.08	6.89	3.3E-04
8	3200	2213	987	32.6	34.2	1.576	45.14	32.40	12.73	2.74E-04
8	1933	1357	576	35.7	36.9	1.219	29.28	21.12	8.16	2.12E-04

where

P_i = Initial load, N

P_f = Final load, N

ΔP = Reduction in load, N

a_i = Initial crack length, mm

a_f = Final crack length, mm

Δa = Crack extension, mm

K_I = Initial stress intensity factor, MPa$\sqrt{m}$

K_f = Final stress intensity factor after exposure, MPa$\sqrt{m}$

ΔK = Difference in stress intensity factor, MPa$\sqrt{m}$

CGR = Crack-growth-rate, mm/hr

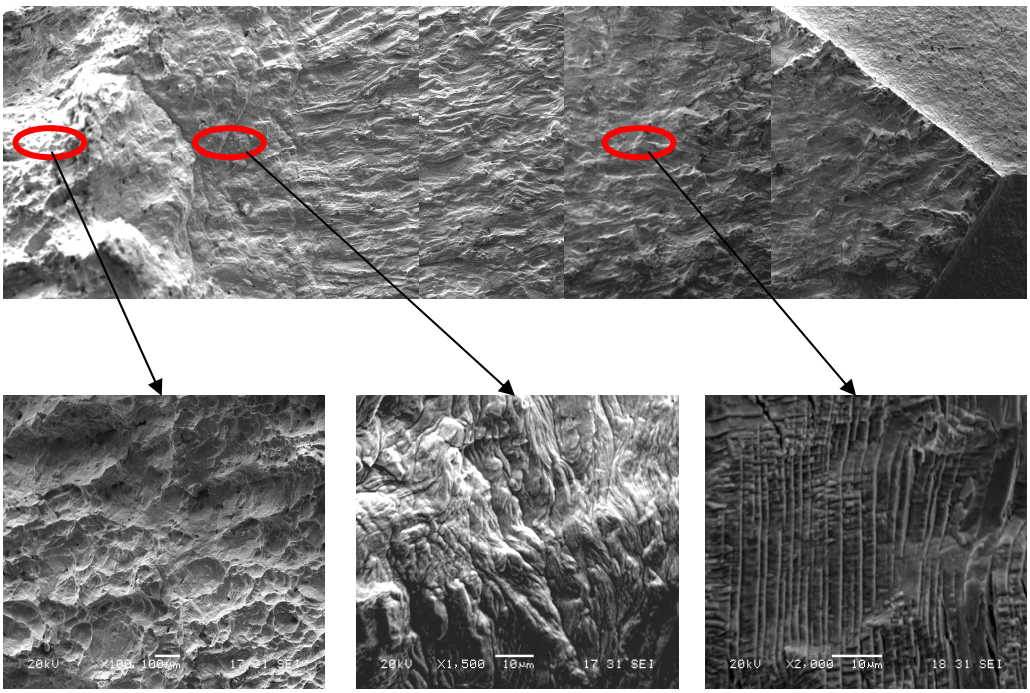

Figure 4-24 SEM Micrographs of a Broken DCB Specimen Surface

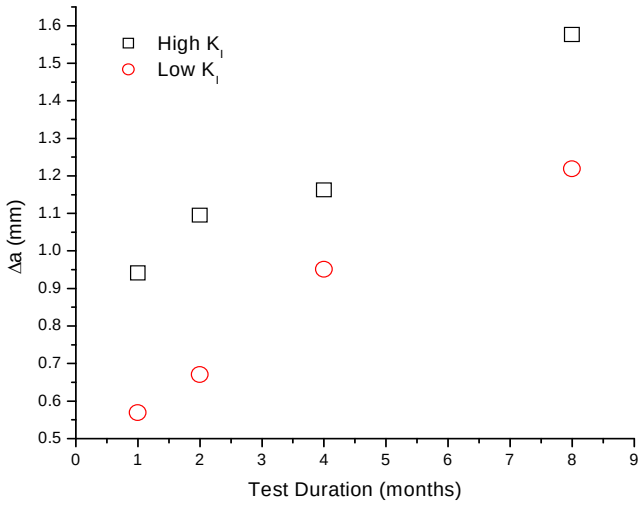

Figure 4-25 Crack Extension (Δa) vs. Test Duration

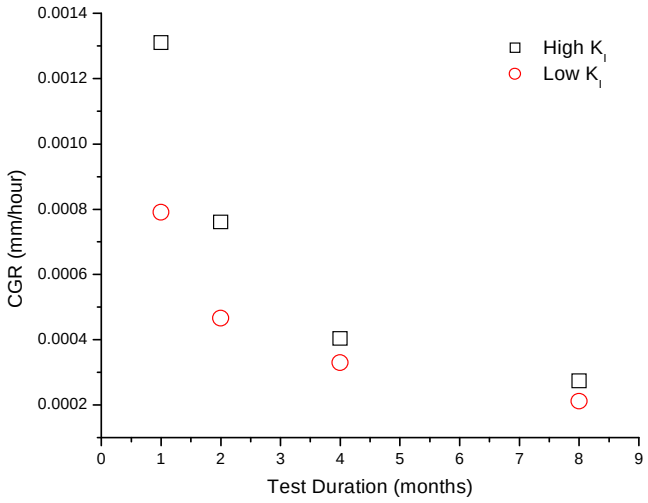

Figure 4-26 Average CGR vs. Test Duration

4.5 Results of Creep Testing

The results of creep testing, showing % creep versus time, involving specimens of Alloy 276 loaded to initial stresses equivalent to 10 and 25% of its yield strength (0.10YS and 0.25YS) values at temperatures of 750, 850 and 950 °C, are shown in Figures 4-27 and 4-28, respectively. These data indicate that when tested at 0.10YS, Alloy 276 did not exhibit any tertiary stage at all three tested temperatures following 1000 hours of testing, suggesting that this alloy may be resistant to failure by time-dependent deformation (creep) at these temperatures. It is, however, interesting to note that at 950 °C, a longer primary creep zone was observed compared to that at 750 and 850 °C. No tertiary zone was also observed when this alloy was tested at 0.25YS at 750 and 850 °C. However, at the same stress level at 950 °C, a very short steady-state creep curve was observed, followed by severe deformation in the tertiary region within 200 hours of testing. These

results suggest that Alloy 276 may not be able to sustain a temperature in the vicinity of 950 °C under an applied stress equivalent to its 0.25YS value.

Assuming that a structural material must not undergo creep deformation exceeding 1% strain following 1000 hours of loading at different stress levels [64], it could be stated that Alloy 276 can be safely used at operating temperatures of 750, 850 and 950 °C at applied stresses equivalent to 10% of its YS values and at 750 °C at 25% of its YS value. However, based on a similar criterion, this material is not capable of withstanding operating temperatures of 850 and 950 °C at applied stresses corresponding to its 0.25YS values. The variation of creep rate with total strain/creep observed in this study at 950 °C for the specimen loaded at 0.25YS is shown in Figure 4-29. As anticipated, the creep rate was gradually reduced until a steady state region was reached, followed by substantially higher creep rates in the tertiary region. Such variation in creep rate is consistent with the findings cited in the open literature [48].

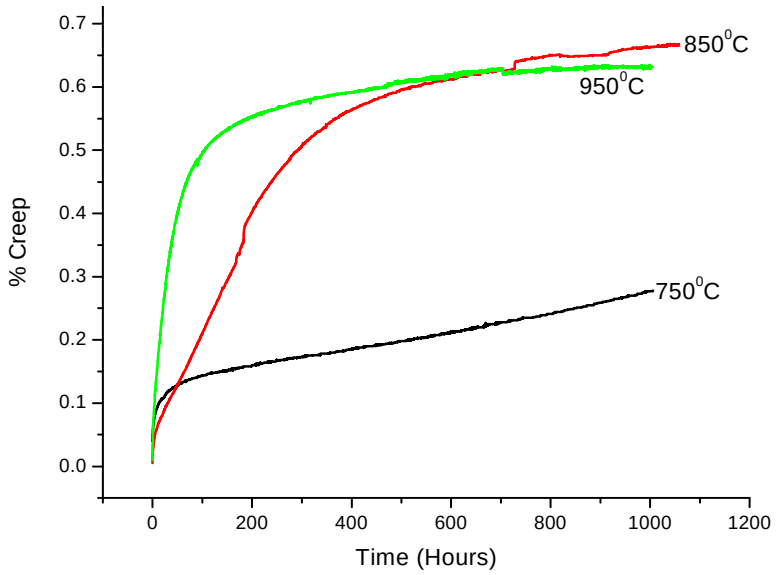

Figure 4-27 % Creep vs. Time at 0.10YS Values

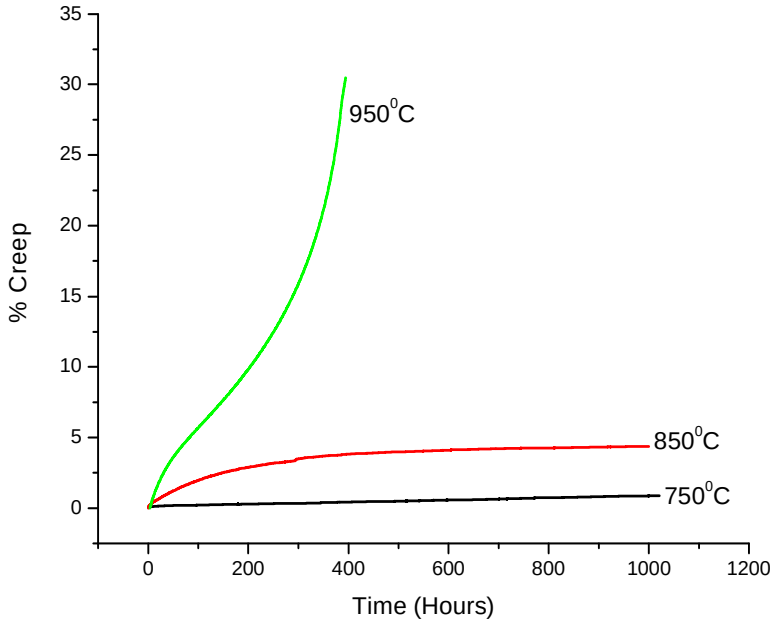

Figure 4-28 % Creep vs. Time at 0.25YS Values

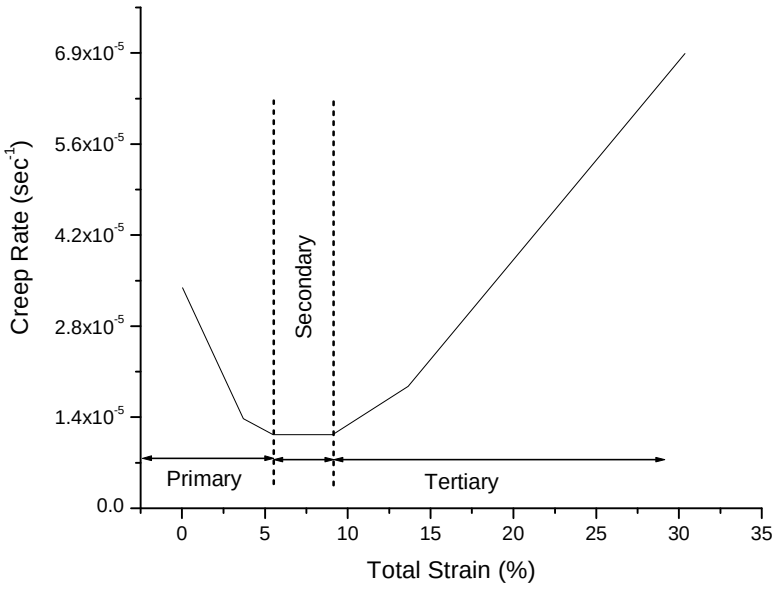

Figure 4-29 Creep Rate vs. Total Strain at 950 °C at 0.25YS

The variations of the steady-state creep rate ($\dot{\varepsilon}_s$) with temperature at both applied stress levels are illustrated in Figure 4-30. These data indicate that the magnitude of $\dot{\varepsilon}_s$ was increased with increasing temperature, when tested at applied stresses corresponding to 0.25YS, which is generally expected since creep is a thermally-activated phenomenon. However, when tested at 0.10YS, the magnitude of $\dot{\varepsilon}_s$ at 950 °C was somewhat lower than that at 850 °C. Further, the $\dot{\varepsilon}_s$ values were relatively higher for specimens tested at a higher stress level (0.25YS), as anticipated.

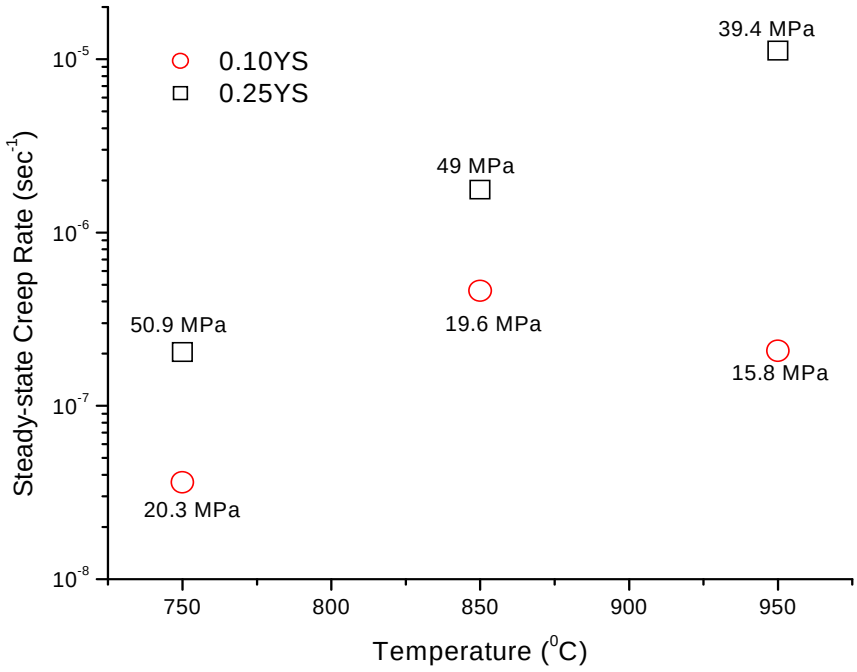

Figure 4-30 $\dot{\varepsilon}_s$ vs. Temperature

4.5.1 Activation Energy Results

As indicated earlier, efforts were made to estimate the magnitude of activation energy (Q) for creep deformation by three methods. The variation of ln ($\dot{\varepsilon}_s$) with (1/T) for the specimen tested at 0.25YS is shown in Figure 4-31. This plot was used to determine Q by the first method which involved an Arrhenius equation (Equation 3-19). The magnitudes of Q determined by all three methods are shown in Table 4-12. The Q values for creep deformation of Alloy 276 ranged between 242.98-300.31 kJ/mole and 205.15-208.37 kJ/mole at applied stresses of 0.10 and 0.25YS, respectively. A wide range of Q values for creep deformation of nickel-base alloys (86-1037 kJ/mole) has been reported in the literature [65-67]. It can be concluded that the calculated Q value for Alloy 276 falls in the range of those reported values.

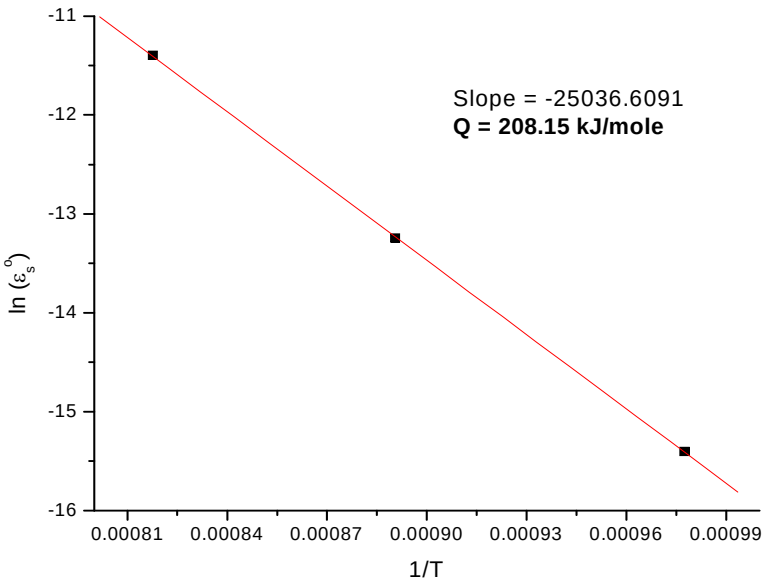

Figure 4-31 ln ($\dot{\varepsilon}_s$) vs. (1/T)

Table 4-12 Q Values

Method	Q (kJ/mole)	
	0.10YS	0.25YS
1	-	208.15
2	242.98	208.37
3	300.31	205.15

4.5.2 Results of TEM Study

TEM analysis was performed on the specimen tested for creep evaluation at 750 °C at an applied stress of 0.25YS to develop a mechanistic understanding of the deformation behavior. The TEM micrographs, as illustrated in Figures 4-32 (a-d), revealed dislocation pile ups, blocking of dislocation movement and precipitates of different sizes within the matrix. Energy dispersive x-ray (EDX) analysis was performed using the scanning transmission electron microscopic (STEM) mode of TEM to identify the precipitates. This analysis is illustrated in Figure 4-33a. EDX analysis of the base matrix is also shown in Figure 4-33b for comparison purposes, which revealed the presence of Nickel (Ni), Chromium (Cr) and Molybdenum (Mo). As evident in Figure 4-33a, the precipitates were rich in Mo and Tungsten (W) along with Carbon (C). Literature suggests [68-70] that three types of precipitate phases can appear in Alloy 276 when exposed to temperatures above 650 °C. These are namely carbides of type M_6C, μ-phase and P-phase. Of these three, μ-phase usually forms in the temperature regime of 760-1093 °C and the occurrence of P-phase is very rare. M_6C precipitates can appear at any temperature

between 650 and 1038 °C and these precipitates usually occur if the weight percent of Mo or W is greater than six. Based on these literature studies and EDX analysis, it can be inferred that in the current investigation the precipitates are of the type M_6C carbides, where the metal content M can be Mo and/or W. The formation of precipitates in the matrix can also lead to the development of subgrains. The dislocation pile ups, blocking of dislocation movement and formation of precipitates and subgrains can prevent accelerated deformation rates of this alloy leading to the occurrence of prolonged steady-state region in the creep curves at 750 and 850 ^{o}C. At 950 ^{o}C, these unstable carbides may undergo dissolution, subsequently causing migration of carbides and grain boundaries that could lead to the faster deformation and a short steady-state region under an applied stress of 0.25YS [71].

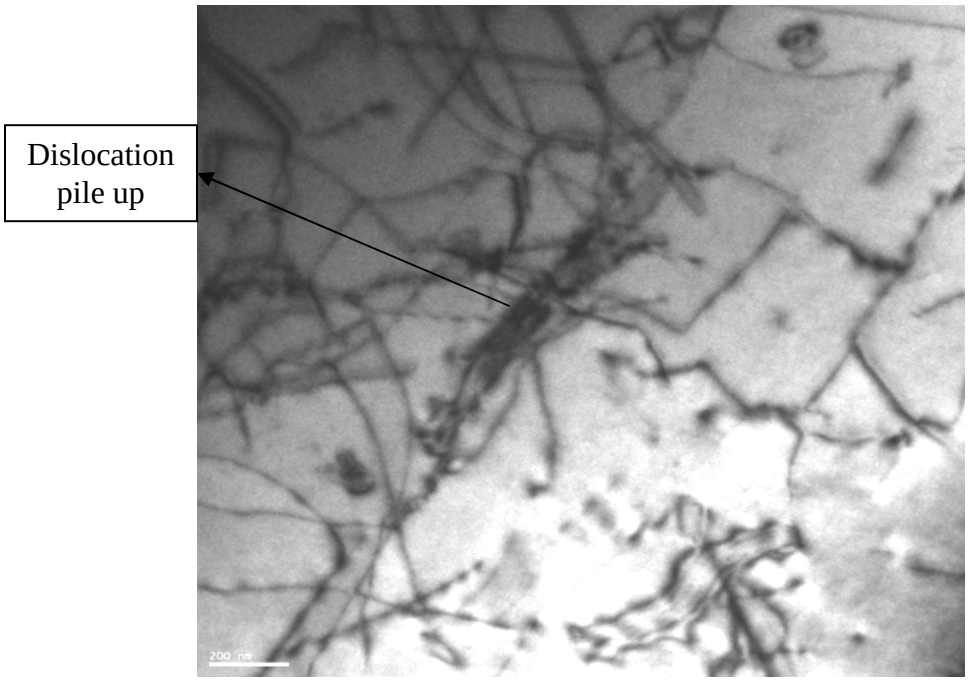

(a)

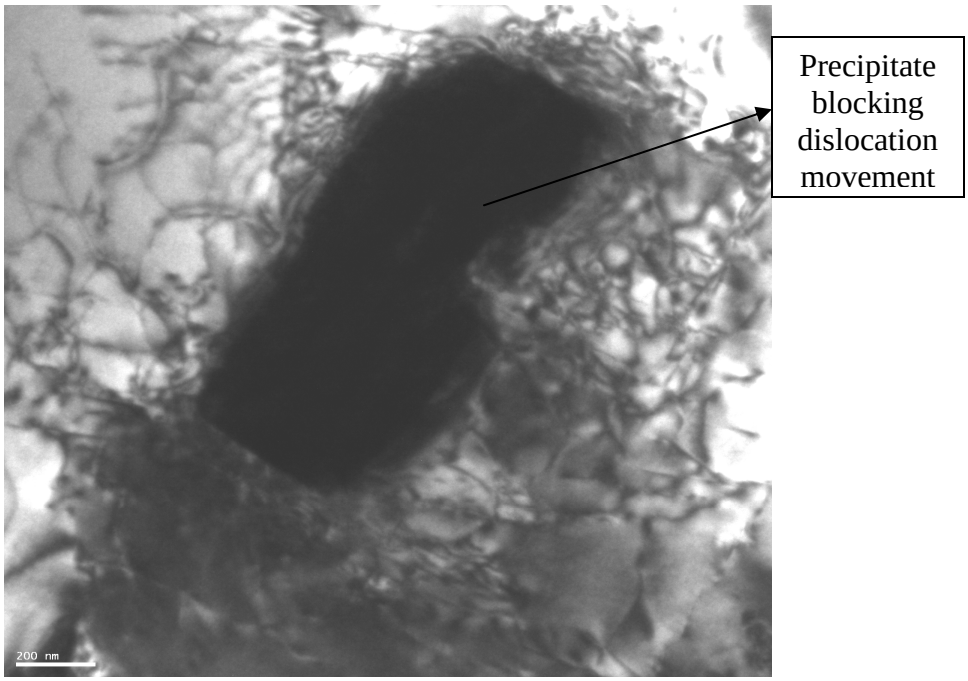
Precipitate blocking dislocation movement
200 nm

(b)

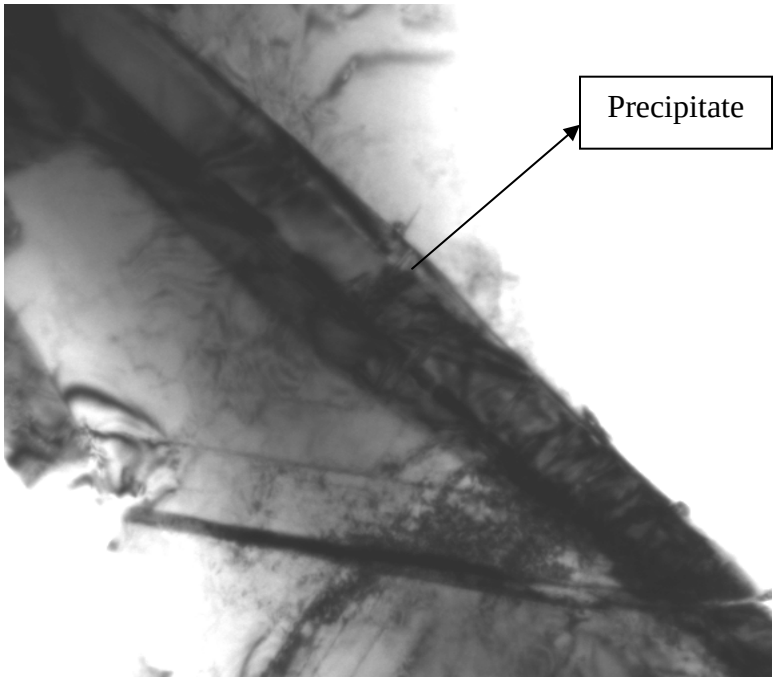
Precipitate

(c)

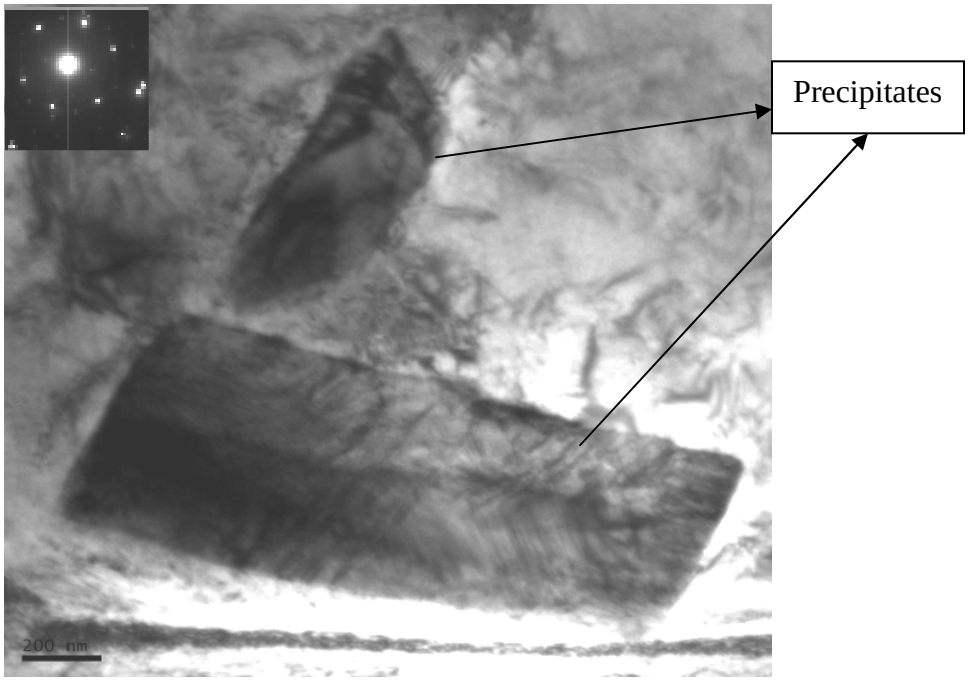

(d)

Figure 4-32 TEM Micrographs

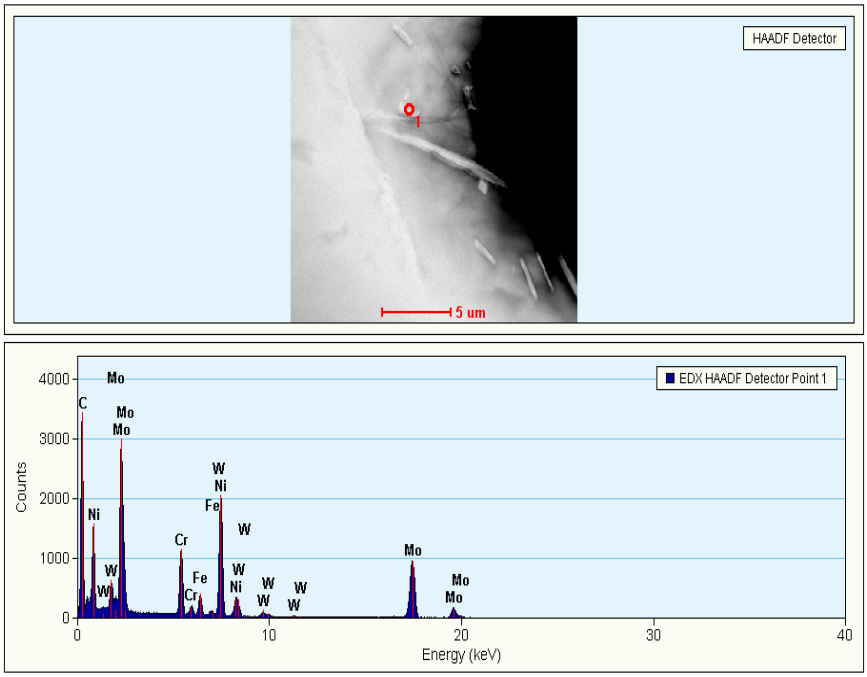

(a) M_6C Precipitate

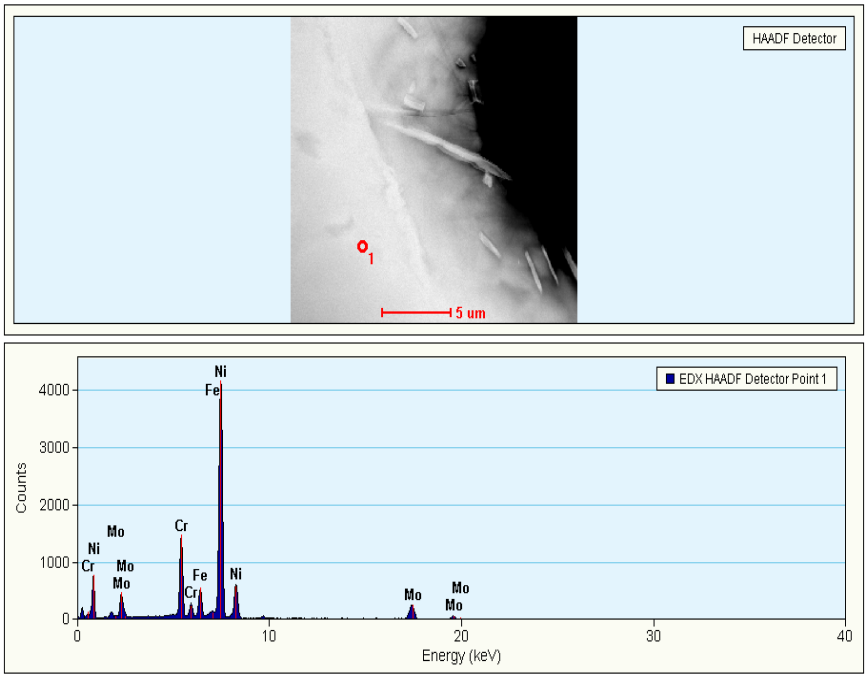

(b) Matrix (Ni-Cr-Mo)

Figure 4-33 STEM Mode EDX Analysis

4.5.3 Grain Size Calculations

The metallurgical microstructures of Alloy 276 specimens used in creep testing at 750, 850 and 950 °C under applied stress levels corresponding to its 0.25YS values are shown in Figure 4-34 (a-c). The ASTM grain size number (G), and the average grain diameter values determined from these micrographs by the mean lineal intercept method are given in Table 4-13. The grain size and the grain diameter of the as-received material are also included in the same table for comparison purpose. A smaller value of G signifies a larger grain size. Thus, the resultant data indicate that the grain size of the tested specimens was gradually enhanced with increasing temperature, showing a substantial growth at 950 °C.

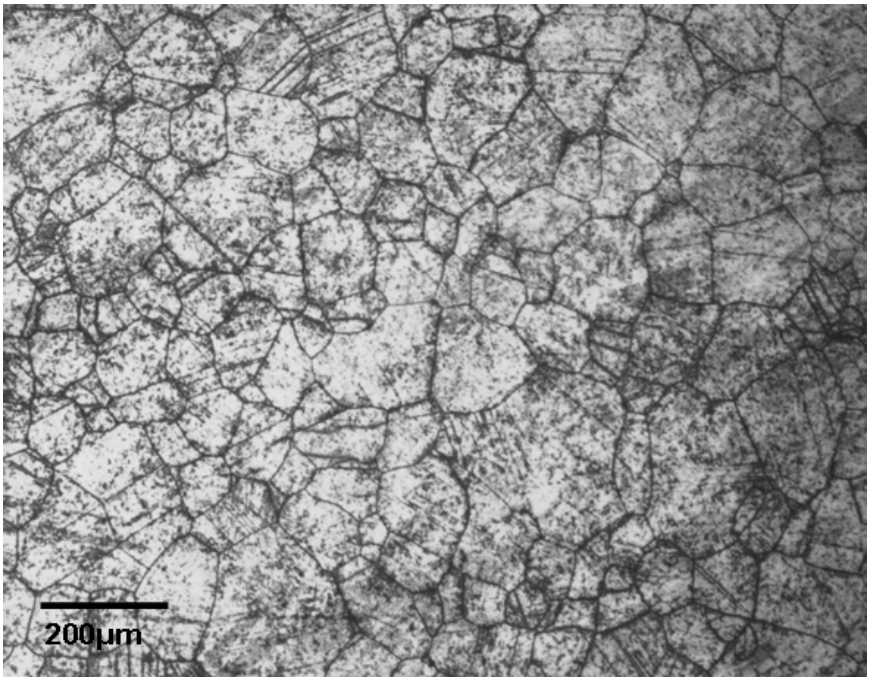

(a) 750 °C

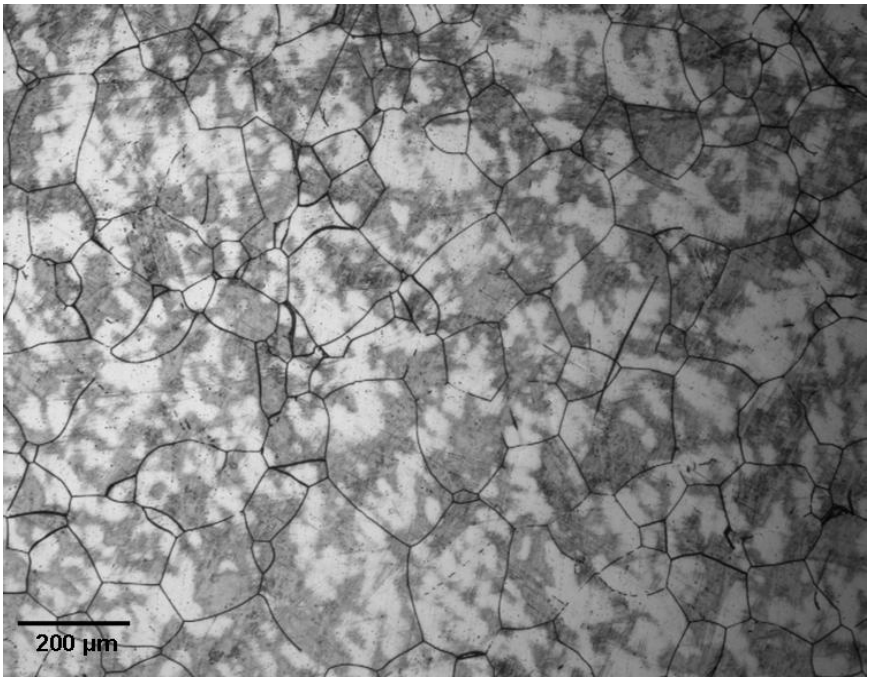

(b) 850 °C

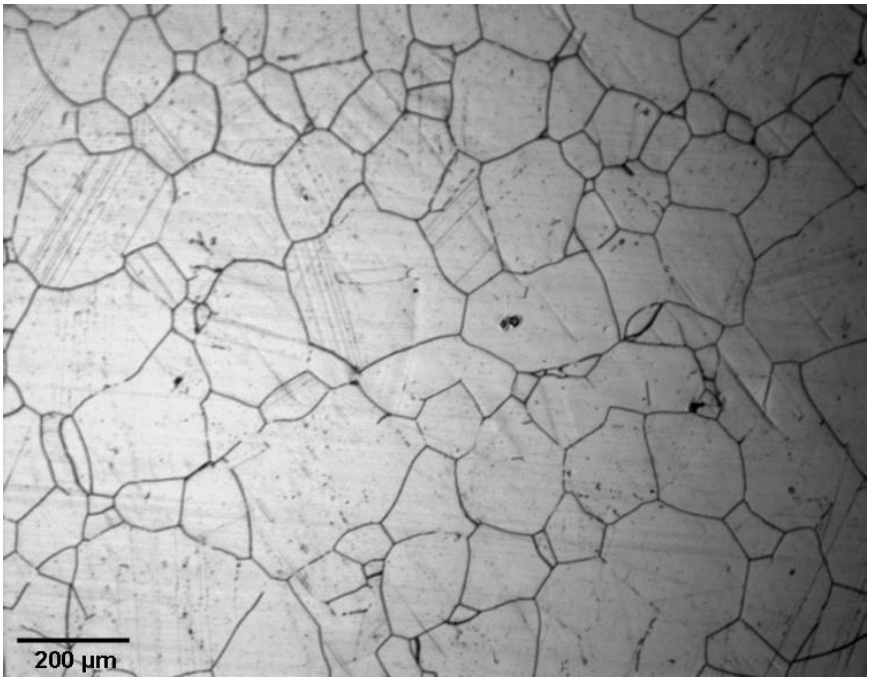

(c) 950 °C

Figure 4-34 Optical Micrographs of Creep Specimens at Different Temperatures

Table 4-13 Grain Size vs. Temperature

Temperature	G	Average Grain Diameter (mm)
Ambient*	3.66 ~ 4	0.101
750 °C	2.66 ~ 3	0.143
850 °C	2.46 ~ 2	0.153
950 °C	1.53 ~ 2	0.212

4.6 Fractographic Evaluation of CT Specimens

The results of fractographic evaluation of the broken surfaces of the CT specimens used in CGR testing at ambient temperature and 300 °C, by SEM, are illustrated in Figures 4-35 and 4-36, respectively. As expected, the cracked region of both specimens was characterized by striations (Figures 4-35a and 4-36a) due to the application of cyclic

* As-received material

loading, thus causing fatigue failures. On the other hand, dimpled microstructures, indicating ductile failures, were observed (Figures 4-35b and 4-36b) beyond the fatigue-cracked region that resulted from fast fracture of the tested specimens due to tensile loading.

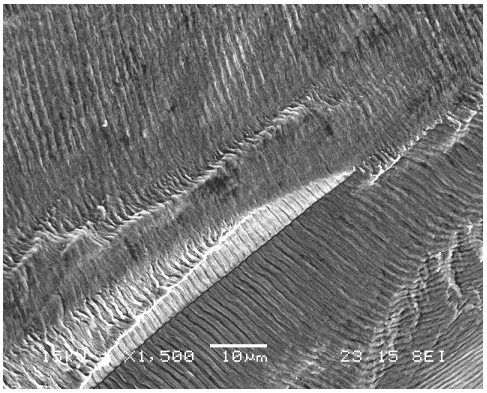

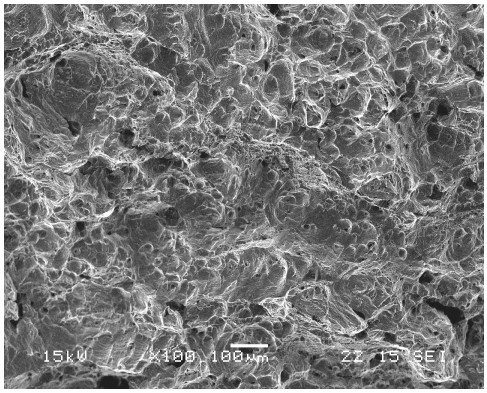

(a) Striations, 1500X (b) Dimples, 100X

Figure 4-35 SEM Micrographs of CT Specimens Tested at Room Temperature

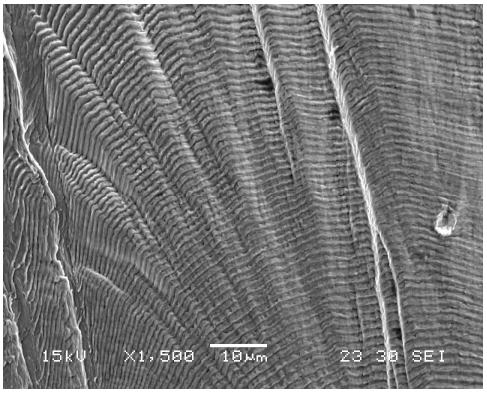

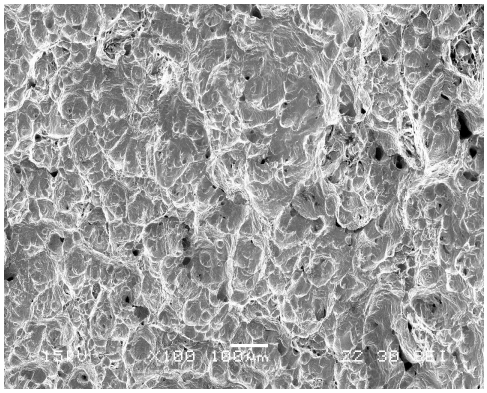

(a) Striations, 1500X (b) Dimples, 100X

Figure 4-36 SEM Micrographs of CT Specimens Tested at 300 °C

CHAPTER 5

DISCUSSION

Two major requirements for a structural material to be suitable for application in the nuclear hydrogen initiative program are its superior resistance to time and temperature induced plastic deformation, and excellent corrosion resistance in an aqueous solution containing chemical species such as sulfuric acid. In view of this rationale, Alloy 276 has been extensively studied in this investigation to evaluate its crack-growth behavior at ambient and elevated temperatures keeping the maximum applied load (P_{max}) at 5 kN while changing the loading ratio (R) from 0.1 to 0.3. A limited number of crack-growth testing has also been performed at constant stress-intensity-factor (K) values. The resistance of this alloy to crack propagation in the presence of a pre-existing crack under tensile loading has been evaluated in terms of J_{IC}, which was based on the elastic-plastic-fracture-mechanics concept of engineering metals and alloys. Further, the susceptibility of this alloy to stress-corrosion-cracking (SCC) has been determined in terms of K before and after exposure of double-cantilever-beam (DCB) specimens in an aqueous solution containing sulfuric acid at 100 °C for variable exposure durations. Time-dependent plastic deformation (creep) of Alloy 276 under sustained loading has also been investigated at three different elevated temperatures. Finally, substantial work has been performed to characterize the metallurgical microstructure, morphology of failure, and nature of defects generated in the tested specimens during plastic deformation under different types of loading.

5.1 Microstructure and Grain Size Evaluations

As anticipated for a nickel-base alloy, Alloy 276 exhibited large austenitic grains and annealing twins at ambient temperature. However, the grain size of this alloy was enhanced to some extent during creep testing at elevated temperatures. The larger grain size at 950 °C indicates that this material can undergo considerable amount of deformation before failure, resulting in loss of strength, and hence, substantial amount of creep.

5.2 Crack-growth-rate Evaluation

With respect to the crack growth behavior of this alloy under cyclic loading (da/dN) at a constant P_{max}, the rate of cracking was substantially higher at 150 °C, irrespective of the R value. Even though the magnitude of da/dN was slightly higher at 300 °C, it could be stated that the final crack length might have reached a critical length within and beyond a temperature range of 100-150 °C. The reduced rate of crack propagation at temperatures above 150 °C could be the result of lower modulus of elasticity (E) values at higher temperatures, indicating reduced stiffness and greater plasticity. Maximum da/dN values were observed at the lowest R value of 0.1 due to a significantly greater loading constraint resulting from the largest load range ($\Delta P = P_{max} - P_{min}$) of 4.5 kN at a constant temperature.

The resultant data also indicate that the number of cycles (N) needed for comparable crack extension was significantly reduced as the temperature was increased from ambient to 150 °C. However, no significant variation in N value was observed between 150 and 300 °C, irrespective of the R value. The results also indicate that the number of cycles to failure (N_f), calculated using Paris equation, was substantially reduced at 150 °C and at

an R value of 0.1, confirming the observation stated earlier. Finally, the activation energy (Q) for crack propagation was somewhat enhanced with increasing R value, suggesting that greater driving forces were necessary for crack extension at higher R values due to reduced loading constraint associated with lower ΔP value. With respect to the da/dN values at constant K_{max}, K_{min}, and thus, constant ΔK values, no significant variation in crack propagation was observed, irrespective of different ΔK values.

Based on the CGR results, the crack propagation almost reached a threshold point at 300 °C, probably due to blunting of the crack-tip at elevated temperatures. Hence, even though testing could not be performed beyond 300 °C due to the failure of the Instron furnace, it can be predicted that the crack growth rate of this alloy would not enhance any further at temperatures higher than 300 °C.

5.3 Fracture Toughness Evaluation

The results of fracture toughness testing indicate that the magnitude of J_{IC} was drastically reduced at 100 °C possibly due to enhanced plasticity of Alloy 276 at a higher temperature, resulting in a higher cracking susceptibility at that temperature. Even though a further drop in J_{IC} value was noted at 200 and 500 °C, these changes were insignificant. A similar effect of temperature on da/dN was also observed, showing reduced rate of crack-growth at 300 °C. Since the fracture toughness values of this alloy were almost constant after 200 °C, testing at temperatures above 500 °C would have probably resulted in the same value for J_{IC}.

5.4 Stress-corrosion-cracking Evaluation

The results of SCC testing involving DCB specimens clearly suggest that the average crack-growth-rate may be reduced with increasing exposure time possibly due to an

attainment of a lowest possible wedge load. Obviously, a critical crack length might have resulted which could not extend further at such insignificant load imparted by the wedge. It is possible that a threshold value of K for SCC (K_{ISCC}) could be determined should the testing be performed beyond eight months of exposure. It is to be noted that due to leaking of the autoclave, SCC testing could not be performed at temperatures beyond 100 °C. In addition, testing at temperatures higher than 300 °C can not be conducted in the liquid phase since the boiling point of sulfuric acid is around 327-340 °C at 100 kPa.

5.5 Creep Evaluation

The results of creep testing suggest that Alloy 276 could be safely used at 750, 850 and 950 °C when loaded at 10 percent of its yield strength (YS) values, without causing excessive plastic deformation. However, this alloy suffered from unacceptable creep strain at 850 and 950 °C under applied stresses equivalent to its 0.25YS values at these temperatures. Dislocation pile ups, blocking of dislocation movement and precipitations of type M_6C carbides within the matrix were observed in the TEM micrographs of the specimen tested at 750 °C at 0.25YS. All these factors can contribute to lower creep deformation at 750 and 850 °C. At 950 °C, these carbides may undergo dissolution, subsequently causing migration of carbides and grain boundaries that could lead to the faster deformation and a short steady-state region.

5.6 Fractographic Evaluation

As anticipated, the broken surfaces of the compact-tension specimens used in da/dN testing exhibited a combination of striations and dimples, indicating brittle and ductile failures due to the application of cyclic loading and tensile fast fracture, respectively. As to the morphology of failure of the DCB specimens used in SCC testing, three fractured

regions including striations, cleavages and ductile tearing were observed on their broken surfaces.

CHAPTER 6

SUMMARY AND CONCLUSIONS

Alloy 276 has been investigated for evaluation of its crack-growth behavior (da/dN), fracture toughness, SCC susceptibility and creep deformation taking different types of mechanical, metallurgical and environmental variables into consideration, where applicable. The key results and the conclusions derived from the overall data are summarized below.

- Large austenitic grains and annealing twins, common microstructural characteristics of solution-annealed nickel-base alloys, were evident in the optical micrograph.
- The average grain size of Alloy 276 was slightly enhanced due to a change in temperature from ambient to 950 °C.
- The magnitude of da/dN was gradually enhanced with increasing temperature at a constant R value. However, the temperature effect on da/dN was more pronounced at 150 °C, possibly due to a greater plasticity and reduced modulus elasticity at this temperature.
- Maximum da/dN values were observed at the lowest R value of 0.1 due to a greater loading constraint associated with the largest ΔP value of 4.5 kN at a constant temperature.
- Consistent with the maximum da/dN values at an R value of 0.1, a lowest number of cycles to failure (N_f) was also observed at this R value, irrespective of the testing temperature. Also, the number of cycles needed for comparable

crack extension at a constant R value was gradually reduced at relatively higher temperatures. This is due to the fact that at a higher temperature the da/dN values were higher which required less number of cycles for crack growth.

- Even though the slope (m) of the steady-state region in the da/dN versus ΔK plot was not influenced by temperature, a greater value of intercept (A) was observed at higher temperatures, indicating enhanced cracking tendency.
- An average activation energy (Q) for crack-growth of 308 J/mole was calculated for Alloy 276, which appears to be close to a Q value for a similar type of austenitic alloy.
- In constant-K testing, the variation of crack length with the number of cycles exhibited a linear relationship, irrespective of the ΔK values, which was consistent with the literature. Further the variation of ΔK values did not exhibit any significant effect on the da/dN values.
- While a significant drop in the J_{IC} value was noted at 100 °C, its variations at higher temperatures were insignificant.
- The difference in stress-intensity-factor values before and after SCC testing (ΔK) was enhanced with DCB specimens loaded to higher initial stress-intensity-factor (K_I) values. Further, the magnitude of average crack-growth-rate was gradually reduced with longer test duration.
- The extent of creep deformation for Alloy 276 fell within the acceptable strain range when loaded to its 0.10YS values at 750, 850 and 950 °C. Hence, this

material can be safely used in heat exchanger applications when the applied stress is less than 0.10YS (~ 2-3 ksi / 15-20 MPa).

- The activation energies for creep deformation were found to be approximately 242.98-300.31 kJ/mole and 205.15-208.37 kJ/mole at applied stresses of 0.10 and 0.25YS, respectively, which are consistent with the literature for similar types of alloys.
- Precipitation of M_6C carbides could lead to higher creep resistance at 750 °C when the applied stress was 0.25YS. Dissolution of these carbides could possibly account for higher creep deformation at 950 °C.
- Fatigue cracking of CT specimens was characterized by striations. On the other hand, dimpled microstructures indicated ductile failure due to tensile loading of these specimens following da/dN testing.
- The DCB specimens exhibited combined fatigue (striations), brittle (cleavage), and ductile (dimples) failures on their broken surfaces due to cyclic loading, SCC and fast fracture.

CHAPTER 7

SUGGESTED FUTURE WORK

- Due to equipment failure and constrained funding, CGR testing could not be performed beyond 300 °C. Even though prediction for crack growth behavior of this alloy at higher temperatures has been made in Chapter 5, it is suggested that testing be performed at temperatures above 300 °C for additional observations.
- J_{IC} testing can be performed at temperatures above 500 °C to confirm the prediction on the fracture toughness behavior of this alloy based on the results of the current study.
- Since the K_{ISCC} value for Alloy 276 was not achieved even after testing for 8 months duration, it is suggested that SCC testing with DCB specimens should be performed for longer exposure periods to determine the magnitude of K_{ISCC}.

APPENDIX A

CRACK-GROWTH-RATE TESTING DATA

A1 Direct-current-potential-drop (DCPD) System

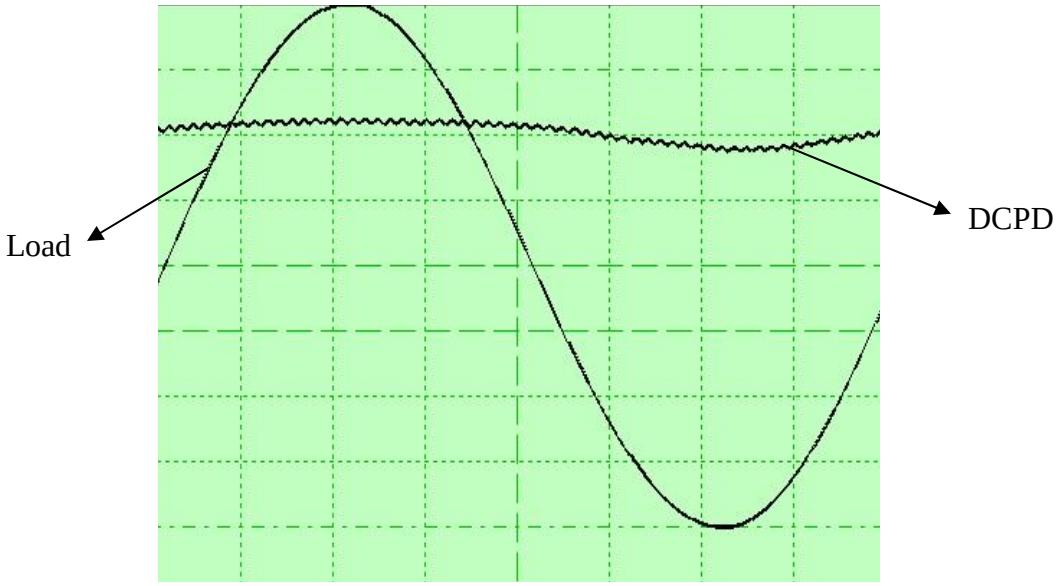

Load vs. DCPD

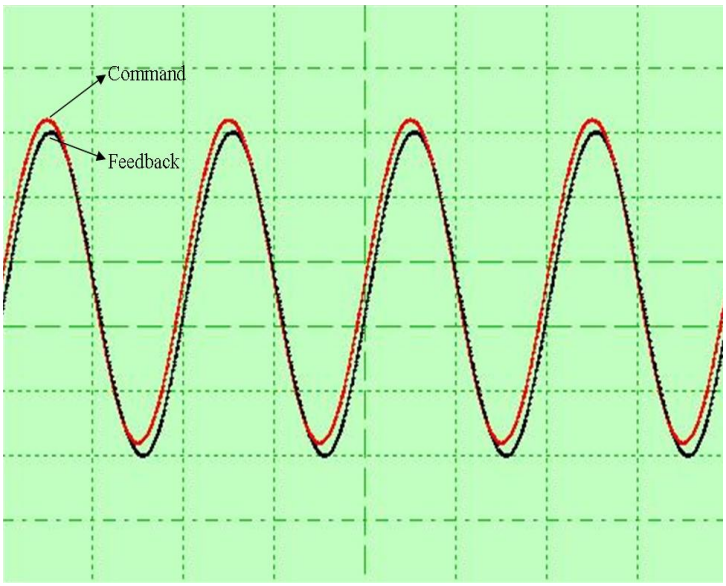

Command Load (DCPD) vs. Feedback Load (Instron)

A2 Constant-Load CGR Testing Data

A2.1 da/dN vs. ΔK Plots

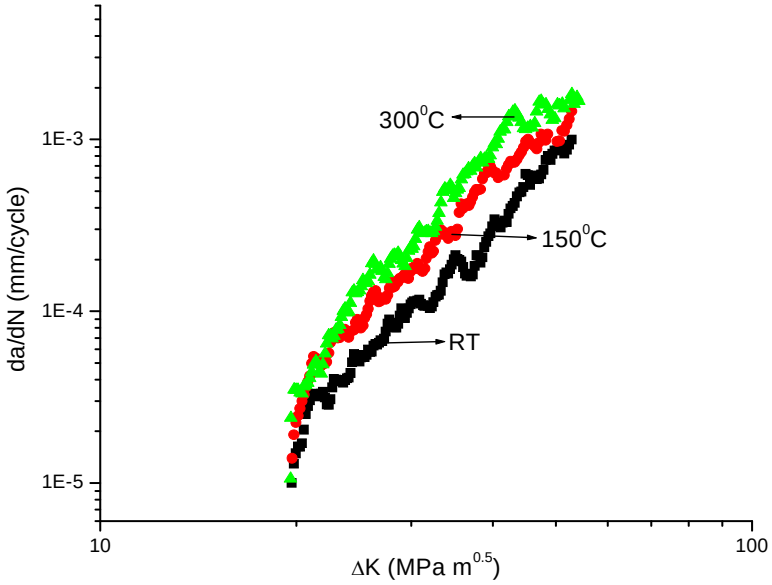

R = 0.1 (Sample 2)

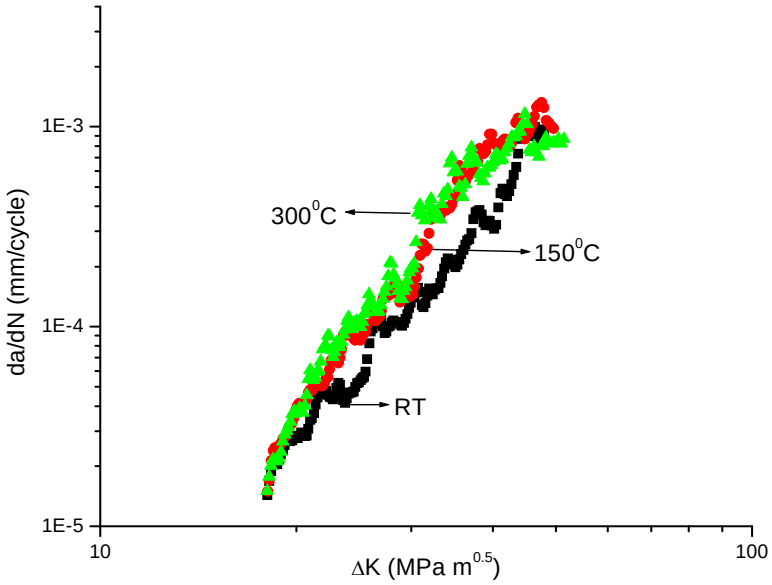

R = 0.2 (Sample 2)

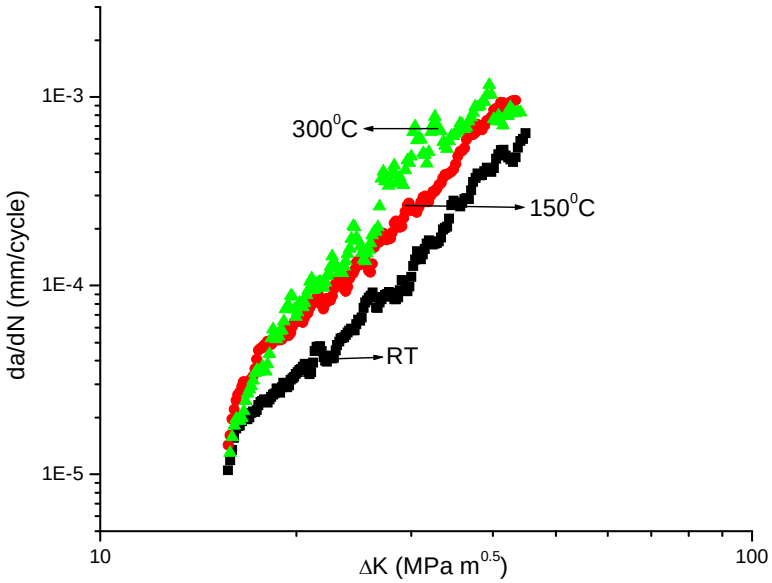

R = 0.3 (Sample 3)

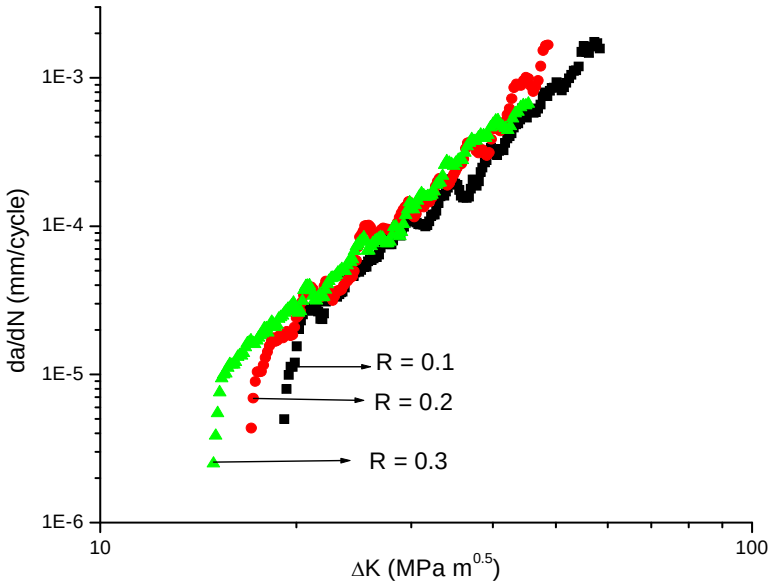

Room Temperature (Sample 1)

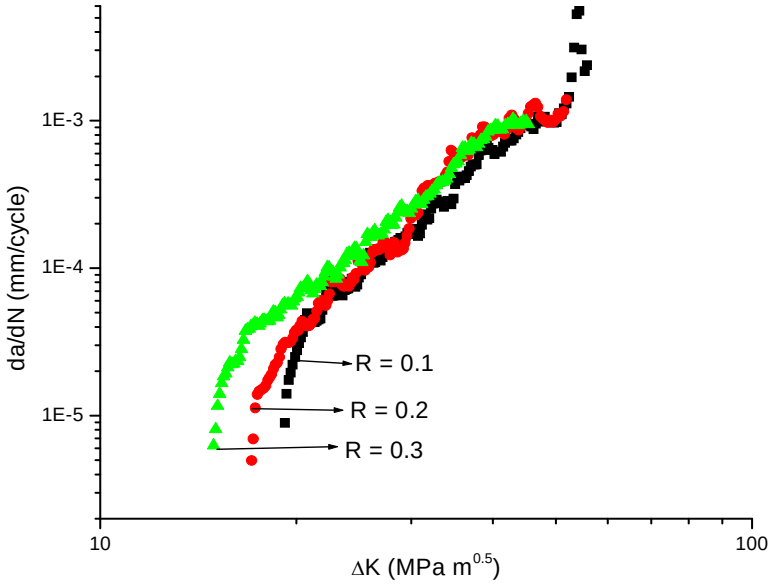

150 °C (Sample 1)

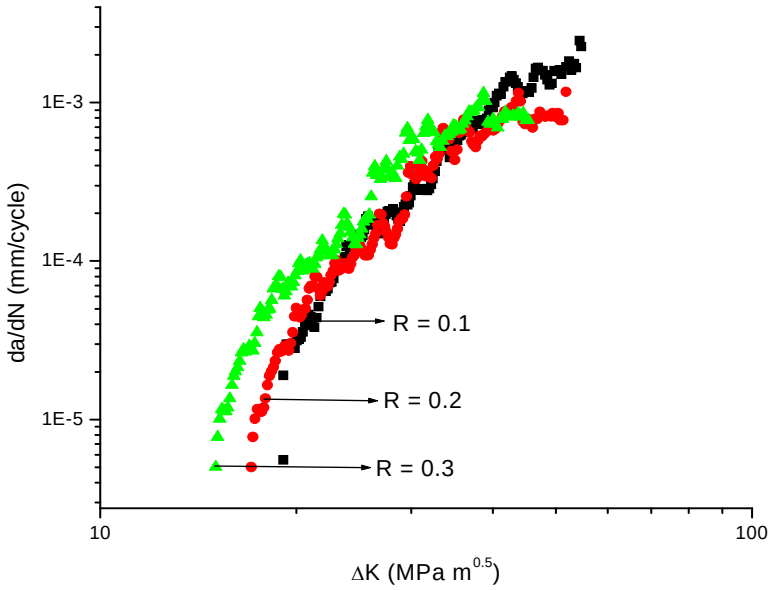

300 °C (Sample 1)

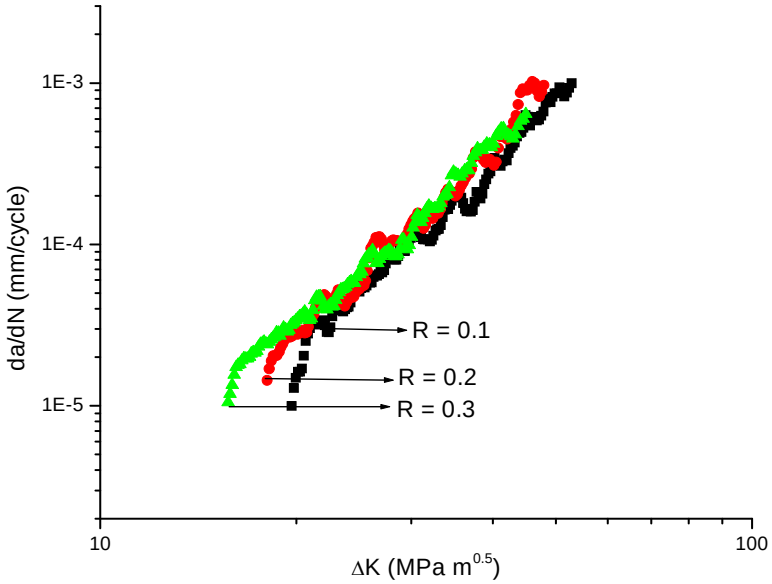

Room Temperature (Sample 2)

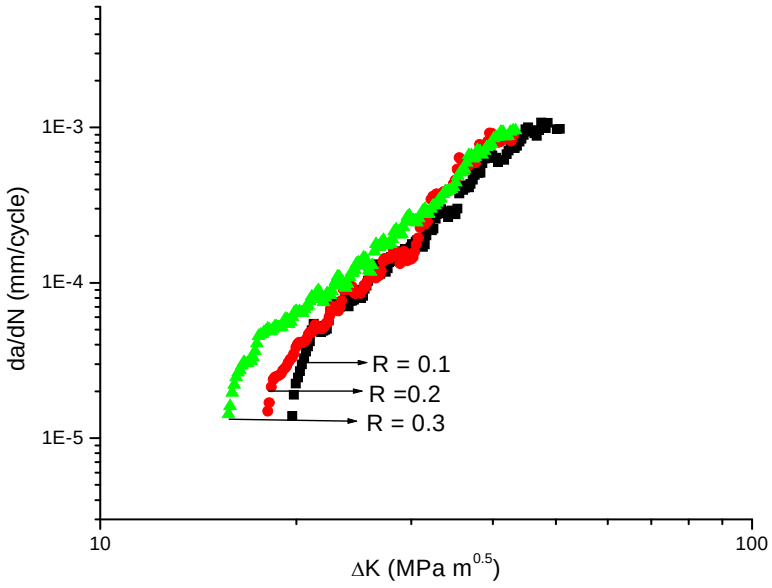

150 °C (Sample 2)

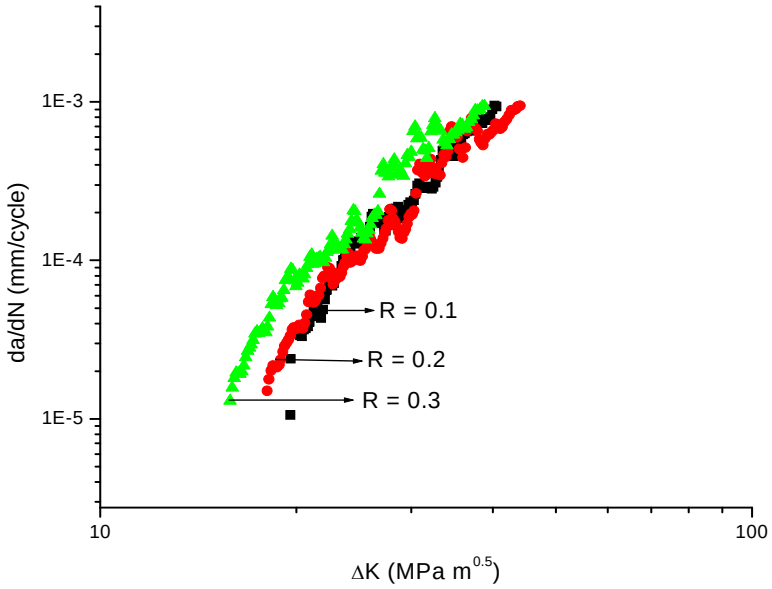

300 °C (Sample 2)

A2.2 Crack-length (a) vs. Number of Cycles (N) Plots

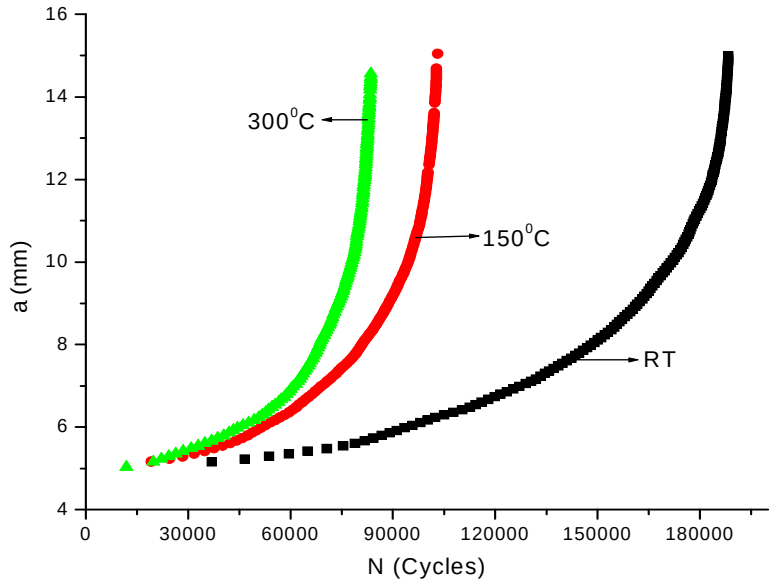

R = 0.1 (Sample 2)

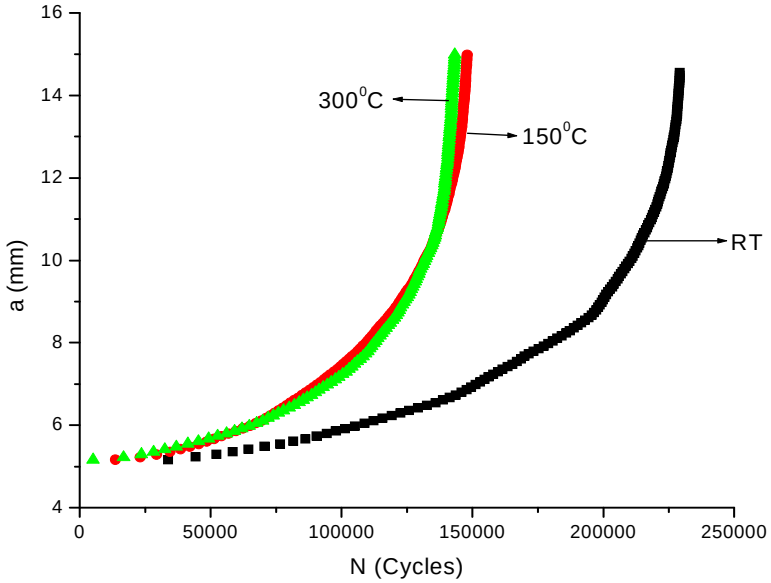

R = 0.2 (Sample 2)

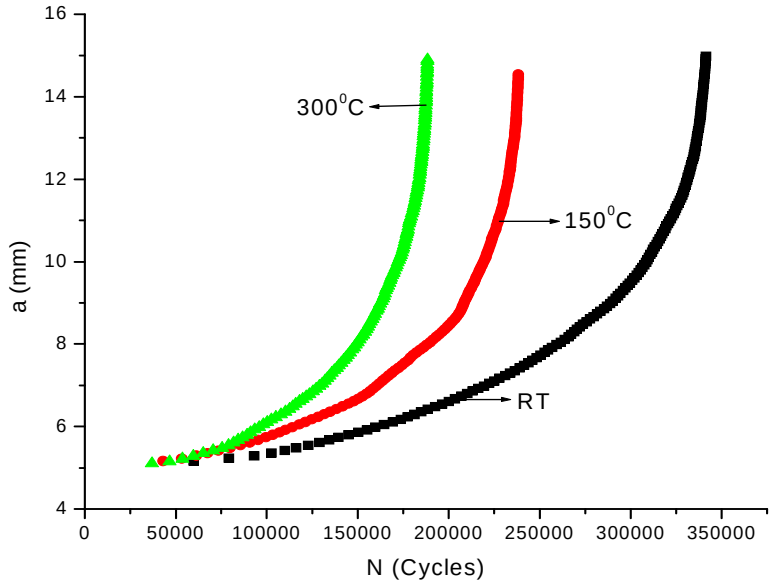

R = 0.3 (Sample 2)

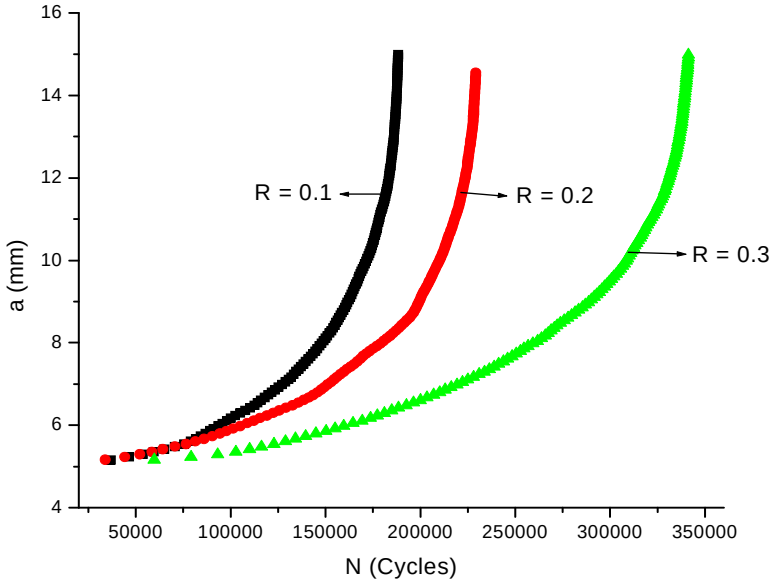

Room Temperature (Sample 2)

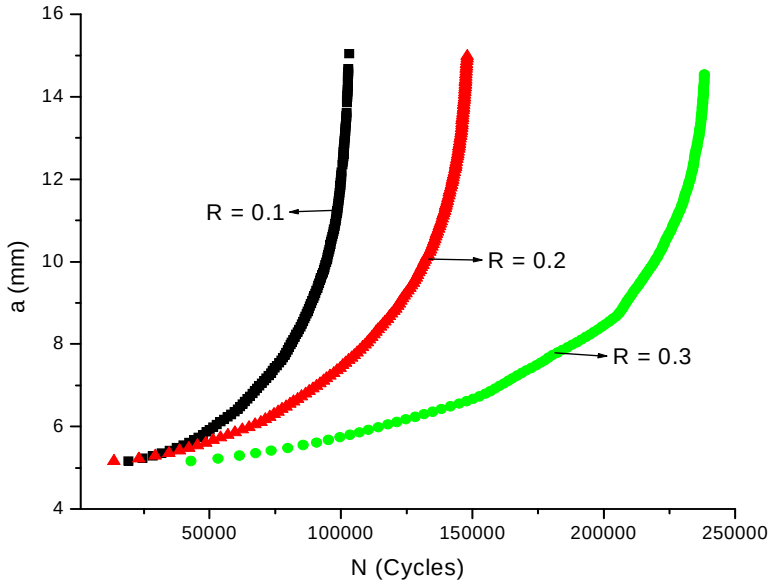

150 °C (Sample 2)

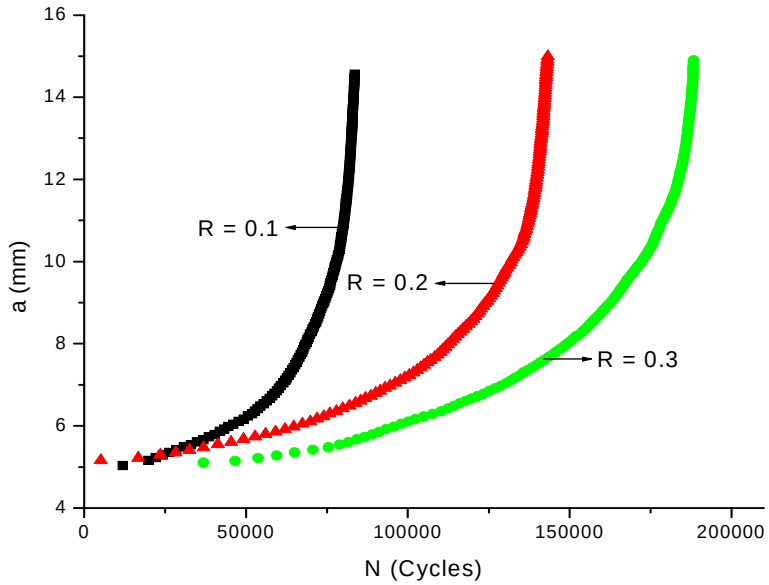

300 °C (Sample 2)

A2.3 Number of Cycles (N) vs. Temperature (T) Plots

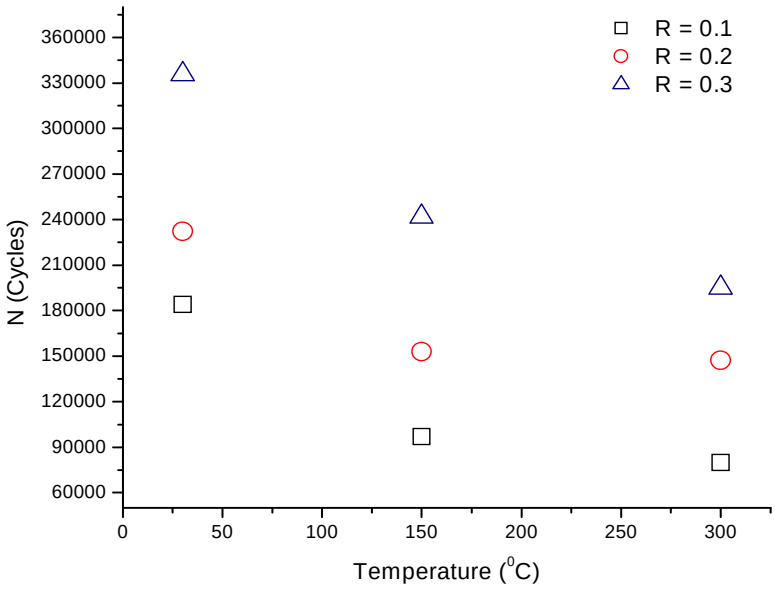

Sample 1

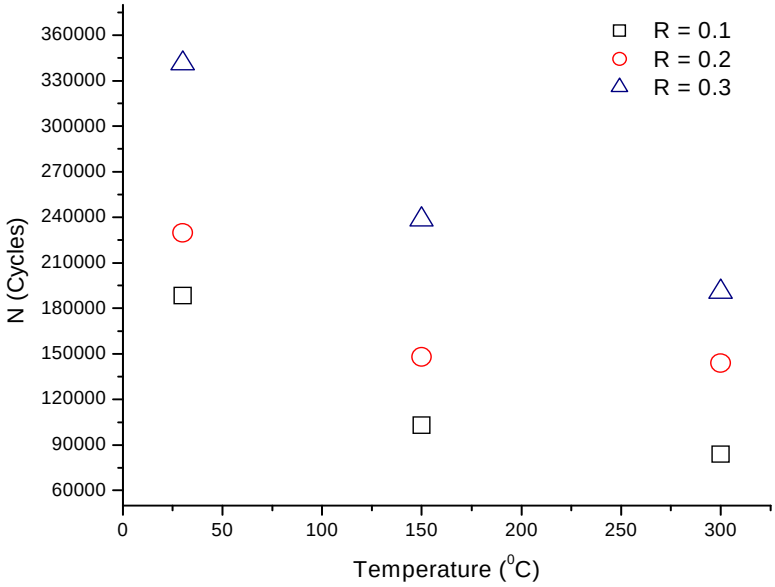

Sample 2

A2.4 Number of Cycles (N) vs. Load Ratio (R) Plots

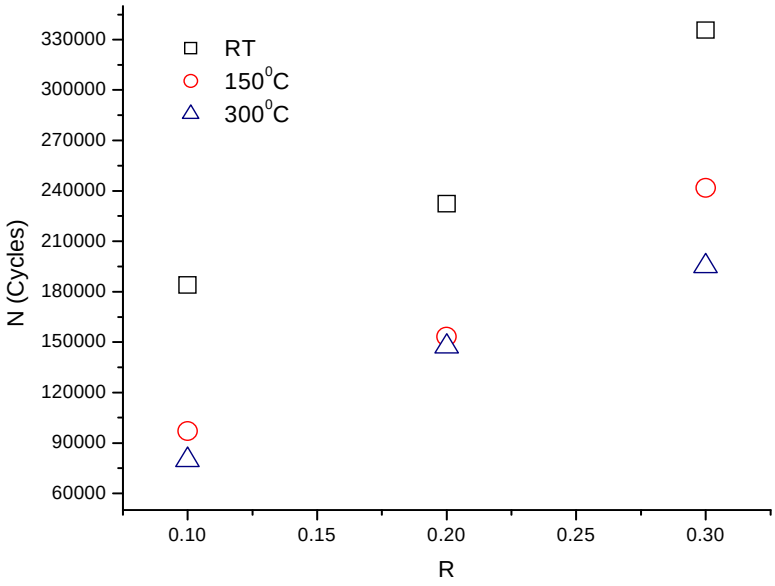

Sample 1

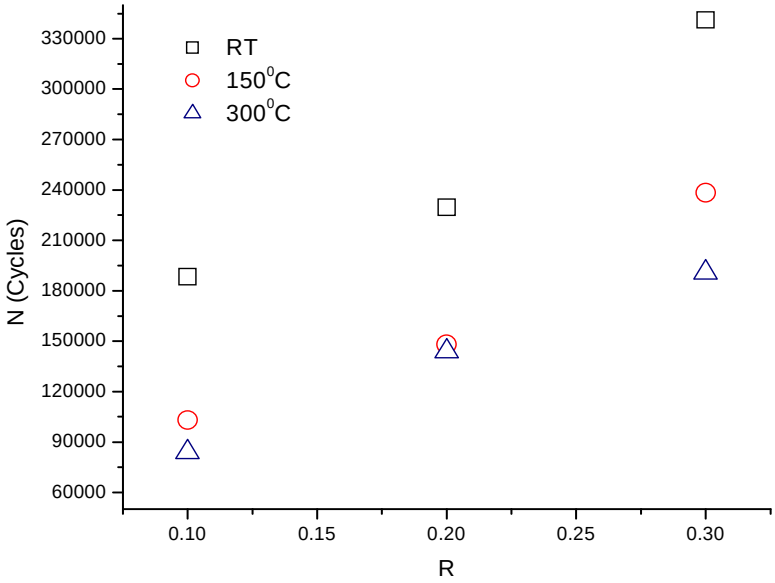

Sample 2

A2.5 Number of Cycles to Failure (N_f) vs. Temperature (T) Plots

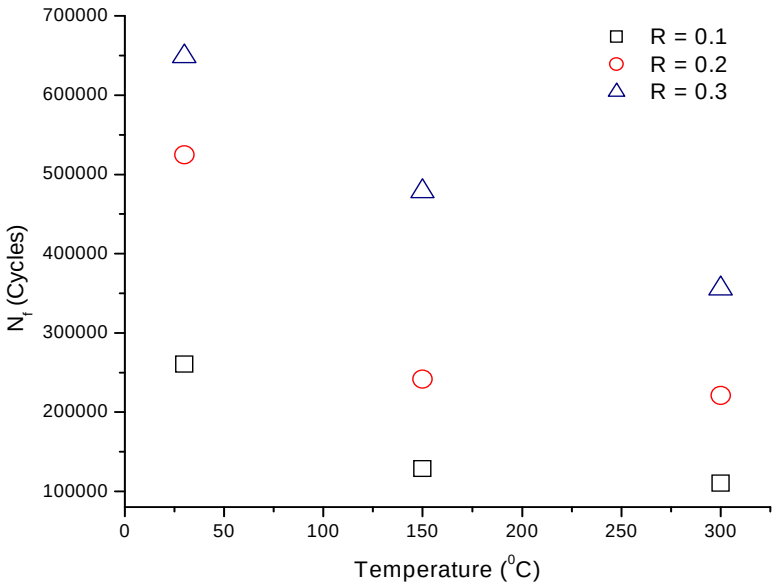

Sample 1

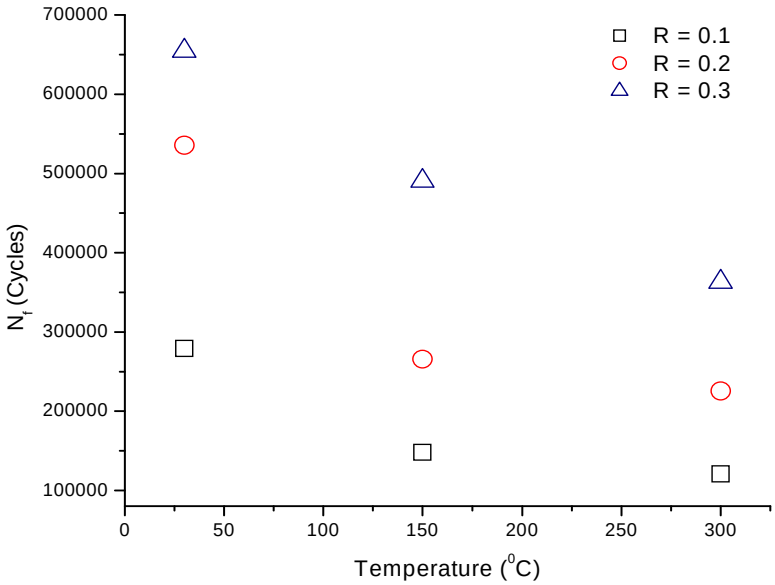

Sample 2

A2.6 Number of Cycles to Failure (N_f) vs. Load Ratio (R) Plots

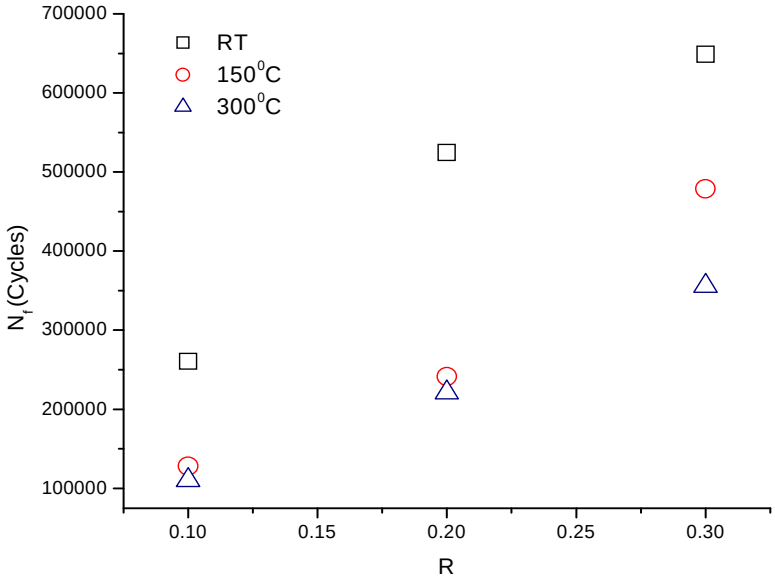

Sample 1

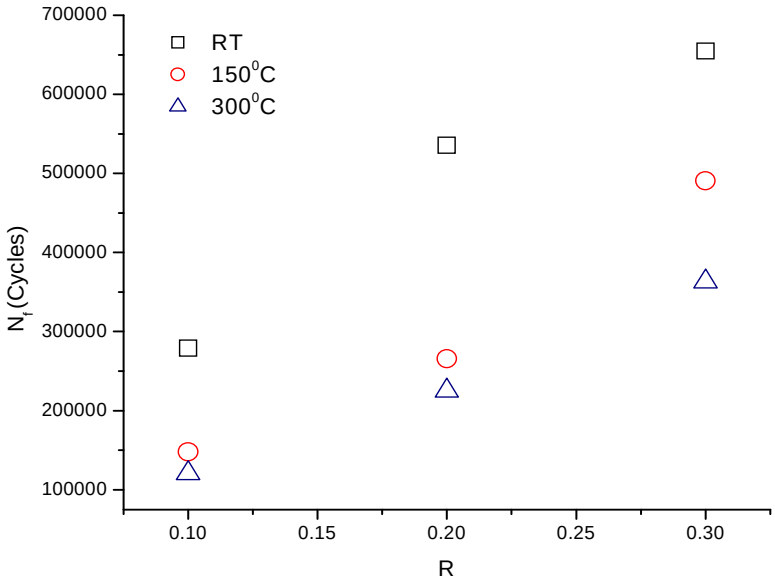

Sample 2

A2.7 Slope (m) Values

Temperature (°C)	m					
	R = 0.1		R = 0.2		R = 0.3	
	Sample 1	Sample 2	Sample 1	Sample 2	Sample 1	Sample 2
Room Temperature	4.10	3.90	3.85	3.79	3.89	3.87
150	3.98	3.96	3.86	3.80	3.73	3.71
300	3.91	3.93	3.78	3.82	3.83	3.81

A2.8 Crack-growth Coefficient (A) Values

Temperature (°C)	A ($\times 10^{-13}$ MPa$\sqrt{m}$)					
	R = 0.1		R = 0.2		R = 0.3	
	Sample 1	Sample 2	Sample 1	Sample 2	Sample 1	Sample 2
Room Temperature	1.25	1.19	1.17	1.13	1.01	1.09
150	3.05	2.93	2.87	2.91	2.78	2.72
300	3.72	3.68	3.56	3.64	3.47	3.53

A2.9 Threshold Stress-intensity-factor-range (ΔK_{th}) Values

Temperature (°C)	ΔK_{th} (MPa√m)					
	R = 0.1		R = 0.2		R = 0.3	
	Sample 1	Sample 2	Sample 1	Sample 2	Sample 1	Sample 2
Room Temperature	18.79	19.01	16.76	16.78	14.77	14.24
150	18.55	18.96	16.90	16.87	14.64	14.52
300	19.07	18.94	16.85	16.94	14.81	14.74

A2.10 Activation Energy (Q) Values

R	Q (J/mole) Sample 1	Average Q (J/mole)	R	Q (J/mole) Sample 2	Average Q (J/mole)
0.1	293.0	307.4	0.1	300.6	307.9
0.2	297.4		0.2	313.0	
0.3	331.9		0.3	310.1	

A2.11 ln (A) vs. 1/T

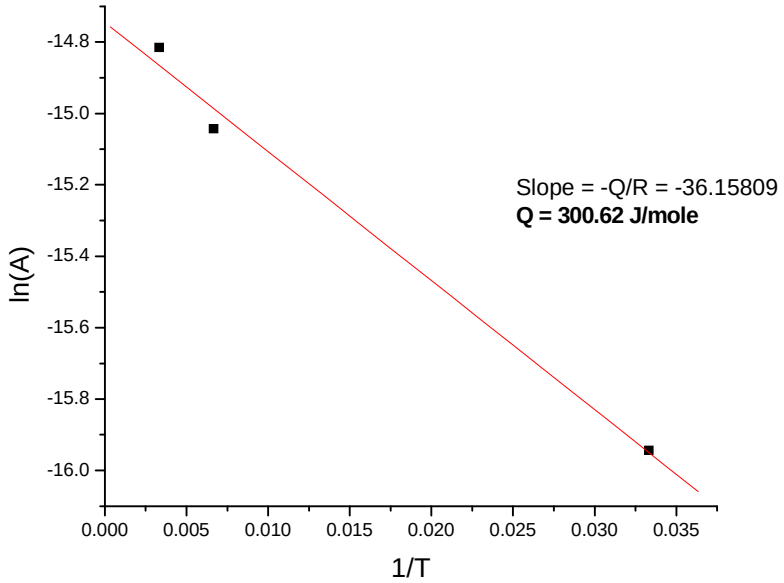

R = 0.1 (Sample 2)

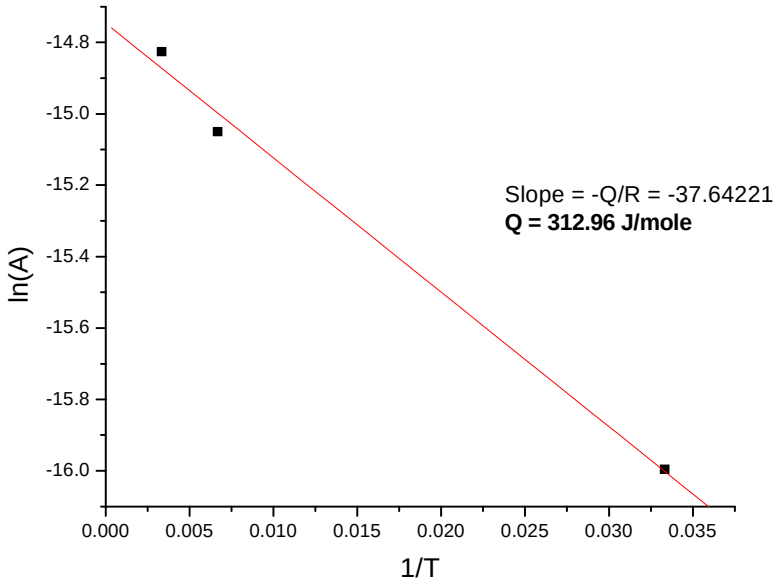

R = 0.2 (Sample 2)

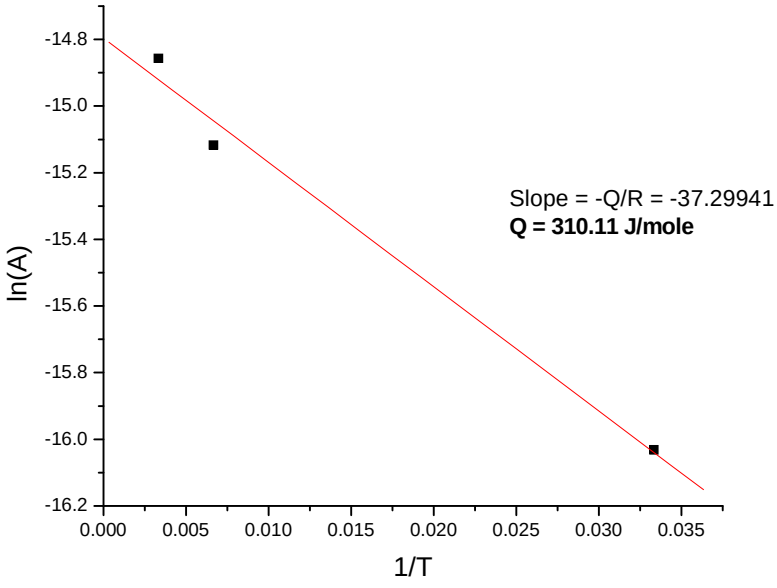

R = 0.3 (Sample 2)

A3 Ambient-Temperature Constant-K CGR Testing Data

A3.1 Crack-length (a) vs. Number of Cycles (N) Plot

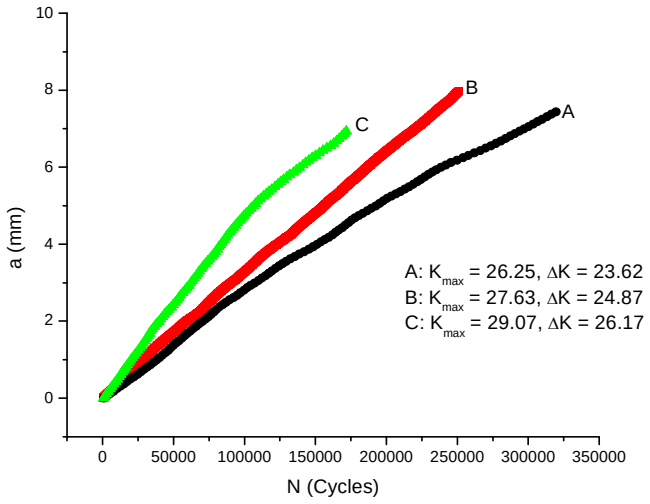

Sample 2

A3.2 Crack-length (a) vs. Load (P) Plot

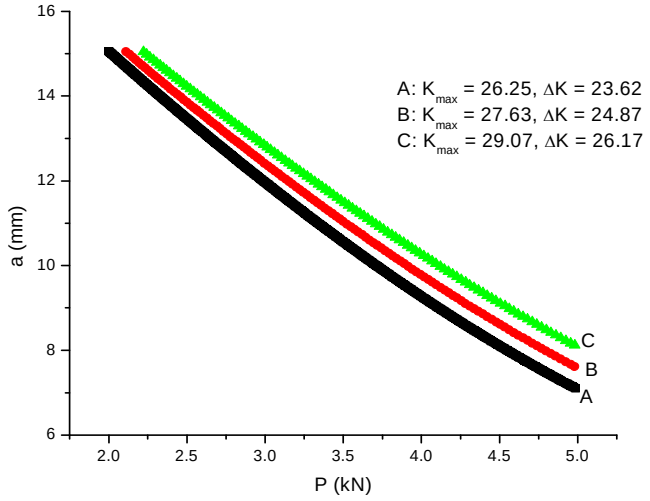

Sample 2

A3.3 da/dN and N Values

ΔK (MPa√m)	Average da/dN (mm/cycle) $\times 10^{-5}$		N (Cycles)	
	Sample 1	Sample 2	Sample 1	Sample 2
23.62	2.57	3.14	483076	408542
24.87	3.18	2.35	392637	488664
26.17	3.64	4.15	324909	335821

APPENDIX B

FRACTURE TOUGHNESS TESTING DATA

B1 Fracture Toughness (J_{IC}) Values

Temperature (°C)	J_{IC} (KJ/m^2)	
	Sample 1	Sample 2
Room Temperature	161.3	150.0
100	100.5	105.3
200	87.1	89.1
500	86.5	85.9

B2 Fracture Toughness (K_{IC}) and CTOD (δ) Values

Temperature (°C)	K_{IC} (MPa$\sqrt{m}$)		δ (mm)	
	Sample 1	Sample 2	Sample 1	Sample 2
Room Temperature	195.6	188.6	0.25	0.23
100	154.1	157.7	0.18	0.19
200	142.5	144.1	0.18	0.18
500	138.9	138.4	0.21	0.21

B3 Tearing Modulus (T) Values

Temperature (°C)	T	
	Sample 1	Sample 2
Room Temperature	381.1	374.4
100	483.3	474.0
200	545.5	543.1
500	563.8	550.8

APPENDIX C

CREEP TESTING DATA

C1 Isothermal Creep Curves

C1.1 750 °C

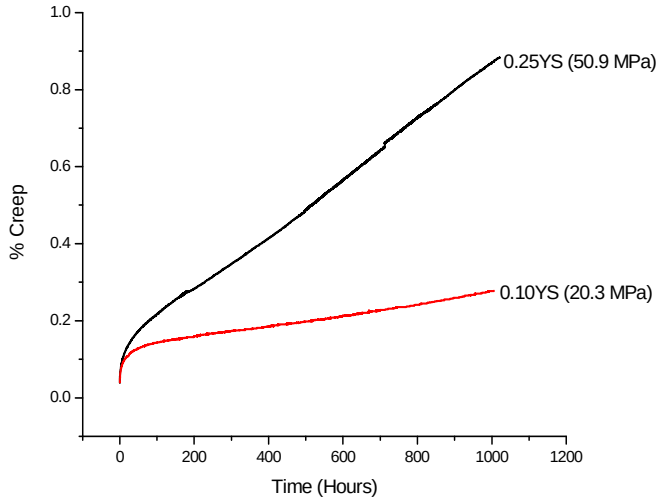

C1.2 850 °C

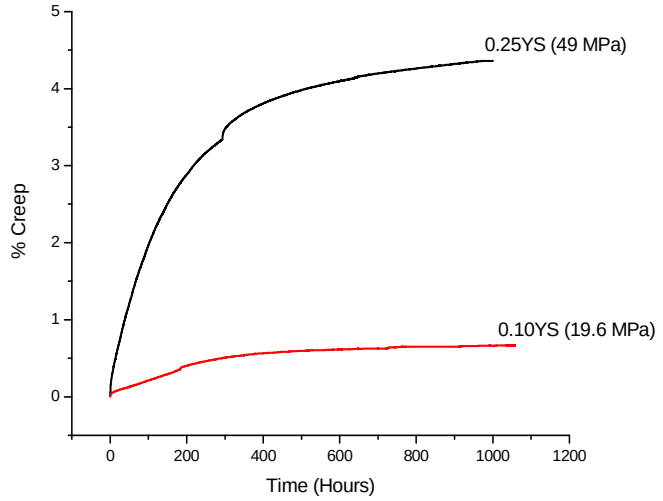

C1.3 950 °C

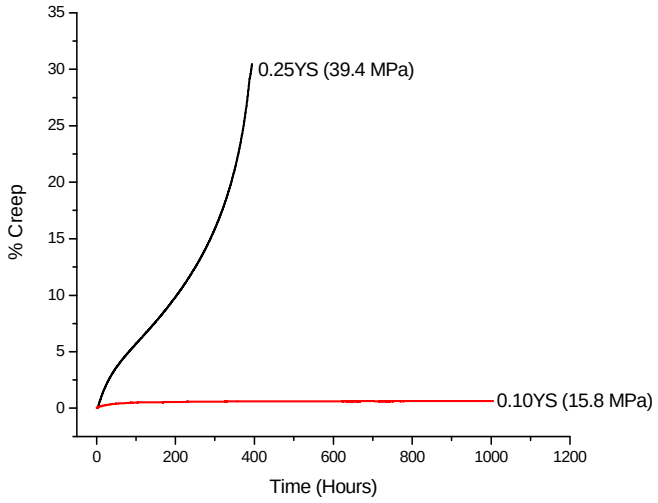

C2 Initial Rapid Elongation vs. Temperature and Applied Stress

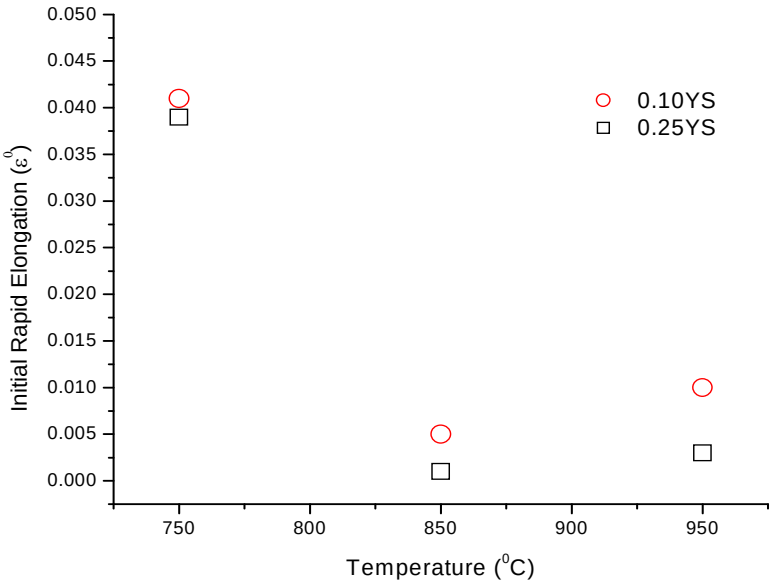

C3 Creep Rate vs. Applied Stress

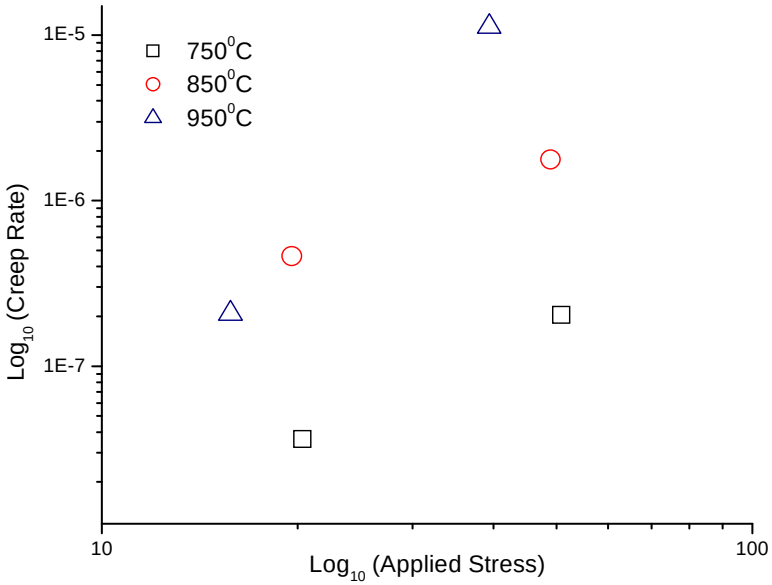

C4 Activation Energy (Q) Values

Method	Q Values (kJ/mole)		Average Q Values (kJ/mole)	
	Applied Stress = 0.10YS	Applied Stress = 0.25YS	Applied Stress = 0.10YS	Applied Stress = 0.25YS
$\dot{\varepsilon}_s = A\exp(-Q/RT)$	-	208.15	271.65	207.22
$Q = \frac{R \ln(\dot{\varepsilon}_1 / \dot{\varepsilon}_2)}{(1/T_2 - 1/T_1)}$	242.98	208.37		
$\dot{\varepsilon} = A\sigma^n \exp(-Q/RT)$	300.31	205.15		

APPENDIX D

SCANNING ELECTRON MICROGRAPHS

D1 SEM Micrographs of CT Specimens Tested for da/dN Studies

D1.1 Ambient Temperature, R = 0.2

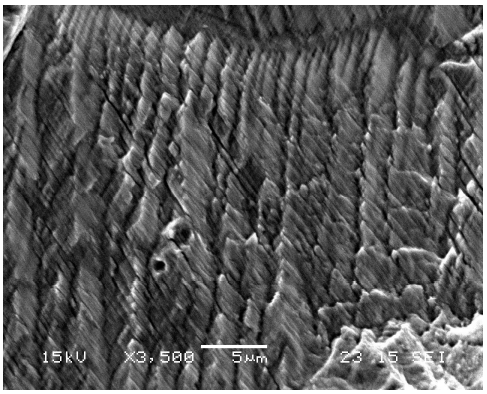

Striations

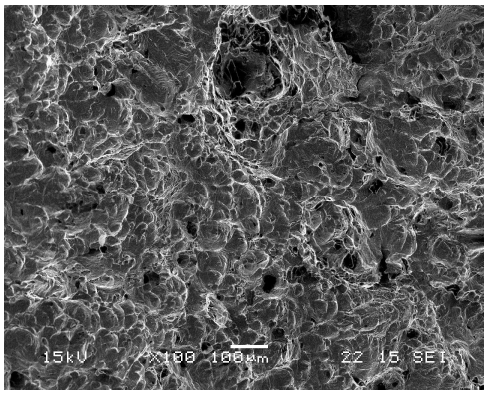

Dimples

D1.2 Ambient Temperature, R = 0.3

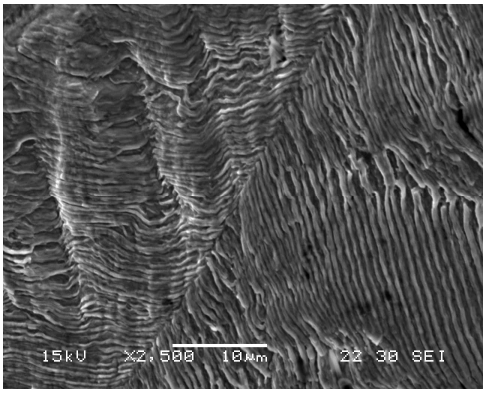

Striations

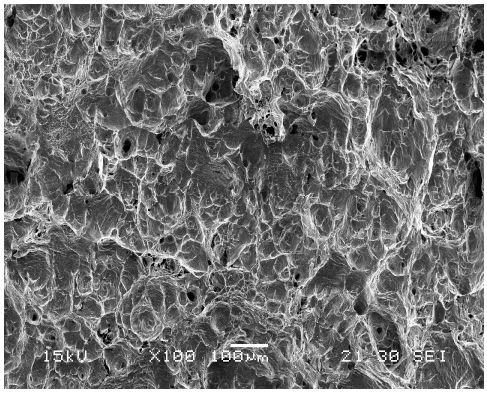

Dimples

D1.3 150 °C, R = 0.1

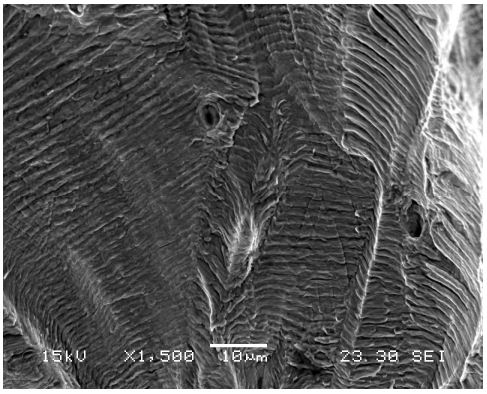

Striations

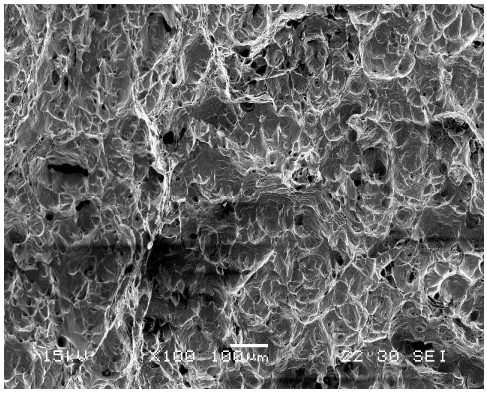

Dimples

D1.4 150 °C, R = 0.2

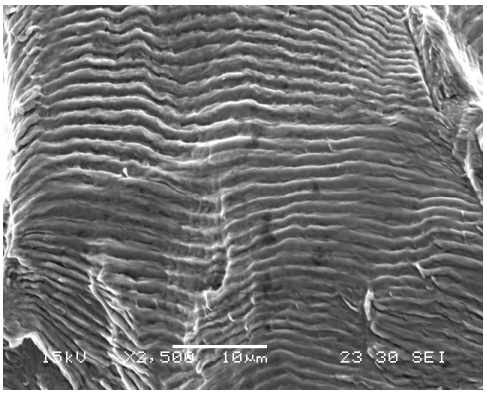

Striations

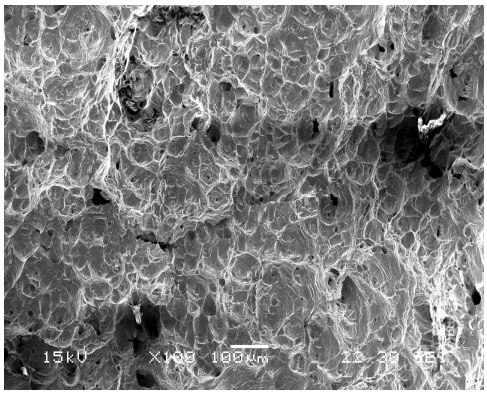

Dimples

D1.5 150 °C, R = 0.3

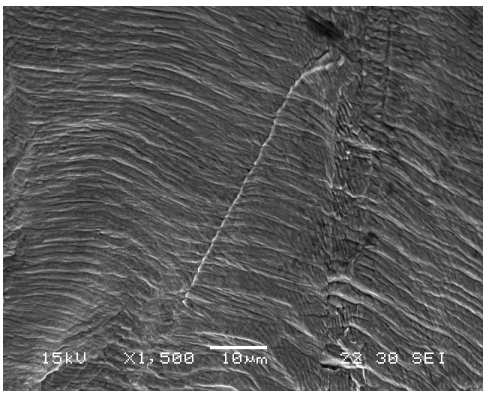

Striations

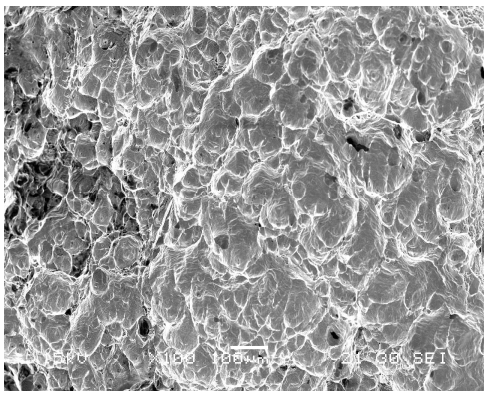

Dimples

D2 SEM Montage Micrographs of DCB Specimens Tested for Variable Exposure Periods

D2.1 1-month Test Duration, Low K_I

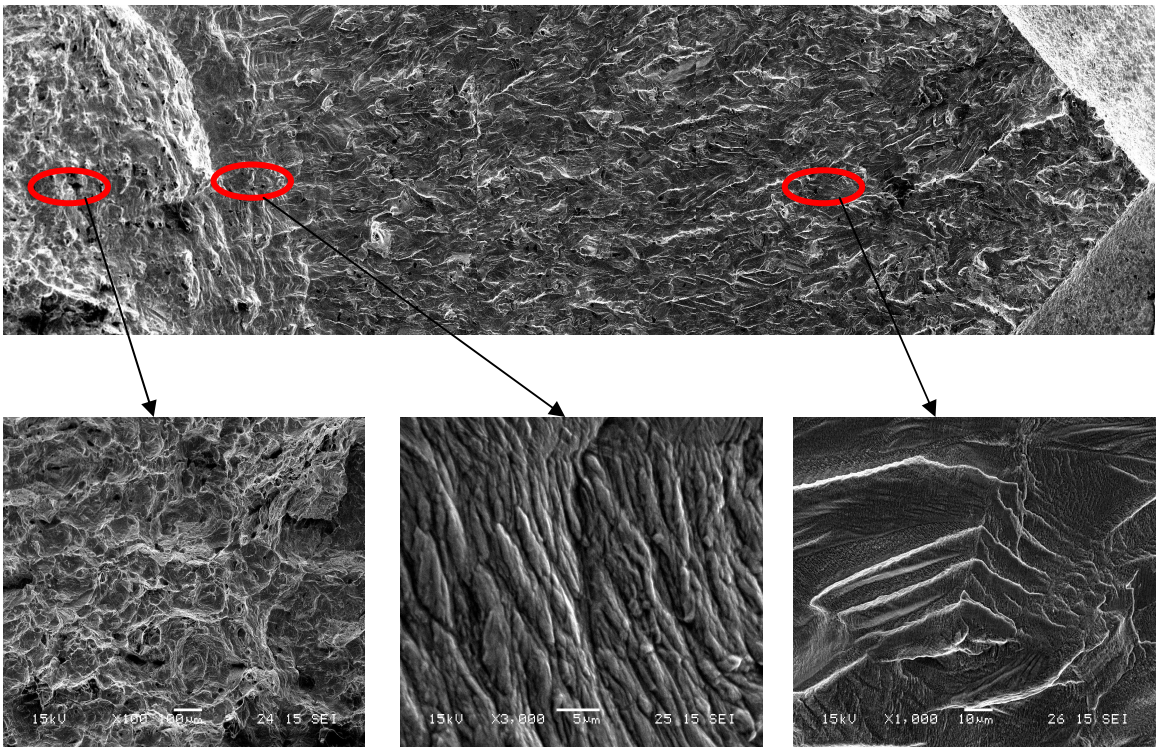

Fast Fracture Region (Dimples)

SCC Region (Cleavages)

Fatigue Pre-crack Region (Striations)

D2.2 1-month Test Duration, High K_I

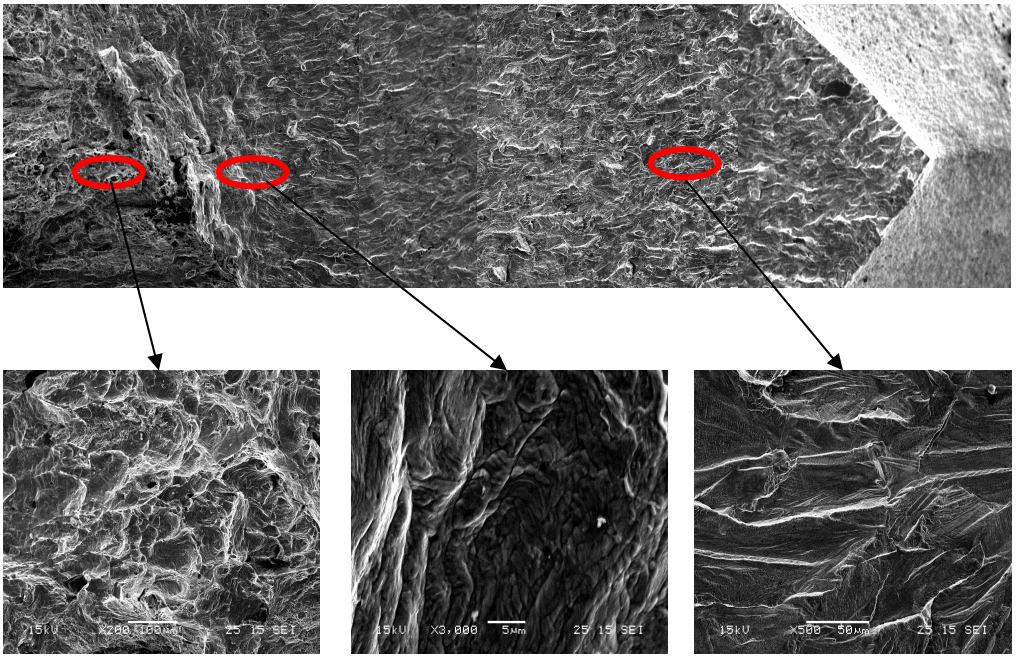

Fast Fracture Region (Dimples)

SCC Region (Cleavages)

Fatigue Pre-crack Region (Striations)

D2.3 2-months Test Duration, Low K_I

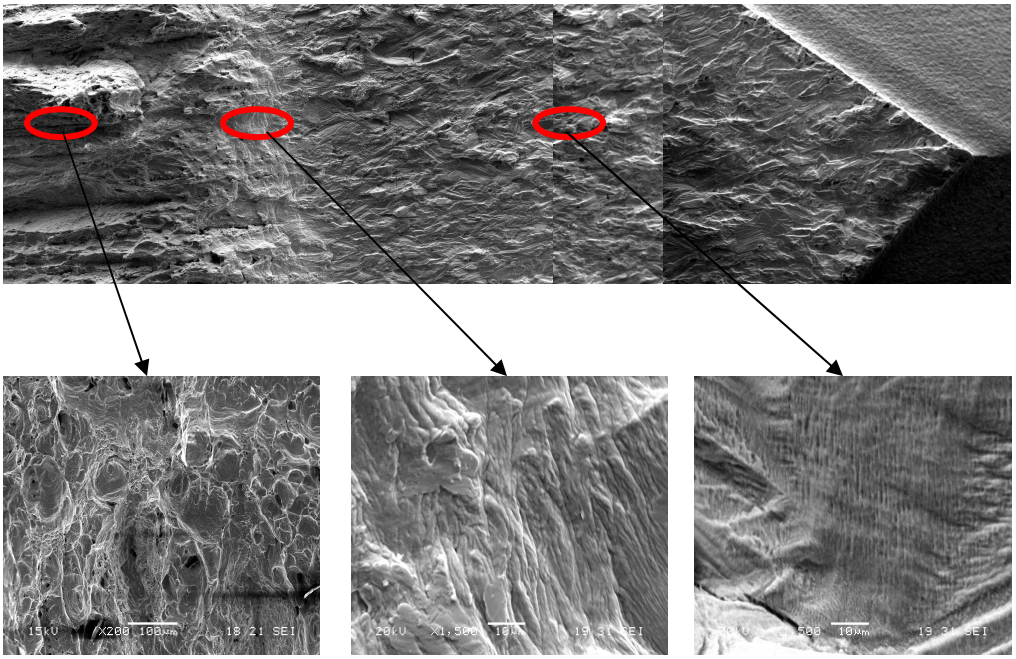

Fast Fracture Region (Dimples)

SCC Region (Cleavages)

Fatigue Pre-crack Region (Striations)

D2.4 2-months Test Duration, High K_I

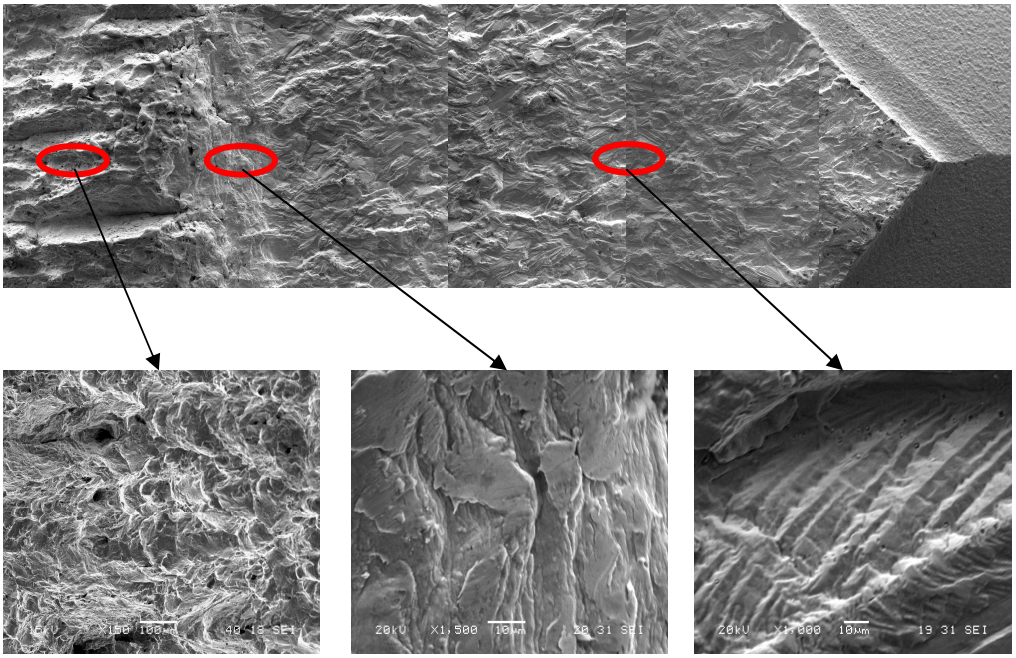

Fast Fracture Region (Dimples)

SCC Region (Cleavages)

Fatigue Pre-crack Region (Striations)

D2.5 4-months Test Duration, Low K_I

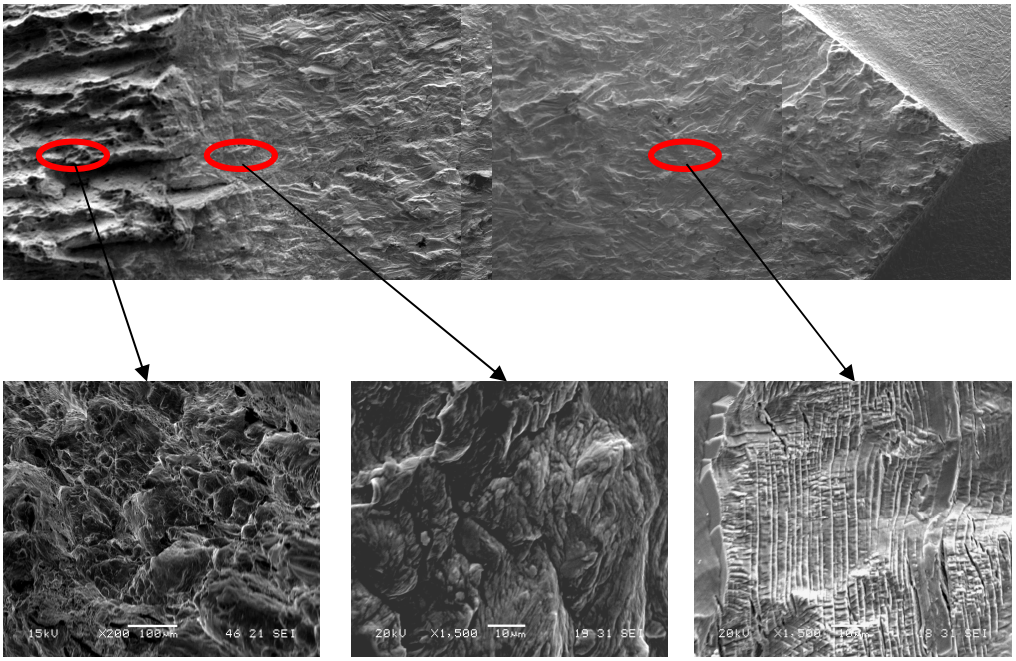

Fast Fracture Region (Dimples)

SCC Region (Cleavages)

Fatigue Pre-crack Region (Striations)

D2.6 8-months Test Duration, Low K_I

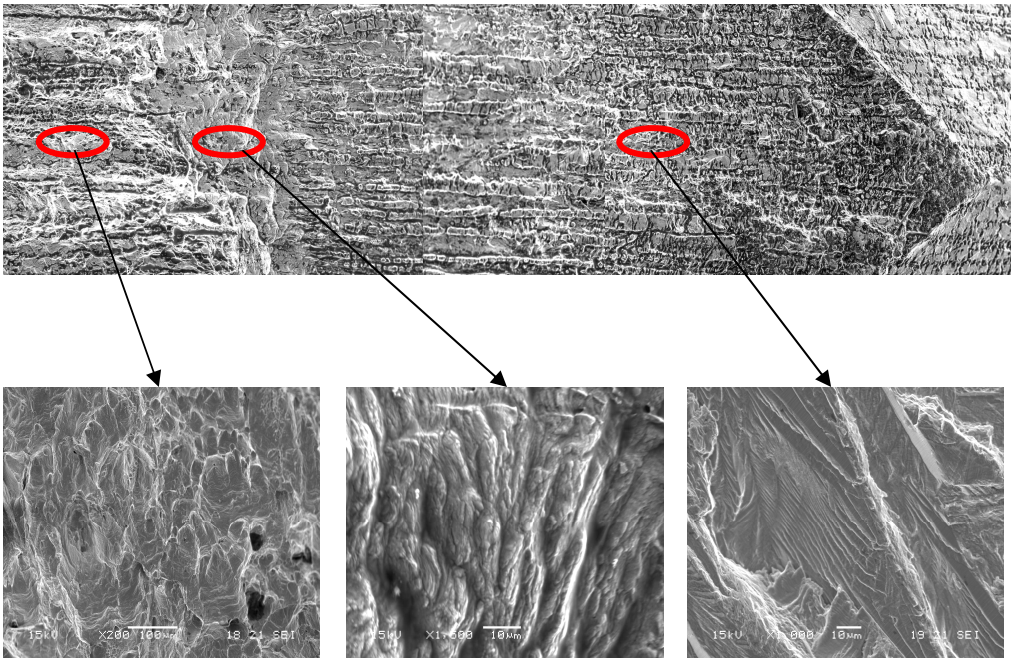

Fast Fracture Region (Dimples)

SCC Region (Cleavages)

Fatigue Pre-crack Region (Striations)

D2.7 8-months Test Duration, High K_I

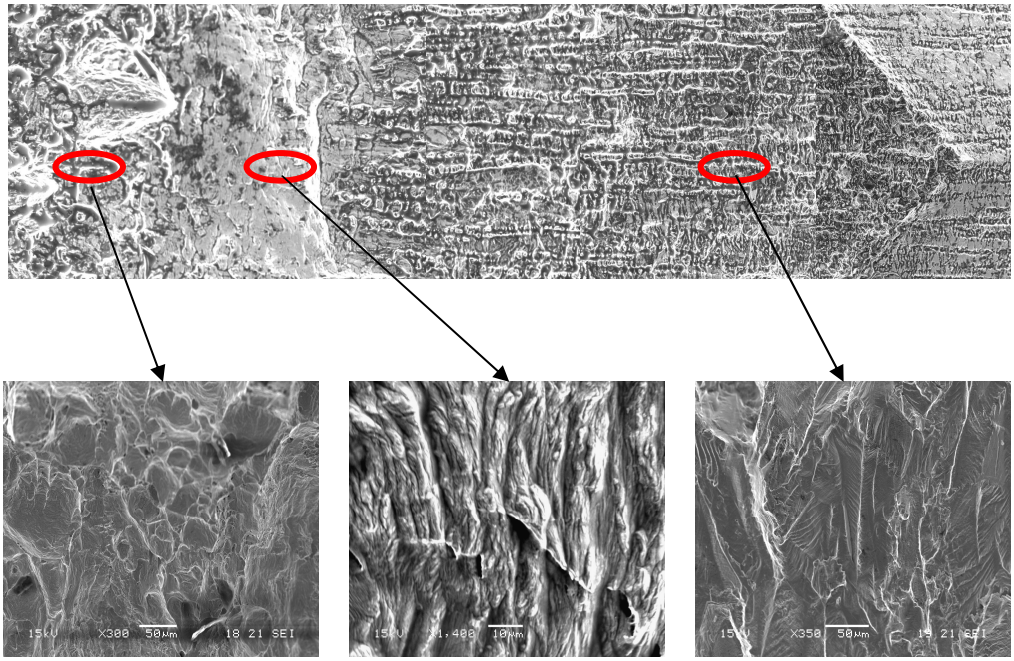

Fast Fracture Region (Dimples)

SCC Region (Cleavages)

Fatigue Pre-crack Region (Striations)

APPENDIX E

TRANSMISSION ELECTRON MICROGRAPHS

E1 Bright Field Images Showing Dislocations and Precipitates

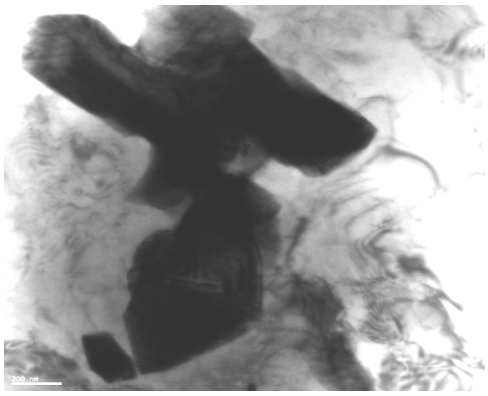

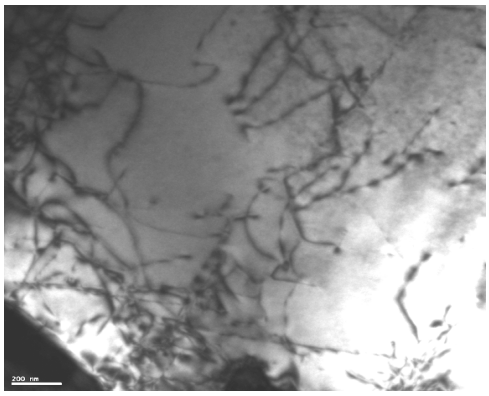

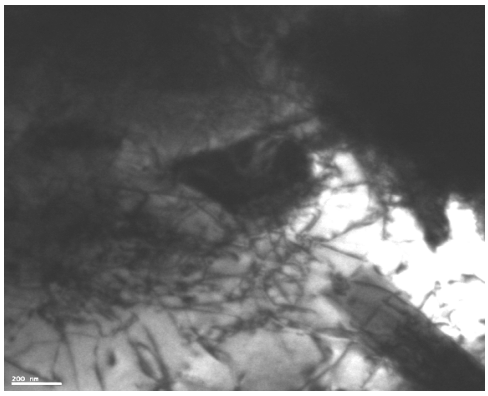

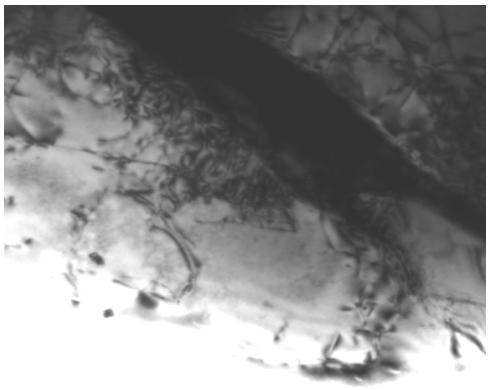

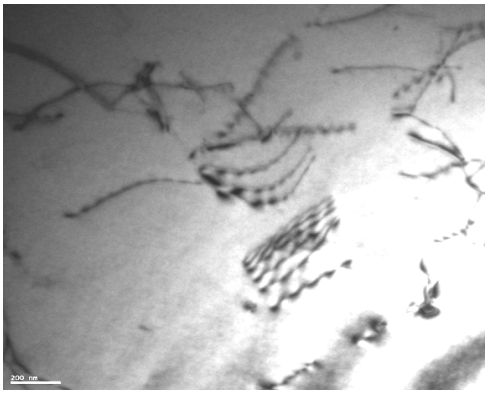

E2 STEM Mode Image Revealing Various Precipitates

APPENDIX F

UNCERTAINTY ANALYSES OF EXPERIMENTAL RESULTS

A precise method of estimating uncertainty in experimental results of CGR testing has been presented by Georgsson [72]. This method is applicable to tests conducted in load control mode at constant-amplitude (using the DCPD technique) and performed under uniaxial loading at ambient temperature.

The combined uncertainty in the results of this investigation was calculated by using the root sum squares equation, given below [72]. This uncertainty corresponds to plus or minus one standard deviation on the normal distribution law representing the studied quantity. This combined uncertainty has an associated confidence level of 68.27%.

$$U_c(y) = \sqrt{\sum_{i=1}^{N} \left[c_i u(x_i) \right]^2} \qquad \text{Equation F-1}$$

where

$U_c(y)$ = Combined uncertainty in the results

c_i = Sensitivity coefficient associated with x_i, usually = 1

The expanded uncertainty (U) was obtained by multiplying the combined uncertainty (U_c) by a coverage factor (k), the value of which was taken as 2 that corresponds to a confidence interval of 95.4% [72, 73]. It is to be noted that all uncertainty calculations in this section are based on a crack length of 0.9 mm for a CT specimen tested at ambient temperature and a load ratio of 0.1. However, this analysis can be applied to all other crack lengths.

F1 Uncertainty in Crack Length [U(a)]

Sample Calculation:

Standard deviation in crack length error due to PD-variation = S_{ea} = ±3.57 μm (S_{ea} value was determined from the 'ea' versus 'a' plot, as illustrated in Figure F-1).

Error in crack length = ea = $\left(a_{N+\Delta N} - a_N\right) - \left[\left(\frac{da}{dN}\right) \times \Delta N\right]$

Uncertainty in crack length due to PD variation =

$$u(a)_{PD} = \left(\frac{\delta a}{a}\right)_{PD} = S_{ea} \times d_v = \pm 3.57 \times 1 = \pm 3.57\ \mu m$$

Combined uncertainty in crack length =

$$U_c(a) = \sqrt{\sum_{i=1}^{N}\left[c_i u(x_i)\right]^2} = \sqrt{\left[c_{PD} u(a)_{PD}\right]^2} = \sqrt{\left[1 \times 3.57\right]^2} = \pm 3.57\ \mu m$$

Expanded uncertainty in crack length =

$U(a) = U_c(a) \times k$

$= \pm 3.57 \times 2$

$= \pm 7.14\ \mu m$

$= \pm \underline{0.00714\ mm}$

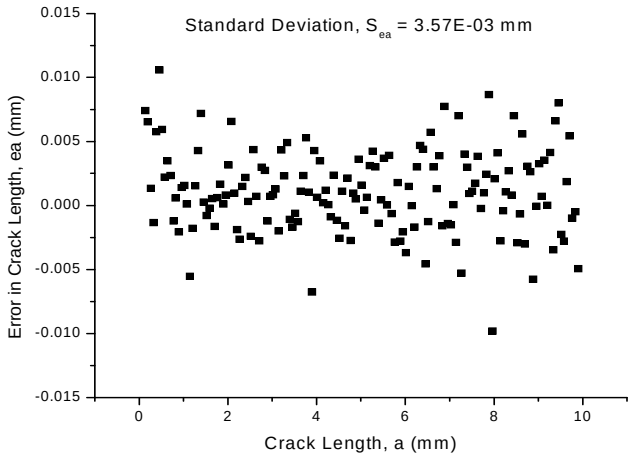

Figure F-1 ea vs. a

F2 Uncertainty in Stress-intensity-factor-range [U(ΔK)]

Sample Calculation:

Following analysis is based on ΔK = 21.04 MPa√m, corresponding to crack length of 0.9 mm.

F2.1 Uncertainty due to Alignment [$u(\Delta K)_a$]

Uncertainty in Instron alignment = ea = ±5% = ±0.05

$$u(\Delta K)_a = \left(\frac{\delta \Delta K}{K}\right)_a = \Delta K \times ea \times d_v = 21.04 \times \pm 0.05 \times 0.5 = \pm 0.526 \text{ MPa}\sqrt{m}$$

F2.2 Uncertainty due to Load Cell [$u(\Delta K)_l$]

Uncertainty in Instron load cell = ea = ±0.25% = ±0.0025

$$u(\Delta K)_l = \left(\frac{\delta \Delta K}{K}\right)_l = \Delta K \times ea \times d_v = 21.04 \times \pm 0.0025 \times 0.5 = \pm 0.0263 \text{ MPa}\sqrt{m}$$

Combined uncertainty in ΔK =

$$U_c(\Delta K) = \sqrt{\sum_{i=1}^{N}\left[c_i u(x_i)\right]^2} = \sqrt{\left[c_a u(\Delta K)_a\right]^2 + \left[c_l u(\Delta K)_l\right]^2}$$

$$= \sqrt{\left[1 \times 0.526\right]^2 + \left[1 \times 0.0263\right]^2} = \pm 0.527 \text{ MPa}\sqrt{m}$$

Expanded uncertainty in ΔK =

$U(\Delta K) = U_c(\Delta K) \times k$

$= \pm 0.527 \times 2$

$= \pm$<u>1.054 MPa√m</u>

F3 Uncertainty in da/dN [U(da/dN)]

Sample Calculation:

$$\frac{da}{dN} = \frac{\Delta a}{\Delta N} = \frac{\Delta a}{N_{average,(a=0.9mm)} - N_{average,(a=0.83mm)}} = \frac{0.9 - 0.83}{100472.8 - 97881} = 2.7 \times 10^{-5} \text{ mm/cycle}$$

$$\left(\frac{da}{dN}\right)_{S_N} = \frac{\Delta a}{\Delta N - S_N} = \frac{0.9 - 0.83}{(100472.8 - 97881) - 10145.445} = -9.3 \times 10^{-6} \text{ mm/cycle}$$

Error in da/dN =

$$u\left(\frac{da}{dN}\right) = \delta\left(\frac{da}{dN}\right) = \left[\left(\frac{da}{dN}\right)_{S_N} - \left(\frac{da}{dN}\right)\right] \times d_v$$

$$= \left[\left(-9.3 \times 10^{-6}\right) - \left(2.7 \times 10^{-5}\right)\right] \times 0.5$$

$$= \pm 1.815 \times 10^{-5} \text{ mm / cycle}$$

Combined uncertainty in da/dN =

$$U_c\left(\frac{da}{dN}\right) = \sqrt{\sum_{i=1}^{N}\left[c_i u(x_i)\right]^2} = \sqrt{\left[c \times u\left(\frac{da}{dN}\right)_a\right]^2}$$

$$= \sqrt{\left[1 \times (1.815 \times 10^{-5})\right]^2}$$

$$= \pm 1.815 \times 10^{-5} \text{ mm/cycle}$$

Expanded uncertainty in da/dN =

$U(da/dN) = U_c(da/dN) \times k$

$= \pm(1.815 \times 10^{-5}) \times 2$

$= \pm \underline{3.63 \times 10^{-5} \text{ mm/cycle}}$

BIBLIOGRAPHY

1. http://hydrogendoedev.nrel.gov/pdfs/review09/pd_12_pickard.pdf, B. Russ and P. Pickard, "Sulfur-Iodine Thermochemical Cycle," *2009 DOE Hydrogen Program Review*, May 19, 2009, Working Link, November 11, 2009.
2. "http://www.haynesintl.com/pdf/h2002.pdf," Corrosion Resistant Alloys – Hastelloy C-276 Alloy, Product Brochure, *Haynes International Inc.*, Working Link, September 30, 2009.
3. "http://www.corrosionmaterials.com/documents/dataSheet/alloyC276DataSheet.pdf," Alloy 276 Data Sheet, *Corrosion Materials*, Working Link, September 30, 2009.
4. S. A. McCoy, L. E. Shoemaker and J. R. Crum, "Corrosion Performance and Fabricability of the New Generation of Highly Corrosion-Resistant Nickel-Chromium-Molybdenum Alloys," Technical Paper – Aqueous Corrosion Alloys, *Special Metals Corporation*, Huntington, WV.
5. N. V. Kothapalli, "Characterization of Alloy C-276 as a Structural Material for High-Temperature Heat Exchangers," M.S. Thesis, Department of Mechanical Engineering, *University of Nevada, Las Vegas*, Summer 2005.
6. J. Pal, "Tensile Properties, Fracture Toughness and Crack Growth Study of Alloy C-276," M.S. Thesis, Department of Mechanical Engineering, *University of Nevada, Las Vegas*, Fall 2006.
7. A. K. Roy, J. Pal and C. K. Mukhopadhyay, "Dynamic Strain Ageing of an Austenitic Superalloy – Temperature and Strain Rate Effects," *Materials Science and Engineering A*, Vol. 474(1-2), 2008, pp. 363-370.

8. R. W. Hertzberg, "Deformation and Fracture Mechanics of Engineering Materials," 4th Edition, Publisher: *John Wiley & Sons, Inc*, NJ, 1996.
9. I. S. Tuba, "Comments on the Classical Elastic-Plastic Analysis for Fracture Mechanics Studies," *International Journal of Fracture Mechanics*, Vol. 6(1), 1970, pp. 61-64.
10. P. Agarwal and A. H. Shabaik, "High Temperature Deformation of Hastelloy Alloy C-276," *Proceedings of the Third International Symposium*, 1976, pp. 237-244.
11. "http://corrosion-doctors.org/MatSelect/corrstainsteel.htm", Stainless Steel Corrosion, *Corrosion Doctors*, Working Link, September 30, 2009.
12. "http://www.specialmetals.com/documents/Inconel%20alloy%20C-276.pdf," Technical Bulletin – Inconel Alloy C-276, Alloy Portfolio, *Special Metals Corporation*, Working Link, September 30, 2009.
13. Inconel Alloy C-276, "Heat No. Z7437CG – Product Certification," *Special Metals Corporation*, Huntington, WV.
14. Hastelloy C-276 Alloy, "Heat No. 276063671 – Product Certification," *Haynes International Inc.*, Kokomo, IN.
15. ASTM Designation E 647-00, "Standard Test Method for Measurement of Fatigue Crack Growth Rates," *American Society for Testing and Materials (ASTM) International*, West Conshohocken, PA, 2004.
16. ASTM Designation E 813-89, "Standard Test Method for J_{IC}, A Measure of Fracture Toughness," *American Society for Testing and Materials (ASTM) International*, West Conshohocken, PA, 1989.

17. NACE Standard TM0177-90, "NACE Standard Double-Cantilever-Beam Test, Method D," *NACE International*, Houston, TX, 1990, pp. 17–22.
18. ASTM Designation E 139-00, "Standard Test Methods for Conducting Creep, Creep-Rupture, and Stress-Rupture Tests of Metallic Materials," *American Society for Testing and Materials (ASTM) International*, West Conshohocken, PA, 2004.
19. "http://www.instron.us/wa/products/fatigue_testing/electric_actuator.aspx," Specifications of Model 8862, Dynamic and Fatigue Test Systems – High Precision Electric Actuator Systems, *Instron Corporation*, Working Link, September 30, 2009.
20. A. K. Roy, J. Pal and M. H. Hasan, "Temperature and Load Ratio Effects on Crack-Growth Behavior of Austenitic Superalloys," *Journal of Engineering Materials and Technology*, Vol. 132(1), 2010.
21. Q. Peng, S. Teysseyre and G. S. Was, "Stress Corrosion Crack Growth in 316 Stainless Steel in Supercritical Water," *3rd International Symposium on Supercritical Water-Cooled Reactors-Design and Technology*, Shanghai, China, 2007.
22. G. A. Hartman and D. A. Johnson, "D-C Electric-Potential Method Applied to Thermal/Mechanical Fatigue Crack Growth," *Experimental Mechanics*, Vol. 27(1), 1987, pp. 106-112.
23. N. Merah, "Detecting and Measuring Flaws using Electric Potential Techniques," *Journal of Quality in Maintenance Engineering*, Vol. 9(2), 2003, pp. 160-175.
24. *Fracture Technology Associates*, "Automated Fatigue Crack Growth Testing and Analysis Software," Version 3.09, Series 2001, Bethlehem, PA, 2001.
25. H. H. Johnson, "Calibration of Electric Potential Method for Studying Slow Crack Growth," *Materials Research Standards*, Vol. 5(9), 1965, pp. 442-445.

26. P. C. McKeighan and D. J. Smith, “Determining the Potential Drop Calibration of a Fatigue Crack Growth Specimen subject to Limited Experimental Observations,” *Journal of Testing and Evaluation*, Vol. 22(4), 1994, pp. 291-301.
27. Y. L. Lu et al., “Effects of Temperature and Hold Time on Creep-Fatigue Crack-Growth Behavior of Haynes 230 Alloy,” *Materials Science and Engineering A*, 429, 2006, pp. 1-10.
28. P. K. Liaw, A. Saxena and J. Schaefer, “Creep Crack Growth Behavior of Steam Pipe Steels: Effects of Inclusion Content and Primary Creep,” *Engineering Fracture Mechanics*, Vol. 57(1), 1997, pp. 105-130.
29. P. C. Paris and F. Erdogan, “A Critical Analysis of Crack Propagation Laws,” *Journal of Basic Engineering (Trans. ASME)*, Vol. 85(4), 1963, pp. 528-534.
30. J. A. Newman, “The Effects of Load Ratio on Threshold Fatigue Crack Growth of Aluminum Alloys,” Ph.D. Dissertation, Department of Engineering Mechanics, *Virginia Polytechnic Institute and State University*, Fall 2000.
31. J. Mallory, “Fatigue Crack Growth in 2324 Aluminum Alloy,” *Journal of Young Investigators*, Vol. 15(5), 2006.
32. V. Marthandam, “Tensile Deformation, Toughness and Crack Propagation Studies of Alloy 617,” Ph.D. Dissertation, Department of Mechanical Engineering, *University of Nevada, Las Vegas*, Spring 2008.
33. K. B. Yoon, T. G. Park and A. Saxena, “Elevated Temperature Fatigue Crack Growth Model for DS-GTD-111,” *Strength, Fracture and Complexity*, Vol. 4(1), 2006, pp. 35-40.

34. T. Yokobori and T. Aizawa, “The Influence of Temperature and Stress Intensity Factor upon the Striation Spacing and Fatigue Crack Propagation Rate of Aluminum Alloy,” *International Journal of Fracture*, Vol. 9(4), 1973, pp. 489-491.
35. T. Yokobori, A. T. Yokobori, Jr. and A. Kamei, “Dislocation Dynamics Theory for Fatigue Crack Growth,” *International Journal of Fracture*, Vol. 11(5), 1975, pp. 781-788.
36. T. Yokobori, S. Konosu and A. T. Yokobori, Jr., “Micro and Macro Fracture Mechanics Approach to Brittle Failure and Fatigue Crack Growth,” *Fracture 1977*, Vol. I(ICF4), Waterloo, Canada, 1977, pp. 665-682.
37. *Instron Corporation*, “Fast Track 2 – J_{IC} Unloading Compliance Software,”
38. “Nonlinear Fracture Toughness Testing,” *Structural Integrity Associates Inc.*, Technical Paper, San Jose, CA.
39. B. K. Neale, “The Fracture Toughness Testing of Centre-Cracked Tensile Specimens using the Unloading Compliance Technique,” *Engineering Fracture Mechanics*, Vol. 59(4), 1998, pp. 487-499.
40. J. E. P. Ipiñaa et al., “Fracture Toughness in Metal Matrix Composites,” *Materials Research*, Vol. 3(3), 2000, pp. 74-78.
41. “http://www.efunda.com/formulae/solid_mechanics/fracture_mechanics/fm_epfm_CTOD.cfm,” *efunda engineering fundamentals*, Working Link, September 30, 2009.
42. P. C. Paris et al., “The Theory of Instability of the Tearing Mode of Elastic-Plastic Crack Growth,” *Elastic-Plastic Fracture (ASTM STP)*, Vol. 668, 1979, pp. 5-36.

43. A. Martinelli and S. Venzi, "Tearing Modulus, J-Integral, CTOA and Crack Profile Shape obtained from the Load-Displacement Curve only," *Engineering Fracture Mechanics*, Vol. 53(2), 1996, pp. 263-277.

44. M. A. Shabara and M. D. Al-Ansary, "Tearing Modulus Analysis for Cracked Plates under Biaxial Loading," *International Journal of Pressure Vessels and Piping*, Vol. 64(2), 1995, pp. 111-117.

45. A. K. Roy et al., "Stress Corrosion Cracking of Alloy C-22 and Ti Gr-12 using Double-Cantilever-Beam Technique," *Micron*, Vol. 30(6), 1999, pp. 649-654.

46. A. K. Roy, D. C. Freeman and M. K. Spragge, "Stress Corrosion Cracking Evaluation of Candidate Container Alloys by Double Cantilever Beam Method," *Corrosion 2000*, Orlando, Florida, 2000, Paper No. 00189.

47. ASTM Designation E 399-99, "Standard Test Method for Linear-Elastic Plane-Strain Fracture Toughness K_{IC} of Metallic Materials," *American Society for Testing and Materials (ASTM) International*, West Conshohocken, PA, 2004.

48. G. E. Dieter, "Mechanical Metallurgy," 3rd Edition, Publisher: *McGraw-Hill*, NY, 1986.

49. "http://www.doitpoms.ac.uk/tlplib/creep/intro.php," Creep Deformation of Metals – Introduction, DoITPoMS Teaching and Learning Packages, *University of Cambridge*, Working Link, September 30, 2009.

50. "http://www.metallurgy.nist.gov/solder/clech/Report_Images/Figure_1.png," Materials Science and Engineering Laboratory, *The National Institute of Standards and Technology (NIST)*, Working Link, September 30, 2009.

51. P. S. Shankar and K. Natesan, “Effect of Trace Impurities in Helium on the Creep Behavior of Alloy 617 for Very High Temperature Reactor Applications,” *Journal of Nuclear Materials*, Vol. 366(1-2), 2007, pp. 28-36.
52. G. F. V. Voort and E. P. Manilova, “Metallographic Techniques for Superalloys,” *Microsc Microanal, Microscopic Society of America*, Vol. 10(2), 2004.
53. ASTM Designation E 112-96, “Standard Test Methods for Determining Average Grain Size,” *American Society for Testing and Materials (ASTM) International*, West Conshohocken, PA, 2004.
54. L. Ma, “Comparison of Different Sample Preparation Techniques in TEM Observation of Microstructure of Inconel Alloy 783 Subjected to Prolonged Isothermal Exposure,” *Micron*, Vol. 35(4), 2004, pp. 273-279.
55. P. E. Fischione, “Materials Specimen Preparation for Transmission Electron Microscopy,” *E. A. Fischione Instruments, Inc. Export*, PA, USA.
56. ASM Handbook, “Metallography and Microstructures,” Publisher: *ASM International*, Vol. 9, Materials Park, OH, 2004.
57. K. Yabusaki and H. Sasaki, “Specimen Preparation Technique for a Microstructure Analysis using the Focused Ion Beam Process,” *Furukawa Review*, No. 22, 2002.
58. M. Meier, “Measuring Grain Size,” Department of Chemical Engineering and Materials Science, *University of California, Davis*, 2004.
59. J. J. Friel, “Practical Guide to Image Analysis,” Publisher: *ASM International*, Materials Park, OH, 2000.

60. ASTM Designation E 8-04, “Standard Test Methods for Tensile Testing of Metallic Materials,” *American Society for Testing and Materials (ASTM) International*, West Conshohocken, PA, 2004.

61. Z. Zheng et al., “The Characterization of Fatigue Crack Growth Behavior by Constant ΔK Control Testing,” *Fatigue & Fracture of Engineering Materials & Structures*, Vol. 22(5), 1999, pp. 383-392.

62. H. Tsuji, H. Nakajima and T. Kondo, “Effect of ΔK Control Modes on Variability/Reproducibility of Fatigue Crack Growth Rate Data,” *Journal of Nuclear Materials*, Vol. 189(1), 1992, pp. 65-71.

63. “http://www.twi.co.uk/content/jk76.html,” CTOD Testing, *TWI (World Centre for Materials Joining Technology)*, Working Link, September 30, 2009.

64. A. K. Roy, M. H. Hasan and J. Pal, “Creep Deformation of Alloys 617 and 276 at 750-950 °C,” *Materials Science and Engineering A*, Vol. 520(1-2), 2009, pp. 184-188.

65. A. R. Ibañez, A. Saxena and J. D. Kang, “Creep Behavior of a Directionally Solidified Nickel Based Superalloy,” *Strength, Fracture and Complexity*, Vol. 4(2), 2006, pp. 75-81.

66. T. Yokobori and A. T. Yokobori, Jr., “High Temperature Creep, Fatigue and Creep–Fatigue Interaction in Engineering Materials,” *International Journal of Pressure Vessels and Piping*, Vol. 78(11-12), 2001, pp. 903-908.

67. V. I. Kovpak and A. N. Olisov, “Some Characteristics of the High-Temperature Creep of Nickel-Base Alloys,” *Strength of Materials*, Vol. 5(2), 1973, pp. 183-187.

68. J. R. Davis, "Corrosion of Weldments," 1st Edition, Publisher: *ASM International*, Materials Park, OH, 2006.

69. F. G. Hodge, "Effect of Aging on the Anodic Behavior of Ni-Cr-Mo Alloys," *Corrosion*, Vol. 29(10), 1973, pp. 375-383.

70. M. Raghavan, B. J. Berkowitz and J. C. Scanlon, "Electron Microscopic Analysis of Heterogeneous Precipitates of Hastelloy C-276," *Metallurgical and Materials Transactions A*, Vol. 13(6), 1982, pp. 979-984.

71. S. Kihara et al., "Morphological Changes of Carbides during Creep and Their Effects on the Creep Properties of Inconel 617 at 1000 °C," *Metallurgical and Materials Transactions A*, Vol. 11(6), 1980, pp. 1019-1031.

72. P. Georgsson, "The Determination of Uncertainties in Fatigue Crack Growth Measurement," *Manual of Codes of Practice for the Determination of Uncertainties in Mechanical Tests on Metallic Materials*, *Standards Measurement & Testing Programme*, Issue 1, 2000.

73. BIPM, IEC, IFCC, ISO, IUPAC, OIML, "Guide to the Expression of Uncertainty in Measurement," *International Organization for Standardization*, Geneva, Switzerland, 1st Edition, 1993.

VITA

Graduate College
University of Nevada, Las Vegas

Joydeep Pal

Degrees:

Bachelor of Science in Mechanical Engineering, 2000
Jadavpur University
Kolkata, India.

Master of Science in Mechanical Engineering, 2006
University of Nevada, Las Vegas
Las Vegas, Nevada.

Special Honors and Awards:

- 'GREAT' Scholarship, Summer 2008.
- Phi Kappa Phi, Fall 2007.
- Tau Beta Pi, Fall 2006.

Publications:

Journal Articles:

- A. K. Roy, J. Pal and M. H. Hasan, "Temperature and load ratio effects on crack-growth behavior of austenitic superalloys," Journal of Engineering Materials and Technology, Vol. 132(1), January 2010.
- A. K. Roy, M. H. Hasan and J. Pal, "Creep deformation of alloys 617 and 276 at 750-950 °C," Materials Science and Engineering A, Vol. 520(1-2), 2009, pp. 184-188.
- A. K. Roy, R. S. Koripelli and J. Pal, "Tensile deformation of a nickel-base superalloy for application in hydrogen generation," International Journal of Hydrogen Energy, Vol. 33(3), 2008, pp. 945-952.
- A. K. Roy, J. Pal and C. K. Mukhopadhyay, "Dynamic strain ageing of an austenitic superalloy – temperature and strain rate effects," Materials Science and Engineering A, Vol. 474(1-2), 2008, pp. 363-370.

Selected Conference Presentations:

- J. Pal, M. H. Hasan and A. K. Roy, "Crack growth behavior of alloy 276 as functions of temperature and load ratio," TMS 2009, San Francisco, CA, February 2009.
- J. Pal and A. K. Roy, "Cracking of alloy C-276 in an acidic environment," ASME-PVP, PVP 2007-26429, San Antonio, TX, July 2007.
- J. Pal and A. K. Roy, "Tensile properties and stress corrosion crack growth studies of alloy C-276", AMPT 2006, Las Vegas, NV, July–August 2006.

- J. Pal et al., “High-temperature tensile properties of nickel-base alloys for hydrogen generation”, SAMPE, Long Beach, CA, April–May, 2006.
- J. Pal and A. K. Roy, “Tensile properties and corrosion susceptibility of alloy C–276 in S–I environment”, AICHE, Cincinnati, OH, October–November, 2005.

Dissertation Title: “Fracture Toughness, Crack-Growth-Rate and Creep Studies of Alloy 276”

Dissertation Examination Committee:

Chairperson, Brendan O’Toole, Ph.D.
Co-chairperson, Ajit K. Roy, Ph.D.
Committee Member, Anthony E. Hechanova, Ph.D.
Committee Member, Woosoon Yim, Ph.D.
Committee Member, Daniel Cook, Ph. D.
Graduate Faculty Representative, Edward S. Neumann, Ph.D.